Least-squares mixed finite elements for geometrically nonlinear solid mechanics

Von der Fakultät für Ingenieurwissenschaften,
Abteilung Bauwissenschaften
der Universität Duisburg-Essen
zur Erlangung des akademischen Grades

Doktor-Ingenieur

genehmigte Dissertation

von

Karl Steeger, M.Sc.

Hauptreferent:	Prof. Dr.-Ing. habil. J. Schröder
Korreferenten:	Prof. Dr. rer. nat. G. Starke
	Prof. Dr.-Ing. habil. A. Düster

Tag der Einreichung:	25. November 2016
Tag der mündlichen Prüfung:	12. Mai 2017

Fakultät für Ingenieurwissenschaften,
Abteilung Bauwissenschaften
der Universität Duisburg-Essen
Institut für Mechanik
Prof. Dr.-Ing. habil. J. Schröder

Herausgeber:

Prof. Dr.-Ing. habil. J. Schröder

Organisation und Verwaltung:

Prof. Dr.-Ing. habil. J. Schröder
Institut für Mechanik
Fakultät für Ingenieurwissenschaften
Abteilung Bauwissenschaften
Universität Duisburg-Essen
Universitätsstraße 15
45141 Essen
Tel.: 0201 / 183 - 2682
Fax.: 0201 / 183 - 2680

ISBN-10 3-9818074-1-3
ISBN-13 978-3-9818074-1-7
EAN 9783981807417

Für Kristina und Gabriel

Vorwort

Die vorliegende Arbeit entstand während meiner Tätigkeit als wissenschaftlicher Mitarbeiter am Institut für Mechanik (Abteilung Bauwissenschaften, Fakultät für Ingenieurwissenschaften) an der Universität Duisburg-Essen unter anderem im Rahmen des durch die Deutsche Forschungsgemeinschaft (DFG) finanzierten Projektes SCHR 570/14-1, STA 402/11-1. An dieser Stelle möchte ich der DFG für die finanzielle Unterstützung danken und meinen persönlichen Dank an einige Menschen aussprechen, die ihren jeweiligen Anteil zum Gelingen dieser Arbeit beigetragen haben.
Zuallererst möchte ich meinem geschätzten Doktorvater Professor Jörg Schröder aufrichtig danken, der mir die Möglichkeit gab unter seiner Leitung zu promovieren. Ihm gilt der Dank für die Förderung während der gesamten Promotionszeit. Seine besondere Art und Weise der Motivation während der gesamten Zeit und sein Enthusiasmus für die Mechanik waren für mich stets eine Quelle der Inspiration. Besonders danken möchte ich auch Professor Gerhard Starke, sowohl für die Übernahme des Zweitgutachtens als auch für die erfolgreiche Zusammenarbeit im Rahmen des gemeinsamen DFG Projektes und darüber hinaus. Bei vielen Diskussionen habe ich sein weitreichendes Wissen in der Mathematik zu schätzen gelernt. Weiterhin gilt mein Dank auch Professor Alexander Düster für sein Interesse an der Arbeit und die Übernahme des externen Gutachtens. Ich danke Professor Joachim Bluhm, der sich jederzeit gerne für fachliche Angelegenheiten Zeit nahm. Sein Wissen und seine Erfahrung führten stets zu guten Ratschlägen. Ein herzliches Dankeschön auch an meine Wegbegleiter Bernhard Eidel, Marc-Andre Keip und Oliver Rheinbach, deren Kompetenzen und ihre Bereitschaft diese zu teilen mir stets eine große Hilfe waren. Dominik Brands gilt mein Dank für jede Art von Unterstützung hinsichtlich der Administration, eingeschlossen der Pflege meines Rechners. Ebenfalls möchte ich Benjamin Müller und Fleurianne Bertrand für die Zusammenarbeit und den mathematischen Austausch danken.
Ein besonderer Dank gilt meinen studentischen Hilfskräften Robert Depenbrock, Maximilian Igelbüscher, Sascha Maassen, Dominik Ohlmann, Yasemin Özmen und Nils Viebahn für die intensive (und teilweise noch andauernde) Zusammenarbeit. Sie schenkten mir ihr Vertrauen, gaben mir die Möglichkeit sie zu fördern und ihre Abschlussarbeiten zu betreuen. Es erfüllt mich mit Stolz zu sehen, wozu sie es bereits heute schon gebracht haben. Darüber hinaus möchte ich Alexander Schwarz danken, der mich bereits während meines Bachelorstudium gefördert hat. Ich durfte an die wissenschaftlichen Erkenntnisse seiner Promotion anknüpfen und er war jederzeit bereit, sein breites Wissen mit mir zu teilen. Die vielen Diskussionen über finite Elemente führten oft zu wesentlichen Erkenntnisgewinnen.
Aufs Herzlichste möchte ich meinen derzeitigen und ehemaligen Kolleginnen und Kollegen am Institut danken, zu denen Solveigh Averweg, Daniel Balzani, Julia Bergmann, Moritz Bloßfeld, Sarah Brinkhues, Vera Ebbing, Simon Fausten, Markus von Hoegen, Veronika Jorisch, Marc-Andre Keip, Simon Kugai, Matthias Labusch, Veronica Lemke, Petra Lindner-Roullé, Simon Maike, Rainer Niekamp, Carina Nisters, Mangesh Pise, Sabine Ressel, Lisa Scheunemann, Thomas Schmidt, Serdar Serdas, Steffen Specht und Huy Ngoc Thai gehören.
Meinen Eltern, meinen Schwiegereltern und meiner gesamten Familie möchte ich danken für die immerwährende Unterstützung. Abschließend danke ich meiner Frau Kristina, die den langen Weg zur Promotion mit mir gegangen ist. Ihre Geduld, ihr Verständnis und ihre Fürsorge waren mir stets eine große Hilfe.

Essen, im Juni 2017 Karl Steeger

Abstract

The computation of reliable results using finite elements is a major engineering goal. Under the assumption of a linear elastic theory many stable and reliable (standard and mixed) finite elements have been developed. Unfortunately, in the geometrically non-linear regime, e.g. applying these elements in the field of incompressible, hyperelastic materials, problems can occur. A possible approach to circumvent these issues might be the least-squares mixed finite element method. Therefore, in this thesis, a mixed least-squares formulation for hyperelastic materials in the field of solid mechanics is provided, investigated and valuated. To create a theoretical basis the continuum mechanical background is outlined, the necessary physical quantities are introduced and the construction of suitable interpolation functions for the interpolation in $W^{1,p}(\mathcal{B})$ (using standard interpolation polynomials) and $W^q(\mathrm{div}, \mathcal{B})$ (using vector-valued Raviart-Thomas interpolation functions) are derived. Furthermore, the general procedure for the construction of a least-squares functional is described and applied for hyperelastic material laws based on a free energy function. Basis for the proposed least-squares element formulation is a div-grad first-order system consisting of the equilibrium condition, the constitutive equation and a stress symmetry condition, all written in a residual form. The solution variables (displacements and stresses) are, dependent on the element type, interpolated using different approximation spaces. The resulting elements are named as $P_m P_k$ and $RT_m P_k$. Here m (stresses) and k (displacements) denote the polynomial order of the particular interpolation function. The performance of the provided elements is investigated and compared to standard and mixed Galerkin elements by extensive numerical studies with respect to e.g. bending dominated problems, incompressibility, stability issues, convergence of the field quantities and adaptivity. Furthermore, the crucial influence of weighting is discussed. Finally, the results are evaluated and the used elements are assessed.

Zusammenfassung

Ein Hauptziel im Bereich des Ingenieurwesens ist die Berechnung vertrauenswürdiger Ergebnisse mit Hilfe der Methode der finiten Elemente. Unter Annahme einer linear elastischen Theorie wurden hierzu bereits viele stabile und zuverlässige standard und gemischte finite Elemente entwickelt. Es hat sich jedoch herausgestellt, dass bei einigen dieser Elemente, unter anderem angewandt auf inkompressible, hyperelastische Materialien, Probleme auftreten. Ein möglicher Ansatz um diese Probleme zu umgehen ist möglicherweise die gemischte least-squares finite Elemente Methode. Daher wird in Rahmen dieser Arbeit eine gemischte least-squares Formulierung für hyperelastische Materialien vorgestellt, untersucht und bewertet. Um eine theoretische Basis zu schaffen wird zuerst ein kontinuumsmechanischer Rahmen geschaffen, die nötigen physikalischen Größen werden eingeführt und die Konstruktion geeigneter Interpolationsfunktionen zur Interpolation in $W^{1,p}(\mathcal{B})$ (mit standard Interpolationspolynomen) und $W^q(\mathrm{div}, \mathcal{B})$ (mit vektorwertigen Raviart-Thomas Interpolationsfunktionen) werden hergeleitet. Im Folgenden wird das allgemeine Vorgehen zur Konstruktion eines least-squares Funktionals beschrieben und angewandt auf hyperelastische Materialien in der Festkörpermechanik basierend auf freien Energiefunktionen. Die Basis für die least-squares Formulierung stellt ein div-grad System erster Ordnung dar, bestehend aus der Gleichgewichtsbedingung, einem Materialgesetz und einer zusätzlichen Bedingung für die Einhaltung einer Spannungssymmetrie. Die Gleichungen liegen hierbei in einer residualen Form vor. Die

Lösungsvariablen sind, im Rahmen dieser Arbeit, die Verschiebungen und die Spannungen welche, abhängig vom Elementtyp, mit unterschiedlichen Interpolationsfunktionen interpoliert werden. Die resultierenden Elemente werden bezeichnet als $P_m P_k$ und $RT_m P_k$, wobei m und k die jeweilige Interpolationsordnung zur Approximation der Spannungen (m) und der Verschiebungen (k) angeben. Die Performanz der entwickelten Elemente wird im Folgenden mit extensiven numerischen Studien untersucht, welche sich unter anderem mit biegedominierten Problemen, Inkompressibilität, Untersuchung von Stabilitätspunkten und der allgemeinen Konvergenz der Lösungsvariablen beschäftigen. Zur Bewertung der Ergebnisse werden diese mit Lösungen verglichen, welche durch standard und gemischte Galerkin Elemente berechnet wurden. Darüber hinaus wird der starke Einfluss der Wichtungsfaktoren auf die Qualität der Lösungen diskutiert. Abschließend werden die Ergebnisse ausgewertet und die entwickelten Elemente bewertet.

Contents

1 Introduction

In this day and age the solution of physical problems on arbitrary domains using numerical simulation methods is widely spread and established in almost all engineering areas. This becomes possible due to the raising computer power which growth followed, at least up to the last years, Moore's law, see Moore [1965]. In the field of solid mechanics the finite element method (FEM) is therefore an almost indispensable integral part of modeling and simulation in engineering applications. The origin of the method can be found in the 1950's inter alia by Argyris and Kelsey [1954], Argyris [1955] and Turner et al. [1956]. The terminology "finite element" has then been introduced by Clough [1960]. In the following decades the method has been extendend and examined further. An overview over the publications with respect to the finite element method is provided, for instance, in Noor [1991] or more recently in the historical overview over various milestones of Stein [2012]. Furthermore, for a comprehensive collection of todays computational methods the reader is referred to the book series of Stein et al. [2004].

1.1 Galerkin and mixed Galerkin finite elements

The underlying variational principle for the solution of the given differential equations is mostly the so-called Galerkin method (Standard Galerkin method), which origin is given in Galerkin [1915]. This method is, in the field of solid mechanics, often restricted on the displacement as field quantitiy. Unfortunately, certain problems limit the applicability of the standard method. That means, that for example incompressible materials could lead to not well-posed formulations. In the case of incompressible or nearly incompressible materials volumetric locking can be observed, resulting in a lower convergence behavior or even a pathological approximation of the stresses, see e.g. Babuška and Suri [1992]. Furthermore, in the field of the standard displacement based FEM the stresses are generally computed as the derivatives of a $\mathcal{C}^0$ continuous function. This leads to a stress field which could be discontinuous at element interfaces. In addition to that, for bending-dominated problems, standard approaches could cause shear locking. In this context "standard" means the classical linear respectively quadratic Galerkin elements. Possible approaches to overcome this problems is to use high-order elements, compare e.g. Düster et al. [2003], Heisserer et al. [2008] and Netz et al. [2013] or to use mixed finite elements.

The basis for these mixed formulations are here mostly variational formulations of Hellinger-Reissner or Hu-Washizu type. To ensure the stability of the resulting saddlepoint structure, methods of this type have to fulfill the so-called LBB-condition (Ladyzhenskaya-Babuška-Brezzi-Bedingung), based on Ladyzhenskaya [1969], Babuška [1973] and Brezzi [1974]. An overview over the analysis can be found e.g. in Bathe [1995], Bathe [2001] and Ern and Guermond [2013]. This condition demands to balance the chosen interpolation orders for the different field quantities. The first hybrid stress finite element, based on the minimum of a complementary energy has been developed by Pian [1964]. Drawbacks of this approach concerning invariance requirements has been eliminated by Pian and Sumihara [1984]. The basis was a Hellinger-Reissner functional, where stresses and displacements were used as basic field variables. Using a non-symmetric approximation of the stress field, Klaas et al. [1995] developed a formulation based on an extended dual Hellinger-Reissner functional with two additional unknown fields leading to optimal convergence rates for the displacements and stresses which are approximated

by Brezzi-Douglas-Marini (BDM) elements, see Brezzi et al. [1985]. Further studies concerning elasto-plasticity problems can be found in Schröder et al. [1997]. On the basis of a Hu-Washizu functional a further approach, the so-called $\bar{\boldsymbol{F}}$-method, was developed by Simo et al. [1984]. This formulation makes use of the multiplicative split of the deformation gradient into volumetric and isochoric parts. In particular for lower order elements certain versions of this have been successfully applied, see de Souza Neto et al. [1996; 2005]. Beyond that, ideas dealt with non-locally averaged nodal stress and deformation quantities. For further approaches, where averages of the pressure or deformation quantities are taken into account over domains that are associated to nodes, edges and faces, see e.g. Dohrmann et al. [2000], Gee et al. [2009], and Liu and Nguyen-Thoi [2010]. A major drawback is that such elements can not be implemented with an acceptable effort in standard commercial finite element software, which is due to the nonlocal averaging operator. Furthermore, the method of incompatible modes, see Wilson et al. [1973] and Taylor et al. [1976], was the starting point for the class of mixed enhanced strain element formulations. Based on the three-field Hu-Washizu functional the Enhanced-Assumed-Strains (EAS) approach has been provided respectively investigated by Simo and Rifai [1990], Simo and Armero [1992] Simo et al. [1993], Reddy and Simo [1995], and Freischläger and Schweizerhof [1996]. Unfortunately, the enhanced elements may encounter mesh-instabilities, such as hourglassing, see Wriggers and Reese [1996]. In this context, reduced integration as well as stabilization techniques can be found in e.g., Bischoff et al. [1999], Reese et al. [1999] and Reese and Wriggers [2000]. A recent publication giving an extensive overview over mixed finite element methods is given by Boffi et al. [2013].

1.2 Least-squares mixed finite elements

A further finite element approach, which increasingly gains attention in the last decades, is the least-squares method. Initially, the least-squares method is the standard approach for regression analysis where it is used to compute, for an arbitrary number of datapoints, a curve which fulfills the given points in a least-squares sense.

The least-squares finite element method (LSFEM) is characterized by several advantages. The LSFEM replaces, for instance, a constrained minimization problem (with saddlepoint structure) by a least-squares formulation without constraints. Thus, it is not restricted by the latter mentioned LBB-condition and it is possible to combine (more or less arbitrary) polynomial orders for the interpolation of the unknowns without losing stability properties. Furthermore, the resulting system matrices are always positive definite which could be advantageous for the applied solver. In addition to that the least-squares functional can be set up using freely selectable field variables and governing equations. A further advantage of the method is that the functional is usable as an inherent a posteriori error indicator, compare e.g. Cai and Starke [2004] and Bochev and Gunzburger [2009]. That means, that for an adaptive mesh refinement strategy no additional costs has to be invested in the error estimation. Unfortunately, the method, as far it has been investigated until today, contains also several disadvantages. Here the weak performance of low order elements has to be mentioned, compare e.g. Pontaza [2003], Pontaza and Reddy [2003] and Schwarz et al. [2010]. Furthermore, the used (physical) residuals respectively their weighting have a crucial impact on the accuracy of the solution and have to be balanced suitably. First applications of the least-squares method in the field of finite elements respectively their mathematical analysis can be found e.g. in Lynn and Arya [1973; 1974],

Zienkiewicz et al. [1974], Jespersen [1977] and Fix et al. [1979]. An overview over the least-squares method and its first applications in the field of finite elements is given in Eason [1976]. Furthermore, in this publication inter alia the advantages of the method are already discussed. In the following decade the number of publications concernig this topics reduces (e.g. Aziz et al. [1985]). This is eventually due to weak approximation quality for lower order elements which where mainly used at that time. The beginning of the 1990's brought a boom for the method, which was mainly restricted on the field of fluid mechanics, compare e.g. Jiang and Chang [1990], Chang and Jiang [1990], Jiang [1992], Tang and Tsang [1993], Cai et al. [1994], Bochev and Gunzburger [1994; 1995], Cai et al. [1995], Chang et al. [1995], Bell and Surana [1994], Bochev [1994; 1999], Berndt et al. [1997], Bochev et al. [1998], Bochev et al. [1999], Ding and Tsang [2001; 2003], Pontaza and Reddy [2003], Kayser-Herold and Matthies [2003] and Kayser-Herold and Matthies [2007]. Here, the used first-order systems interpolate different combinations as, for instance, the flow velocity, the pressure, the stresses or the vorticity field. The approximation of these unknown quantities was mainly restricted on the Sobolev space $H^1(\mathcal{B})$. For an overview over the developments of the least-squares method in the field of fluid mechanics the reader is referred to Jiang [1998], Bochev and Gunzburger [2009] and Kayser-Herold and Matthies [2005] and the references therein.

In the field of solid mechanics the number of publications considering the least-squares method is significantly smaller. First formulations can be found e.g. in Cai et al. [1995], where a formulation for linear elastic problems has been provided. Therefore, the authors used as a basis a div-curl-grad system of first-order with the unknown fields velocity, vorticity and pressure (VVP). Further investigations of this working group, also in the field of linear elastic problems, are inter alia Cai et al. [1997; 1998; 2000a;b] and Kim et al. [2000]. In this publications the displacement and the displacement gradient are used as field quantities and are interpolated in $H^1(\mathcal{B})$. In the works of Cai and Starke [2004] and Cai et al. [2005] the authors used the displacement and the stresses as unknown fields. The approximation of the quantities has been executed in $H^1(\mathcal{B})$ via standard polynomial interpolation for the displacement field and, for the stress field, vector-valued interpolation functions of Raviart-Thomas type, see Raviart and Thomas [1977], in $H(\mathrm{div}, \mathcal{B})$. This choice of interpolation spaces has been continued for instance in Schwarz [2009] and Schwarz et al. [2010]. In the latter mentioned publications also the suitability of the functional as an error indicator, the fulfillment of the stress symmetry as well as the behavior of the formulations considering (nearly) incompressible materials is discussed. Furthermore, a main benefit of the formulation in Schwarz et al. [2010] is the good performance of the developed low order element. This is due to a modification of the first variation of the functional and the resulting improvement of the momentum balance. An extension on transversely isotropic elasticity can be found in Schwarz and Schröder [2007] and in Schwarz et al. [2014] a least-squares formulation with an additional (redundant) residual has been used. In Bertrand et al. [2014] the application of the first-order system least-squares method on curved boundaries is provided. In the field of material nonlinearities, in detail elasto-plasticity, Kwon et al. [2005] and Starke [2007] published results. A main issue in this context has been the non-smoothness of the constitutive relation in the case of plastic deformations and the resulting problems using standard nonlinear solver. To overcome this, Starke [2009] used a non-smooth Newton method which results in suitable convergence rates. In the work of Schwarz et al. [2009b] this issue is circumvented by a modified approach and in Schwarz et al. [2009a] the authors used a viscoplastic formu-

lation. In Steeger et al. [2015] the authors investigate a displacement-stress formulation where they consider the performance using an interpolation of the stresses in $H(\mathrm{div}, \mathcal{B})$ compared to an interpolation of the stresses in $H^1(\mathcal{B})$. In the publications of Jiang and Wu [2002] and Jiang [2002] two different formulations are taken under consideration. In Jiang and Wu [2002] (part 1), beside the displacement and the stresses, the rotation with respect to the plane normal is used as a basis for the formulation. The second part (Jiang [2002]) considers a formulation for the computation of bending problems considering thin plates. Therefore, the author used a first-order system which depends on four different quantities and shows optimal convergence rates in the provided examples.

First investigations in the field of geometrically nonlinear problems in the field of solid mechanics are e.g. Westphal [2004] and Manteuffel et al. [2006] where a constitutive relation of St.Venant-Kirchhoff type has been considered. As of late also least-squares formulations for hyperelastic problems has been developed, see e.g. Schwarz et al. [2012], Starke et al. [2012], Müller et al. [2014], Müller [2015] and Müller and Starke [2016]. In Schröder et al. [2016] several least-squares formulations for isotropic and anisotropic elasticity at small and large strains are given. In Kadapa et al. [2015] a formulation using the displacements and the pressure as field quantities, interpolated by NURBS (non-uniform rational B-splines), has been provided. Here, fluid mechanical problems as well as problems in the field of solid mechanics (hyperelasticity) are taken under consideration.

1.3 Outline

This work is organized as follows: After a brief introduction of the used physical quantities and the essential continuum mechanical relations several hyperelastic free-energy functions are given in **Section 2**. The used interpolation spaces $W^{1,p}(\mathcal{B})$ and $W^q(\mathrm{div}, \mathcal{B})$ are introduced and the derivation of suitable functions for the approximation in these spaces are shown for different interpolation orders in **Section 3**. Here, especially the construction of vector-valued Raviart-Thomas functions is discussed in detail. Furthermore, an alternative way for the development of such functions is described. **Section 4** provides the general rule for construction of a least-squares functional followed by the derivation of a least-squares mixed finite element formulation for hyperelastic free energy functions. After that, for a deeper understanding of the method, the application of the LSFEM on an one-dimensional example is considered. Here, starting from the governing differential equation all steps up to the solution of a simple boundary value problem are discussed in detail. As the least-squares mixed finite element method is not restricted to the LBB-condition, in the following different element types are provided and the resulting number of degree of freedom per element are given. Furthermore, some remarks are given on the application of boundary conditions for the different field quantities. Therefore, the difference between the application of boundary conditions for the two element types (RT_mP_k and P_mP_k) is shown by a simple example. Finally, in this Section some remarks on the implementation are given. Therefore, individual parts of the codes are shown to give a brief overview over the implementations in AceGen. In **Section 5** several numerical benchmark problems are taken under consideration. First the example of a cantilever beam shows the performance of the formulation considering different interpolation orders as well as different element types (RT_mP_k and P_mP_k). In the following the influence of the scalar weighting factor ω_3 on the performance considering this bending dominated problem is shown. The next boundary value problem under consideration is the Cook's

Membrane problem. Here, the distribution of the stresses of a least-squares finite element is compared to a standard and a mixed Galerkin element. Furthermore, using this example, the ability of the method to compute support reactions is investigated. The following example of a quartered plate aims to show the performance of the different element types with respect to the computation of stresses for a boundary value problem consisting of different materials. In addition to that the benchmark of the compression test is provided, compare Reese and Wriggers [2000]. As a three-dimensional example the benchmark problem of a clamped plate is taken under consideration. Finally, the performance of the least-squares formulation under assumption of a transversely isotropic material is investigated.

The locking phenomena could be an important issue for finite element formulations. Therefore, in **Section 6**, the influence of a raise of the Lamé paramter λ (respectively the Poisson's ration $\nu \to 0.5$) which is the so-called volumetric locking or Poisson's locking, is investigated. Therefore, the term "locking" is defined and the influence to the provided least-squares mixed finite element is tested by means of a numerical example.

As the least-squares functional is usable as an error indicator, the application of adaptive mesh refinement is a cost-effective method to improve the performance of the elements. In **Section 7**, after a brief introduction into the theory of adaptive mesh refinement, two different marking strategies are presented. In the following, the benchmark problem of a plate with a hole is considered. There, a regular mesh refinement as well as an adaptive mesh refinement is used for the computation of the result. For comparison the resultant convergence rates are taken under consideration.

Due to stability issues for several mixed finite element formulations presented in Auricchio et al. [2010] and Auricchio et al. [2013], in **Section 8** the ability of the provided element formulation for the computation of stability points for several numerical examples are shown. As the least-squares method, due to its structure, cannot produce negative eigenvalues, a different definition for the detection of the critical loads is neccesary. Therefore, the definition of Müller et al. [2014] is used and the results are compared to a standard Galerkin element.

Finally, in **Section 9** the discussed topics are summarized and a conclusion is drawn concerning the obtained findings. Furthermore, at the end of this work, an outlook is given pointing out further issues, which could be discussed in future work.

2 Continuum mechanical background

In the field of computational mechanics mostly materials are assumed to be a continuum. The real material structure is in general inhomogeneous at least on an atomistic level. But even on higher scales (as e.g. on the microscopic level) the material properties are not continuous (as e.g. different grain size distributions). However, the simplification to a continuous material and the disregard of the microstrucure leads, in general, to sufficiently accurate results for the prediction of the physical behavior. Therefore, certain field quantities as e.g. the displacements or the stresses replace the complex behavior of the real physical body. Due to the definition as a continuum the complete material behavior can be described in an inner material point of the domain, which contains all physical state quantities. The assumption of a physical body as continuous medium is the basis for the so-called continuum mechanics, which fundamentals can be found in Truesdell and Toupin [1960], Truesdell and Noll [1965] and Eringen [1967]. Further general continuum mechanical literature is given e.g. by Marsden and Hughes [1994], Stein and Barthold [1996], Šilhavý [1997], Holzapfel [2000], Truesdell and Noll [2004] and Parisch [2013]. The present work is restricted to solid bodies which are assumed to be a continuum and purely elastic. First, the necessary kinematical quantities and deformation measures will be introduced. Furthermore, several stress quantities will be presented. In the next subsection different hyperelastic free energy functions will be given. In the framework of this work the derivations of the balance principles and the entropy inequality are omitted and the interested reader is referred to standard textbooks as e.g. Holzapfel [2000] or Wriggers [2001].

2.1 Kinematics and deformation measures

For the description of an arbitrary movement of a body in space its kinematics has to be defined. Therefore, a continuous body in the so-called "reference configuration" $\mathcal{B}_0 \subset \mathbb{R}^3$, with the Euclidian space $\mathbb{R}^3$, parametrized in $\boldsymbol{X}$, with the boundary $\partial\mathcal{B}_0$ is defined. Each material point (particle) of the body $\mathcal{B}_0$ (the location) can be described by its position vector $\boldsymbol{X}$. If this body undergoes movements in terms of deformations, translations and/or rotations the body changes its position to new ones at time $t \in \mathbb{R}_+$, where the position of each particle of the body can be described by a position vector $\boldsymbol{x}_t$. These configurations of the body $\mathcal{B}_t \subset \mathbb{R}^3$ with the boundary $\partial\mathcal{B}_t$ are called "current configurations". The motion (mapping) between reference and current configuration is then given by

$$\boldsymbol{x}_t(\boldsymbol{X}, t) = \varphi(\boldsymbol{X}, t) : \mathcal{B}_0 \rightarrow \mathcal{B}_t \,, \tag{1}$$

which maps every point $\boldsymbol{X} \in \mathcal{B}_0$ to a point $\boldsymbol{x} \in \mathcal{B}_t$. In the following, for simplification, further derivations are restricted on one current placement at a fixed time t and neglect, for quantities referring to the current placement, the subscript t leading to

$$\boldsymbol{x}(\boldsymbol{X}) = \varphi(\boldsymbol{X}) : \mathcal{B}_0 \rightarrow \mathcal{B}. \tag{2}$$

The arising displacement is given by $\boldsymbol{u}(\boldsymbol{x}) = \boldsymbol{x} - \boldsymbol{X}$. On both bodies an infinitesimal line, vectorial area and volume element $\mathrm{d}\boldsymbol{X}$, $\mathrm{d}\boldsymbol{A}$ and $\mathrm{d}V$ (on $\mathcal{B}_0$) respectively $\mathrm{d}\boldsymbol{x}$, $\mathrm{d}\boldsymbol{a}$ and $\mathrm{d}v$ (on $\mathcal{B}_t$) can be defined, see also Figure 1.

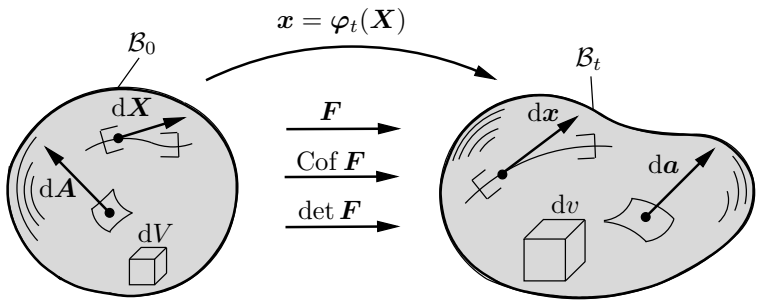

Figure 1: Mappings of the infinitesimal line, area and volume elements, $\boldsymbol{F} : \mathrm{d}\boldsymbol{X} \mapsto \mathrm{d}\boldsymbol{x}$, $\mathrm{Cof}\,\boldsymbol{F} : \mathrm{d}\boldsymbol{A} \mapsto \mathrm{d}\boldsymbol{a}$ and $\det \boldsymbol{F} : \mathrm{d}V \mapsto \mathrm{d}v$.

The current position vector $\boldsymbol{x}$ is given as

$$\boldsymbol{x} = \boldsymbol{X} + \boldsymbol{u}\,. \tag{3}$$

With this in hand, the deformation gradient $\boldsymbol{F}$, a fundamental kinematical quantitiy defined as the gradient of the mapping $\varphi(\boldsymbol{X})$ in Equation (2) with respect to the coordinates $\boldsymbol{X}$, is given as

$$\boldsymbol{F} = \frac{\partial \varphi}{\partial \boldsymbol{X}} = \frac{\partial \boldsymbol{x}}{\partial \boldsymbol{X}} = \mathbf{I} + \nabla \boldsymbol{u}\,. \tag{4}$$

Here, ∇ denotes the gradient with respect to the reference configuration. The deformation gradient can be used for the mapping between the reference and the current configuration. The mapping between an infinitesimal line element in the reference configuration $\mathrm{d}\boldsymbol{X}$ and an infinitesimal line element $\mathrm{d}\boldsymbol{x}$ in the current configuration is given by

$$\mathrm{d}\boldsymbol{x} = \boldsymbol{F}\,\mathrm{d}\boldsymbol{X}\,. \tag{5}$$

With two independent infinitesimal line elements denoted by

$$\mathrm{d}\boldsymbol{x} = \boldsymbol{F}\,\mathrm{d}\boldsymbol{X} \quad \text{and} \quad \mathrm{d}\boldsymbol{y} = \boldsymbol{F}\,\mathrm{d}\boldsymbol{Y}\,, \tag{6}$$

an infinitesimal vectorial area element $\mathrm{d}\boldsymbol{a}$ can be defined given by the cross product

$$\mathrm{d}\boldsymbol{a} = \mathrm{d}\boldsymbol{x} \times \mathrm{d}\boldsymbol{y}\,. \tag{7}$$

For the mapping of the area element from the reference to the current configuration with

$$\mathrm{d}\boldsymbol{A} = \boldsymbol{N}\,\mathrm{d}A \quad \text{and} \quad \mathrm{d}\boldsymbol{a} = \boldsymbol{n}\,\mathrm{d}a \tag{8}$$

and Equation (6) and Equation (7)

$$\mathrm{d}\boldsymbol{a} = (\boldsymbol{F}\,\mathrm{d}\boldsymbol{X}) \times (\boldsymbol{F}\,\mathrm{d}\boldsymbol{Y}) = \mathrm{Cof}[\boldsymbol{F}]\;(\mathrm{d}\boldsymbol{X} \times \mathrm{d}\boldsymbol{Y}) = \mathrm{Cof}[\boldsymbol{F}]\;\mathrm{d}\boldsymbol{A} \tag{9}$$

is obtained, with $\boldsymbol{N}$ and $\boldsymbol{n}$ as the unit normal vectors of the associated area elements. Here, Cof $\boldsymbol{F}$ denotes the cofactor given as

$$\text{Cof}\,\boldsymbol{F} = \det[\boldsymbol{F}]\boldsymbol{F}^{-T}\,,$$

under the assumption of an invertible deformation gradient

$$\boldsymbol{F}^{-1} = \frac{\partial \boldsymbol{X}}{\partial \boldsymbol{x}}. \tag{10}$$

An infinitesimal volume element in the reference configuration $\mathrm{d}V = \mathrm{d}\boldsymbol{A} \cdot \mathrm{d}\boldsymbol{Z}$ can be mapped to an infinitesimal volume element in the current configuration $\mathrm{d}v = \mathrm{d}\boldsymbol{a} \cdot \mathrm{d}\boldsymbol{z}$ using the determinant of the deformation gradient

$$\mathrm{d}v = J\ \mathrm{d}V\,,$$

where J denotes the determinant of the deformation gradient $J = \det \boldsymbol{F}$. All described mappings are depicted in Figure 1.

Since the deformation gradient $\boldsymbol{F}$ includes rigid body rotations and can be split in a left and right stretch tensor ($\boldsymbol{V}$, $\boldsymbol{U}$) and an orthogonal rotation tensor $\boldsymbol{R}$ it can be written as

$$\boldsymbol{F} = \boldsymbol{R}\boldsymbol{U} = \boldsymbol{V}\boldsymbol{R}\,. \tag{11}$$

Further deformation measures, which are free from rigid body rotations and just account for the pure stretch part of the defomation are the nonlinear deformation measures

$$\boldsymbol{C} = \boldsymbol{F}^T\boldsymbol{F} = \boldsymbol{U}^2 \quad \text{and} \quad \boldsymbol{b} = \boldsymbol{F}\boldsymbol{F}^T = \boldsymbol{V}^2. \tag{12}$$

$\boldsymbol{C}$ is denoted as right Cauchy-Green deformation tensor and $\boldsymbol{b}$ as left Cauchy-Green deformation tensor (respectively Finger tensor). Another deformation measure is the Green-Lagrange strain tensor $\boldsymbol{E}$, given as

$$\boldsymbol{E} = \frac{1}{2}(\boldsymbol{C} - \mathbf{I}) = \frac{1}{2}(\nabla\boldsymbol{u} + (\nabla\boldsymbol{u})^T + (\nabla\boldsymbol{u})^T\nabla\boldsymbol{u}). \tag{13}$$

For the description of hyperelastic material behavior a so-called Helmholtz free energy function $\psi(\boldsymbol{F})$ respectively the appropriate strain energy density $W(\boldsymbol{F}) = \rho_0\psi(\boldsymbol{F})$ defined per unit volume with the reference density ρ_0 is used. As it is important, that the description of the material behavior is invariant with respect to superimposed rigid body rotations onto the spatial placement, the principle of material frame indifference (principle of objectivity) has to be satisfied. Using the right Cauchy-Green tensor $\boldsymbol{C}$ as deformation measure in the free energy function, the principle is fulfilled, compare e.g. Truesdell and Noll [1965]. Therefore the principle of material symmetry has to be fulfilled, compare also Schröder et al. [2016]. Hence, the hyperelastic free energy is written in terms of the principal invariants (respectively the main invariants) of the right Cauchy-Green deformation tensor given as

$$I_1 = \operatorname{tr}\boldsymbol{C}, \quad I_2 = \operatorname{tr}[\text{Cof}\,\boldsymbol{C}] = \operatorname{tr}[\det[\boldsymbol{C}]\boldsymbol{C}^{-1}], \quad I_3 = \det\boldsymbol{C} = J^2 \tag{14}$$

respectively

$$J_1 = \text{tr } \boldsymbol{C}, \quad J_2 = \text{tr}[\boldsymbol{C}^2], \quad J_3 = \text{tr}[\boldsymbol{C}^3]. \tag{15}$$

Both types of invariants can be transferred into each other. In the following also transverse isotropic hyperelastic materials are taken under consideration. Therefore, the mixed invariants

$$I_4 = \text{tr}[\boldsymbol{C}\boldsymbol{M}] \quad \text{and} \quad I_5 = \text{tr}[\text{Cof}[\boldsymbol{C}]\boldsymbol{M}]\,, \tag{16}$$

have to be introduced. Here $\boldsymbol{M}$ denotes a structural tensor given by

$$\boldsymbol{M} = \boldsymbol{a} \otimes \boldsymbol{a}\,, \tag{17}$$

with $\boldsymbol{a}$ denoting the preferred direction in the reference configuration and $|\boldsymbol{a}| = 1$. For detailed discussions about the construction of hyperelastic free energy functions, coercivity, convecxity and further informations about the satisfaction of the latter mentioned principles the reader is referred to e.g. Schröder and Neff [2001; 2003], Schröder and Neff [2003], Balzani [2006], Schröder et al. [2008], Schröder [2010] and Ebbing [2010].

2.2 Stress quantities

The application of a load on a solid body leads to an internal reaction force respectively an associated internal stress field. Considering a cutting plane through the body with a normal $\boldsymbol{N}$ in the reference configuration respectively $\boldsymbol{n}$ in the current configuration leads to a representation of the inner stresses by a traction vector $\boldsymbol{T}$ (respectively $\boldsymbol{t}$). With the theorem of Cauchy the traction vectors are obtained as

$$\boldsymbol{T} = \boldsymbol{P}\boldsymbol{N} \quad \text{respectively} \quad \boldsymbol{t} = \boldsymbol{\sigma}\boldsymbol{n}\,, \tag{18}$$

with the first Piola-Kirchhoff stress tensor $\boldsymbol{P}$ and the Cauchy stress tensor $\boldsymbol{\sigma}$. $\boldsymbol{P}$ is an unsymmetric tensor and relates the true stress to the undeformed (reference) area, whereas $\boldsymbol{\sigma}$ denotes the true physical stress (with respect to the current area). The transformation between the Cauchy stress $\boldsymbol{\sigma}$ and the first Piola-Kirchhoff stress tensor $\boldsymbol{P}$ is given as

$$\boldsymbol{P} = J\boldsymbol{\sigma}\boldsymbol{F}^{-T} \tag{19}$$

using $\boldsymbol{T}\,\mathrm{d}A = \boldsymbol{t}\,\mathrm{d}a$, Equation (9) and Equation (8).

In order to obtain a symmetric measure the second Piola-Kirchhoff stress tensor $\boldsymbol{S}$ is introduced, which is completely related to the reference configuration

$$\boldsymbol{S} = \boldsymbol{F}^{-1}\boldsymbol{P}\,. \tag{20}$$

A further stress quantitiy is the so-called Kirchhoff stress tensor $\boldsymbol{\tau}$ given as

$$\boldsymbol{\tau} = J\boldsymbol{\sigma} = \boldsymbol{P}\boldsymbol{F}^{T}\,. \tag{21}$$

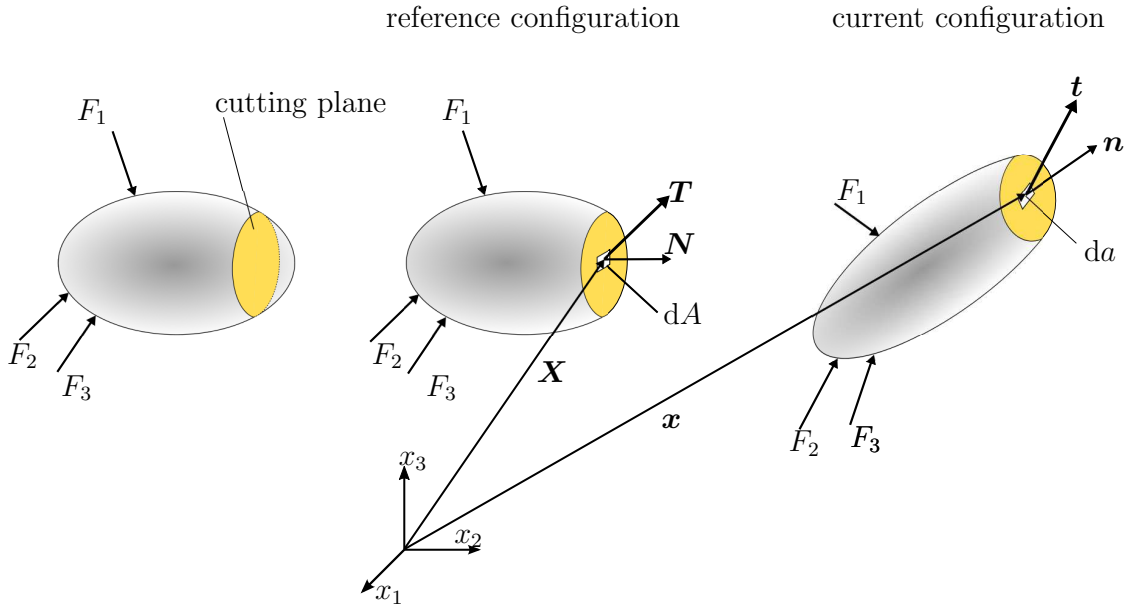

Figure 2: Body with cutting plane and internal stress vectors $\boldsymbol{T}$ and $\boldsymbol{t}$.

Out of the requirement of a thermodynamically consistent material, the Clausius-Duhem inequality has to be satisfied, see e.g. Truesdell and Noll [1965], and the relations between the stress tensors and the free energy function are obtained as

$$\boldsymbol{P} = \rho_0 \frac{\partial \psi}{\partial \boldsymbol{F}}, \quad \boldsymbol{S} = 2\rho_0 \frac{\partial \psi}{\partial \boldsymbol{C}}. \tag{22}$$

2.3 Hyperelastic materials

Materials which behave purely elastic also in the case of large strain and can be described by a strain energy potential ensuring no energy generation or dissipative in a closed cycle are called hyperelastic. In the framework of this contribution several free energy functions will be considered in order to describe the stress response of the material. Therefore, the derivative of the free energy function based on the invariants of the right Cauchy-Green deformation tensor $\boldsymbol{C}$, see Equation (14), is used. The free energy functions have to satisfy the condition of a stress free reference configuration ($\boldsymbol{S}|_{\boldsymbol{C}=\mathbf{I}} = \mathbf{0}$) and the associated Lagrangian moduli

$$\mathbb{C} = 4\rho_0 \frac{\partial^2 \psi}{\partial \boldsymbol{C} \partial \boldsymbol{C}}, \tag{23}$$

has to be equal to the fourth order tensor for linear elasticity for the unloaded reference configuration ($\mathbb{C}|_{\boldsymbol{C}=1} = \mathbb{C}^{le}$) given as

$$\mathbb{C}^{le} = \frac{\partial^2 \psi(\boldsymbol{\varepsilon})}{\partial \boldsymbol{\varepsilon} \partial \boldsymbol{\varepsilon}} = \lambda \, \mathbf{I} \otimes \mathbf{I} + 2\mu \, \mathbf{II}, \tag{24}$$

with the linear strain tensor

$$\boldsymbol{\varepsilon} = \frac{1}{2}(\nabla \boldsymbol{u} + \nabla^T \boldsymbol{u})\,, \tag{25}$$

the strain energy for linear elastic solids

$$\psi(\boldsymbol{\varepsilon}) = \frac{1}{2}\lambda(\operatorname{tr}\boldsymbol{\varepsilon})^2 + \mu \operatorname{tr}\boldsymbol{\varepsilon}^2 \tag{26}$$

and the Lamé parameters λ and μ.

Here, the index representations of the identity tensors of second ($\mathbf{I}$) and fourth order ($\mathbb{I}$) are given as

$$\mathrm{I}_{ij} = \delta_{ij} \quad \text{and} \quad \mathbb{I}_{ijkl} = \delta_{ik}\delta_{jl}\,, \tag{27}$$

where δ_{ij} denotes the Kronecker Delta.

2.3.1 Neo-Hookean The isotropic free energy functions of Neo-Hookean type are given in terms of the first and third principal invariant of the right Cauchy-Green deformation tensor $\boldsymbol{C}$, see Equation (14), as

$$\begin{aligned} 1)\quad \psi^{iso}_{NH}(I_1, I_3) &= \frac{\mu}{2}(I_1 - 3) + \frac{\lambda}{4}(I_3 - 1) - \left(\frac{\lambda}{2} + \mu\right)\ln(\sqrt{I_3})\,, \\ 2)\quad \psi^{iso}_{NH}(I_1, I_3) &= \frac{\mu}{2}(I_1 - 3) - \mu \ln\sqrt{I_3} + \frac{\lambda}{2}\left(\theta(J)\right)^2\,, \end{aligned} \tag{28}$$

compare for Equation (28.1) e.g. Wriggers [2001] and for Equation (28.2) Auricchio et al. [2013] with different expressions for $\theta(J)$ given as

$$a)\,\theta(J) = J - 1\,, \qquad b)\,\theta(J) = \ln J \qquad \text{and} \qquad c)\,\theta(J) = 1 - \frac{1}{J}\,. \tag{29}$$

This leads to different expressions for the second Piola-Kirchhoff stress tensor $\boldsymbol{S}$, given as the derivative of the free energy with respect to the right Cauchy-Green deformation gradient $\boldsymbol{C}$ multiplied by two, see also Equation (22) with $\rho_0 = 1$. Using the derivatives of the principal invariants, see Wriggers [2001], given as

$$\frac{\partial I_1}{\partial \boldsymbol{C}} = \mathbf{I}\,, \quad \frac{\partial I_2}{\partial \boldsymbol{C}} = I_1\mathbf{I} - \boldsymbol{C} \quad \text{and} \quad \frac{\partial I_3}{\partial \boldsymbol{C}} = I_3 \boldsymbol{C}^{-1}\,, \tag{30}$$

leads to

$$\begin{aligned} &1) \quad \boldsymbol{S} = \mu\,(\mathbf{I} - \boldsymbol{C}^{-1}) + \frac{\lambda}{2}\,(I_3 - 1)\,\boldsymbol{C}^{-1}\,, \quad 2a) \quad \boldsymbol{S} = \mu\,(\mathbf{I} - \boldsymbol{C}^{-1}) - \frac{\lambda}{2}\sqrt{I_3}\boldsymbol{C}^{-1}\,, \\ &2b) \quad \boldsymbol{S} = \mu\,(\mathbf{I} - \boldsymbol{C}^{-1}) - \frac{\lambda}{2}\boldsymbol{C}^{-1} \quad \text{and} \qquad 2c) \quad \boldsymbol{S} = \mu\,(\mathbf{I} - \boldsymbol{C}^{-1}) + \frac{\lambda}{2}\frac{1}{\sqrt{I_3}}\boldsymbol{C}^{-1}\,. \end{aligned} \tag{31}$$

The first Piola-Kirchhoff stress tensor can then be computed using the relation $\boldsymbol{P} = \boldsymbol{F}\boldsymbol{S}$.

2.3.2 Mooney-Rivlin A special case of an Ogden type material, compare Ogden [1984] is the compressible Mooney-Rivlin material (compare e.g. Ciarlet and Geymonat [1982] respectively Schröder et al. [2016]),

$$\psi_{MR}^{iso} = \alpha_1 I_1 + \eta_1 I_2 + \delta_1 I_3 - \delta_2 \ln(\sqrt{I_3})\,, \tag{32}$$

with

$$\alpha_1 = \frac{1}{4}(\lambda + 2\mu + \lambda(\xi - 2))\,, \quad \eta_1 = \frac{1}{4}\lambda(1 - \xi)\,, \quad \delta_1 = \frac{\lambda\xi}{4}\,, \quad \delta_2 = \frac{1}{2}(\lambda + 2\mu)\,, \tag{33}$$

and $\xi \in (0, 1)$. In the framework of this thesis the value is chosen as $\xi = \frac{1}{2}$. The second Piola-Kirchhoff stress tensor $\boldsymbol{S}$ can be computed as

$$\boldsymbol{S} = (2\alpha_1 + 2\eta_1 I_1)\mathbf{I} - 2\eta_1 \boldsymbol{C} + (2\delta_1 - \frac{\delta_2}{I_3})\,\mathrm{Cof}\,\boldsymbol{C}\,. \tag{34}$$

2.3.3 Transverse isotropic hyperelasticity As the isotropic basis of the material behavior the free energy given in equation (28.1) is used for the proposed formulation. Adding a transverse isotropic part in terms of the mixed invariant J_4, see Equation (16), the transverse isotropic free energy is obtained as

$$\psi_{NH}^{ti} = \frac{\lambda}{4}\,(I_3 - 1) - (\frac{\lambda}{2} + \mu)\ln(\sqrt{I_3}) + \frac{\mu}{2}\,(I_1 - 3) + \alpha_1 \big\langle J_4 - 1 \big\rangle^{\alpha_2}\,, \tag{35}$$

with the definition of the Macauly brackets

$$\big\langle \beta \big\rangle := \frac{1}{2}(\beta + |\beta|)\,, \tag{36}$$

and the requirement of the parameters $\alpha_1 \geq 0$ and $\alpha_2 > 1$, see Balzani et al. [2006]. The reason for the choice of the Macauly brackets is due to the fact, that only an elongation of the fibers generates stresses.

The second Piola-Kirchhoff stress tensor $\boldsymbol{S}$ is then given as

$$\boldsymbol{S} \;=\; \mu\,(\mathbf{I} - \boldsymbol{C}^{-1}) + \frac{\lambda}{2}\,(I_3 - 1)\,\boldsymbol{C}^{-1} + 2\alpha_2\alpha_1 \big\langle J_4 - 1 \big\rangle^{\alpha_2 - 1}\boldsymbol{M}\,. \tag{37}$$

For a better overview, in Equation (38) several fundamental differential equations, tensors and their relations used in this thesis are summarized.

Deformation gradient	$\boldsymbol{F} = \mathbf{I} + \nabla \boldsymbol{u}$
Right Cauchy-Green deformation tensor	$\boldsymbol{C} = \boldsymbol{F}^T \boldsymbol{F}$
Principal invariants of $\boldsymbol{C}$	$I_1 = \operatorname{tr} \boldsymbol{C}, \quad I_2 = \operatorname{tr}[\operatorname{Cof} \boldsymbol{C}], \quad I_3 = \det \boldsymbol{C}$
Mixed invariants	$I_4 = \operatorname{tr}[\boldsymbol{C}\boldsymbol{M}], \quad I_5 = \operatorname{tr}[\operatorname{Cof}[\boldsymbol{C}]\boldsymbol{M}]$
Free energy function	$\psi(\boldsymbol{C})$
1st Piola Kirchhoff stress tensor	$\boldsymbol{P} = \rho_0 \dfrac{\partial \psi}{\partial \boldsymbol{F}}$
2nd Piola Kirchhoff stress tensor	$\boldsymbol{S} = \boldsymbol{S}^T = 2\rho_0 \dfrac{\partial \psi}{\partial \boldsymbol{C}} = \boldsymbol{F}^{-1}\boldsymbol{P}$
Balance of momentum (static case)	$\operatorname{Div} \boldsymbol{P} + \boldsymbol{f} = \mathbf{0}$

(38)

3 Interpolation

For the approximation of quantities in the framework of the FEM appropriate interpolation functions have to be chosen. The choice of the functions is dependent on the interpolation spaces, which are described in Section 3.1. In the following the interpolation functions used for the least-squares mixed finite element formulations are presented. Here, it is differentiated between standard interpolation polynomials of Lagrangian type (Section 3.2), which ensure conforming discretizations of $W^{1,p}(\mathcal{B})$ and vector-valued Raviart-Thomas interpolation functions (Section 3.3) which ensure conforming discretizations of $W^q(\mathrm{div}, \mathcal{B})$.

3.1 Interpolation spaces

The mixed least-squares finite element formulations presented in this contribution are based on displacement-stress functionals. Hence, the solution variables are the displacements ($\boldsymbol{u}$) and the stresses ($\boldsymbol{P}$). For the interpolation of these unknowns suitable approximation spaces have to be chosen. For the displacements $W^{1,p}(\mathcal{B})$ is an appropriate choice due to its restrictions that the unknown function as well as their derivative have to fulfill the $L^p(\mathcal{B})$-norm

$$|| \bullet ||_{L^p(\mathcal{B})} = \sqrt[p]{\int_{\mathcal{B}} | \bullet |^p \, \mathrm{d}V} \,. \tag{39}$$

This leads to the definition of the Sobolev space

$$W^{1,p}(\mathcal{B}) = \{ \boldsymbol{u} \in L^p(\mathcal{B}) : \nabla \boldsymbol{u} \in L^p(\mathcal{B}) \} \,,$$

with $||\boldsymbol{u}||_{L^p(\mathcal{B})} < \infty$ and $||\nabla \boldsymbol{u}||_{L^p(\mathcal{B})} < \infty$. For the interpolation of the stresses the space $W^q(\mathrm{div}, \mathcal{B})$ is a suitable choice, compare e.g. Müller et al. [2014]. The restriction here are that the function as well its divergence has to fulfill the $L^q(\mathcal{B})$-norm. With this in hand the Sobolev space

$$W^q(\mathrm{div}, \mathcal{B}) = \{ \boldsymbol{P} \in L^q(\mathcal{B})^2 : \mathrm{div}\ \boldsymbol{P} \in L^q(\mathcal{B}) \} \,,$$

is obtained. Dependent on the formulation, p and q have to be chosen suitable under consideration of the restriction $p \leq q \leq 2$. In the case of linear elastic problems, $p = 2$ and $q = 2$ can be chosen leading to the Sobolev spaces $W^{1,2}(\mathcal{B}) = H^1(\mathcal{B})$ and $W^2(\mathrm{div}, \mathcal{B}) = H(\mathrm{div}, \mathcal{B})$. Furthermore, an approximation of the stresses in $W^{1,p}(\mathcal{B})$ is also taken under consideration, see also Chapter 4.5, where also the correlation of the interpolation spaces to each other is shown in Equation (113). In the following subsection the interpolation functions, which guarantee a conforming discretization of the above mentioned Sobolev spaces, are provided.

3.2 Discretization of $W^{1,p}(\mathcal{B})$

For the interpolation of quantities where the function $\boldsymbol{u}(\boldsymbol{x})$ as well as the derivative $\boldsymbol{u}'(\boldsymbol{x})$ have to satisfy the $L^p(\mathcal{B})$-norm

$$||\boldsymbol{u}||_{L^p(\mathcal{B})} < \infty \quad \text{and} \quad ||\boldsymbol{u}'||_{L^p(\mathcal{B})} < \infty \,, \tag{40}$$

standard interpolation polynomials of Lagrangian type are chosen. In the following the construction of these polynomials in two dimensions for a triangular finite element domain in the parameter space $\boldsymbol{\xi} = (\xi, \eta)^T$ is considered. Therefore, the general polynomial is given as

$$N(\xi, \eta) = a_1 + a_2\xi + a_3\eta + a_4\xi^2 + a_5\xi\eta + a_6\eta^2 \ldots . \tag{41}$$

The related monomials can be identified, for instance, using the Pascal's triangle, see Figure 3 respectively e.g. Zhu et al. [2005], by choosing, starting from the top row up to the $(k+1)$-th row the necessary terms.

$$\begin{array}{ccccccccccc}
 & & & & 1 & & & & & & \\
 & & & & \xi & & \eta & & & & \\
 & & & \xi^2 & & \xi\eta & & \eta^2 & & & \\
 & & \xi^3 & & \xi^2\eta & & \xi\eta^2 & & \eta^3 & & \\
 & \xi^4 & & \xi^3\eta & & \xi^2\eta^2 & & \xi\eta^3 & & \eta^4 & \\
\xi^5 & & \xi^4\eta & & \xi^3\eta^2 & & \xi^2\eta^3 & & \xi\eta^4 & & \eta^5 \\
. & & . & & . & & . & & . & & . \\
. & & . & & . & & . & & . & & .
\end{array}$$

Figure 3: Pascal's triangle for the monomials for two-dimensional interpolation functions.

In order to construct the interpolation functions N^I for each interpolation site I (associated to a node) a system of equations is solved, enforcing that the interpolation polynomial has to be one at the respective node coordinates and zero at all other nodes

$$N^I(\xi_J, \eta_J) = \begin{cases} 1, & \text{for } I = J \\ 0, & \text{for } I \neq J \end{cases} \tag{42}$$

with the nodal coordinates $(\xi_J, \eta_J)^T$. For instance for the first node the system of equations

$$\begin{aligned}
& a_1^1 + a_2^1\xi_1 + a_3^1\eta_1 + a_4^1\xi_1^2 + a_5^1\xi_1\eta_1 + a_6^1\eta_1^2 \ldots = 1 \\
\wedge\ & a_1^1 + a_2^1\xi_2 + a_3^1\eta_2 + a_4^1\xi_2^2 + a_5^1\xi_2\eta_2 + a_6^1\eta_2^2 \ldots = 0 \\
\wedge\ & a_1^1 + a_2^1\xi_3 + a_3^1\eta_3 + a_4^1\xi_3^2 + a_5^1\xi_3\eta_3 + a_6^1\eta_3^2 \ldots = 0 \\
\wedge\ & \ldots
\end{aligned} \tag{43}$$

is obtained, from which the coefficients a_i^1 are computed. By solving the system of equations with respect to a changed right-hand side vector (the position of the "one" is changing) the seeked coefficients a_i^I are obtained. Inserting them into the general form of the interpolation polynomial (41) yields the function for each interpolation site.

3.3 Discretization of $W^q(\mathrm{div}, \mathcal{B})$

For the interpolation of quantities where the function $\boldsymbol{P}$ as well as the divergence $\mathrm{Div}\,\boldsymbol{P}$ have to satisfy the $L^q(\mathcal{B})$-norm (39)

$$||\boldsymbol{P}||_{L^q(\mathcal{B})} < \infty \quad \text{and} \quad ||\operatorname{Div} \boldsymbol{P}||_{L^q(\mathcal{B})} < \infty\,, \tag{44}$$

vector-valued Raviart-Thomas interpolation functions Ψ_m^J where m denotes the interpolation order and J the associated interpolation site are chosen. The feature of these function is, that the resulting interpolation is normal continuous, i.e. the normal component(s) of the interpolated field (field quantity multiplied by associated normal) are interpolated continuously, compare e.g. Raviart and Thomas [1977] or Ervin [2012], respectively. Thus, in case of the interpolation of the stresses using this functions, the normal entries of the stress tensor (the so-called traction vector $\boldsymbol{PN}$, compare Chapter 2.2) are continuously interpolated. It is differentiated between outer and inner interpolation sites J^{out} and J^{in}. The total number of interpolation sites is then given as $|J|_{\mathcal{C}} = |J^{out}|_{\mathcal{C}} + |J^{in}|_{\mathcal{C}} = m^2+4m+3$ with $|J^{out}|_{\mathcal{C}} = 3(m+1)$ and $|J^{in}|_{\mathcal{C}} = m(m+1)$. Here, $|A|_{\mathcal{C}}$ denotes the cardinality of the set A, i.e. the number of elements in the set A. The construction is shown for a two-dimensional triangular finite element domain in the parameter space $\boldsymbol{\xi} = (\xi, \eta)^T$. The outer interpolation sites are related to the respective element edges $\hat{e}^L$ (with $|\hat{e}^L|_{\mathcal{C}} = 3$) and their associated normals $\hat{\boldsymbol{n}}^L$ (with $|\hat{\boldsymbol{n}}^L|_{\mathcal{C}} = 3$, $\hat{\boldsymbol{n}}^1 = (1/\sqrt{2}, 1/\sqrt{2})^T$, $\hat{\boldsymbol{n}}^2 = (-1, 0)^T$ and $\hat{\boldsymbol{n}}^3 = (0, -1)^T$) and the inner ones to the triangular domain in a parameter space (ξ, η) denoted by $\hat{\Omega}^e$, see also Figure 4.

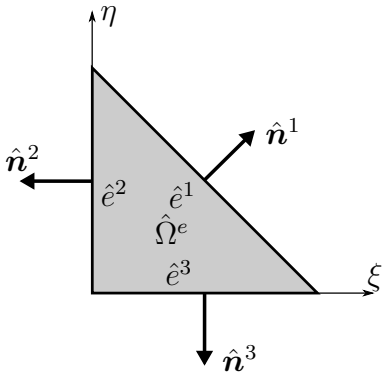

Figure 4: Numbering of edges $\hat{e}^L$ and their associated normals $\hat{\boldsymbol{n}}^L$.

The interpolation order as well as the number of interpolation sites for a two-dimensional triangular element up to order $m = 3$ is given in Table 1. In the framework of this contribution the derivations are restricted to meshes with non-curved edges. An enhancement to curved boundaries has been done in Bertrand et al. [2014].

RT_m	Pol. order of Ψ_m^J	$\lvert J^{out}\rvert_{\mathcal{C}}$ per $\hat{e}^L$	$\lvert J^{out}\rvert_{\mathcal{C}}$	$\lvert J^{in}\rvert_{\mathcal{C}}$	$\lvert J\rvert_{\mathcal{C}}$
RT_0	linear	1	3	0	3
RT_1	quadratic	2	6	2	8
RT_2	cubic	3	9	6	15
RT_3	quartic	4	12	12	24

Table 1: Raviart-Thomas setups ($m = 0, 1, 2, 3$) in two dimensions.

The general form of the vectorial basis functions of order m in the parameter space $\boldsymbol{\xi} = (\xi, \eta)^T$ is given by

$$\hat{\boldsymbol{v}}_m(\xi,\eta) = \hat{\boldsymbol{p}}_m(\xi,\eta) + \hat{p}_m(\xi,\eta) \begin{pmatrix} \xi \\ \eta \end{pmatrix}, \tag{45}$$

where $\hat{p}_m, \hat{\boldsymbol{p}}_m$ are general scalar-valued and vectorial functions of order m with J unknown coefficients $(a, b, c, ...)$, see exemplary Equation (55). For the construction the expressions

$$\begin{aligned} M_{out}^{L,K} &= \int_{\hat{e}^L} (\hat{\boldsymbol{v}}_m \cdot \hat{\boldsymbol{n}}^L)\, \hat{q}_m^{L,K}\, ds \\ \text{and (for } m \geq 1) \qquad M_{in}^{I} &= \int_{\hat{\Omega}^e} \hat{\boldsymbol{v}}_m \cdot \hat{\boldsymbol{q}}_{m-1}^{I}\, da \end{aligned} \tag{46}$$

have to be evaluated for each interpolation site J, that means for each $\hat{\boldsymbol{n}}^L$, $\hat{q}_m^{L,K}$ and $\hat{\boldsymbol{q}}_{m-1}^{I}$. Here, $\hat{q}_m^{L,K}, \hat{\boldsymbol{q}}_{m-1}^{I}$ are explicit, scalar-valued and vectorial functions of order m and $m-1$ corresponding to the interpolation site J, which have to be chosen linear independent. The linear independency has to be guaranteed for the inner interpolation sites and the individual edges, independently. With the conditions

$$M_{out}^{L,K}(\hat{\boldsymbol{n}}^O, \hat{q}_m^{OP}) = \begin{cases} 1, & \text{for } L = O \wedge K = P \\ 0, & \text{for } L \neq O \vee K \neq P \end{cases} \tag{47}$$

and

$$M_{in}^{I}(\hat{\boldsymbol{q}}_{m-1}^{P}) = \begin{cases} 1, & \text{for } I = P \\ 0, & \text{for } I \neq P \end{cases} \tag{48}$$

for each interpolation site J a system of equations, which solution are the unknown coefficients, is obtained. $M_{out}^{L,K}$ and M_{in}^{I} are often called "outer" and "inner" moments. These yields, entering in (45), the (linear independent, compare Ciarlet [1991]) vectorial basis functions $\hat{\boldsymbol{v}}_m^J(\xi,\eta)$ for each interpolation site J of the reference triangle. For the transformation of the basis function from the parameter space $(\hat{P}^i, \hat{\boldsymbol{n}}^i, \mathrm{d}\hat{\boldsymbol{A}}, \hat{\boldsymbol{v}}_m^J ...)$ to the physical space $(P^i, \boldsymbol{n}^i, \mathrm{d}\boldsymbol{A}, \boldsymbol{v}_m^J ...)$, see also Figure 5, the requirement, that the flux over the element edges is equal in both configurations has to be fulfilled.

Let $(\mathrm{d}\hat{\boldsymbol{A}}, \mathrm{d}\boldsymbol{A})$ denote the vectorial area element of the parameter and physical space, respectively, then

$$\hat{\boldsymbol{v}}_m^J \cdot \mathrm{d}\hat{\boldsymbol{A}} = \boldsymbol{v}_m^J \cdot \mathrm{d}\boldsymbol{A}\,. \tag{49}$$

is demanded. Now the mapping of the vectorial area element of Equation (9) is inserted and a linear geometry transformation $\boldsymbol{\varphi}_t$ is assumed, see Figure 1. This leads to a constant transformation matrix $\boldsymbol{T}$ associated to the unit triangle in the parameter space $\boldsymbol{\xi}(\xi,\eta)$ and the triangular element in the physical space $\boldsymbol{x}(x_1, x_2)$:

$$\boldsymbol{T} = \frac{\partial \boldsymbol{x}}{\partial \boldsymbol{\xi}} = \begin{pmatrix} -x_1^1 + x_1^2 & -x_1^1 + x_1^3 \\ -x_2^1 + x_2^2 & -x_2^1 + x_2^3 \end{pmatrix} \tag{50}$$

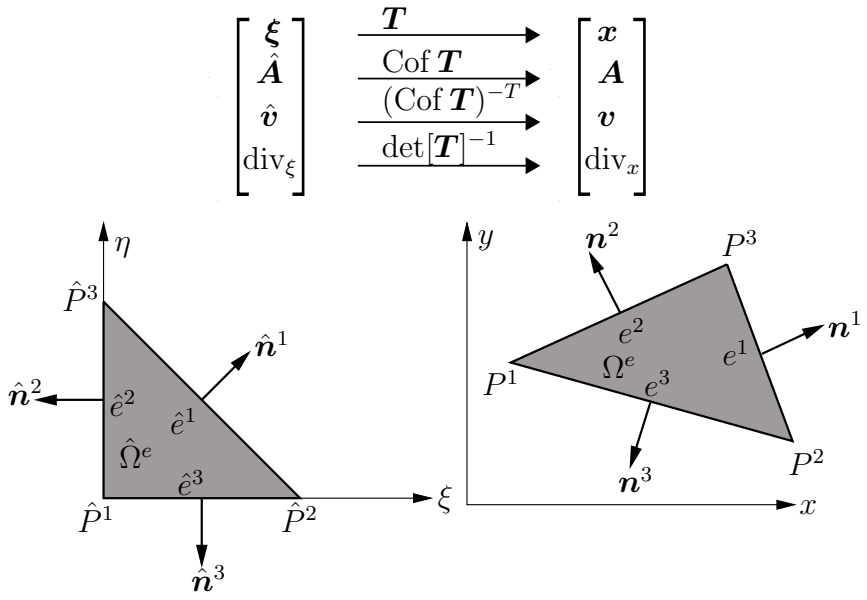

Figure 5: Piola transformation.

with the known coordinates of the vertices $P^I = (x_1^I, x_2^I)$ in the physical space. With this in hand and $\mathrm{Cof}\,\boldsymbol{T} = \det[\boldsymbol{T}]\boldsymbol{T}^{-T}$

$$\hat{\boldsymbol{v}}_m^J = \mathrm{Cof}[\boldsymbol{T}]^T \boldsymbol{v}_m^J \rightsquigarrow \boldsymbol{v}_m^J = \frac{1}{\det \boldsymbol{T}} \boldsymbol{T} \hat{\boldsymbol{v}}_m^J \tag{51}$$

is obtained from Equation (49), which transforms the basis function of the parameter space $\hat{\boldsymbol{v}}_m^J$ to the basis function of the physical space $\boldsymbol{v}_m^J$. Furthermore, the divergence of the basis function has to be transformed. Applying the divergence with respect to the physical space (div_x) on both sides of (51) yields

$$\mathrm{div}_x \boldsymbol{v}_m^J = \mathrm{div}_x [\frac{1}{\det \boldsymbol{T}} \boldsymbol{T} \hat{\boldsymbol{v}}_m^J] = \frac{1}{\det \boldsymbol{T}} \mathrm{div}_\xi \hat{\boldsymbol{v}}_m^J, \tag{52}$$

using the relations

$$\boldsymbol{T}\mathrm{div}_x \hat{\boldsymbol{v}}_m^J = \mathrm{div}_\xi \hat{\boldsymbol{v}}_m^J \quad \text{and} \quad \mathrm{div}_x [\frac{1}{\det \boldsymbol{T}} \boldsymbol{T}] = 0\,, \tag{53}$$

because $\boldsymbol{T}$ is a constant matrix. To obtain the vector-valued Raviart-Thomas interpolation functions Ψ_m^J, a normalization condition on $\boldsymbol{v}_m^J$ has to be applied in order to get suitable functions for Ψ_m^J.

The sum of all Raviart-Thomas shape function Ψ_m^J belonging to one edge multiplied with the associated normal of this edge should be equal to one.

It should be remarked, that a reasonable choice of the functions $\hat{q}_m^{L,K}$, which is recommended by the author, simplifies the generalization of the normalization condition for all interpolation orders m to

$$\Psi_m^J = l\ \boldsymbol{v}_1^J \quad \text{and} \quad \operatorname{div} \Psi_m^J = l\ \operatorname{div} \boldsymbol{v}_1^J\,, \tag{54}$$

where l denotes the associated length of the edge of the interpolation site under consideration. In the following the construction of the interpolation functions for $m = 1$ will be provided. The basic equations for the construction of $m = 2$ and $m = 3$ is given in the Appendix (see Chapter A.1 and Chapter A.2). For the construction for $m = 0$ the reader is referred e.g. to Schwarz [2009].

3.3.1 Basis functions for order $m = 1$. The general form of the vectorial basis function (45) for the order $m = 1$ is given as

$$\hat{\boldsymbol{v}}_1(\xi,\eta) = \underbrace{\begin{pmatrix} a_1 + a_2\xi + a_3\eta \\ b_1 + b_2\xi + b_3\eta \end{pmatrix}}_{\hat{\boldsymbol{p}}_1} + \underbrace{(c_1\xi + c_2\eta)}_{\hat{p}_1} \begin{pmatrix} \xi \\ \eta \end{pmatrix}. \tag{55}$$

Since $m \geq 1$, both parts of (46) have to be evaluated for the interpolation sites $J = 1..8$ leading to eight equations

$$M_{out}^{L,K} \text{ with } L = 1..3, K = 1..2 \quad \text{and} \quad M_{in}^{I} \text{ with } I = 1..2\,. \tag{56}$$

Exemplary the evaluation for the sites $J = 3$ ($M_{out}^{1,1}$) and $J = 8$ (M_{in}^{2}) will be considered in more detail, see Figure 6.

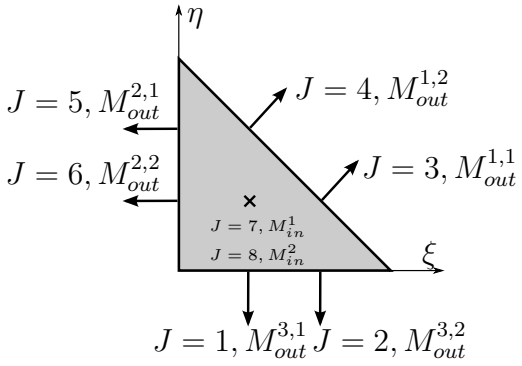

Figure 6: Numbering of interpolation sites J for RT_1.

The complete set of functions $\hat{q}_1^{L,K}$ and $\hat{\boldsymbol{q}}_0^I$ and neccesary additional conditions (correlation of coordinates) for the construction of RT_1 are given in Table 2.

L	K	I	$\hat{q}_1^{L,K}$ / $\hat{\boldsymbol{q}}_0^I$	correlation of coordinates
1	1	-	2ξ	$\eta = 1 - \xi$
1	2	-	2η	$\eta = 1 - \xi$
2	1	-	2η	$\xi = 0$
2	2	-	$2(1-\eta)$	$\xi = 0$
3	1	-	$2(1-\xi)$	$\eta = 0$
3	2	-	2ξ	$\eta = 0$
-	-	1	$(1,0)^T$	-
-	-	2	$(0,1)^T$	-

Table 2: Set of functions $\hat{q}_1^{L,K}$ and $\hat{\boldsymbol{q}}_0^I$ and correlation of coordinates for the construction of RT_1.

$\underline{J = 3,\ M_{out}^{1,1}\textbf{:}}$ Evaluating the first part of (46) with $\hat{\boldsymbol{n}}^1 = \sqrt{\frac{1}{2}} \begin{pmatrix} 1 \\ 1 \end{pmatrix}$, $\hat{q}_1^{1,1} = 2\xi$ and the correlation for the coordinates $\xi + \eta = 1$ leads to

$$\begin{aligned} M_{out}^{1,1} &= \int_{e^1} (\hat{\boldsymbol{v}}_1 \cdot \hat{\boldsymbol{n}}^1)\ \hat{q}_1^{1,1}\ ds \\ &= \int_{e^1} \begin{pmatrix} a_1 + a_2\xi + a_3\eta + c_1\xi^2 + c_2\xi\eta \\ b_1 + b_2\xi + b_3\eta + c_1\xi\eta + c_2\eta^2 \end{pmatrix} \cdot \frac{1}{\sqrt{2}} \begin{pmatrix} 1 \\ 1 \end{pmatrix} 2\xi\, ds \\ &= a_1 + \frac{2a_2}{3} + \frac{a_3}{3} + b_1 + \frac{2b_2}{3} + \frac{b_3}{3} + \frac{2c_1}{3} + \frac{c_2}{3}, \end{aligned} \tag{57}$$

with $ds = \sqrt{2} d\xi$.

$\underline{J = 8,\ M_{in}^2\textbf{:}}$ For this interpolation site $\hat{\boldsymbol{q}}_0^2 = (0,1)^T$ is chosen and, evaluating the second part of (46),

$$\begin{aligned} M_{in}^2 &= \int_{\Omega^e} \hat{\boldsymbol{v}}_m \cdot \hat{\boldsymbol{q}}_0^2\ da \\ &= \int_0^1 \int_0^{1-\eta} \begin{pmatrix} a_1 + a_2\xi + a_3\eta + c_1\xi^2 + c_2\xi\eta \\ b_1 + b_2\xi + b_3\eta + c_1\xi\eta + c_2\eta^2 \end{pmatrix} \begin{pmatrix} 0 \\ 1 \end{pmatrix} d\xi d\eta \\ &= \frac{b_1}{2} + \frac{b_2}{6} + \frac{b_3}{6} + \frac{c_1}{24} + \frac{c_2}{12}, \end{aligned} \tag{58}$$

is obtained. The computations at each interpolation site, as exemplary done for $J = 3$ in Equation (57) and $J = 8$ in Equation (58), yields under consideration of (47) and (48) a system of equations, which has to be solved for each interpolation site J. The right-hand side vector has a non-vanishing entry at the J^{th} entry, which is equal to one. Solving

the system of equations yield the parameter a_i, b_i for $i = 1, 2, 3$ and c_1, c_2 of the vectorial basis functions (55) in the form $(a_1, a_2, a_3, b_1, b_2, b_3, c_1, c_2)^T$. We obtain the coefficients for the eight vectorial basis functions $\hat{\boldsymbol{v}}_1^J$ for the considered RT_1-case as given in Table 3.

	$\hat{v}_1^1$	$\hat{v}_1^2$	$\hat{v}_1^3$	$\hat{v}_1^4$	$\hat{v}_1^5$	$\hat{v}_1^6$	$\hat{v}_1^7$	$\hat{v}_1^8$
a_1	0	0	0	0	1	−2	0	0
a_2	3	−2	−2	−1	−1	6	16	8
a_3	0	0	0	0	−3	3	0	0
b_1	−2	1	0	0	0	0	0	0
b_2	3	−3	0	0	0	0	0	0
b_3	6	−1	−1	−2	−2	3	8	16
c_1	−4	4	4	0	0	−4	−16	−8
c_2	−4	0	0	4	4	−4	−8	−16

Table 3: Set of coefficients for the construction of RT_1.

Now the obtained vector-valued basis functions (as well as their divergences) has to be transformed to the physical space by Equation (51) and Equation (52) and normalized by Equation (54).

3.4 Alternative discretization of $W^q(\mathrm{div}, \mathcal{B})$

It is inconvenient if the nodal degree of freedom respectively the nodal quantity is not equal to the interpolated quantity at this position. Consequently, the nodal results coming from the sytem of equations does not have any physical meaning, which is, at least from an engineering point of view, unsatisfying. Especially if the nodal values are used for postprocessing or for non-constant boundary conditions this property is desirable. Unfortunately, the latter described way of construction does not demand the interpolation function to be one at its nodal coordinates and zero at all other nodes. This leads, for $m \geq 2$, to vector-valued functions, which does not fulfill the condition.

To show this effect, exemplary for RT_2, the interpolation functions are evaluated on a unit triangular domain. In detail the functions are considered for the edge e^3 or rather $\hat{e}^3$, as for the used unit traingle $\Omega^e = \hat{\Omega}^e$. In Figure 7 it can be seen, that the constructed functions have their roots not at the coordinates of the respective interpolation site. Furthermore, the functions are not one at their respective nodes. It should be remarked that this fact does not influence the correctness of the discretization.

In order to overcome this issue, the aim is to develop alternative interpolation functions of Raviart-Thomas type, which fulfill this condition. For the latter approach the evaluation of the outer and inner moments lead to the sought functions. In contrast to that, the alternative approach uses a nodal evaluation of a prescribed condition. Therefore, it has to be started from the general form given in Equation (45) respectively Equation (55), Equation (135) and Equation (137). Now for each outer interpolation site the functions $\hat{\boldsymbol{v}}_m^J$ are sought, which fulfill, multiplied with their associated normal $\hat{\boldsymbol{n}}^L$ and the length $\hat{l}^L$ of the associated site $\hat{e}^L$, the nodal condition

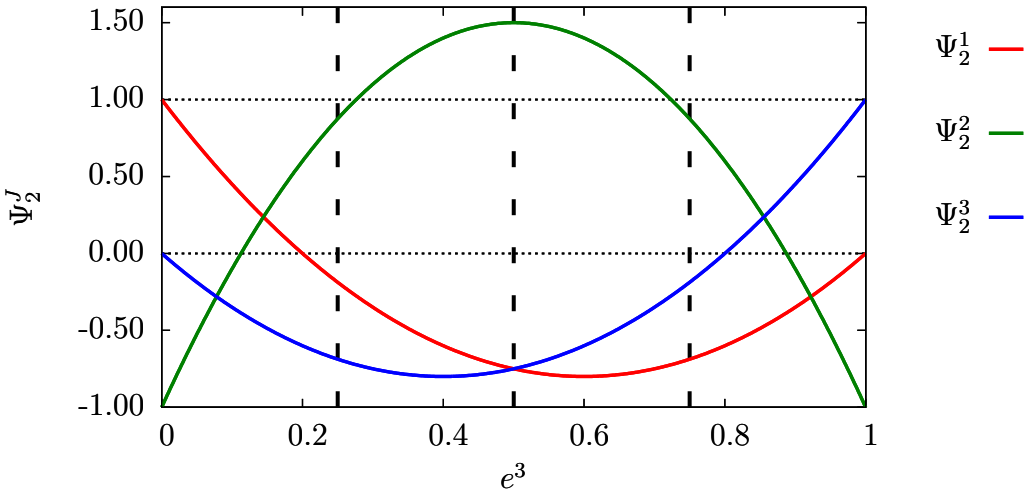

Figure 7: Plot of the Raviart-Thomas functions Ψ_2^J over the edge e^3 on a unit triangular domain

$$\hat{\boldsymbol{v}}_m^J(\xi_I, \eta_I) \cdot \hat{\boldsymbol{n}}^L \hat{l}^L = \begin{cases} 1, & \text{for } I = J \\ 0, & \text{for } I \neq J\,. \end{cases} \tag{59}$$

For the inner nodes

$$\hat{\boldsymbol{v}}_m^J \cdot \hat{\boldsymbol{q}}_{m-1}^I = \begin{cases} 1, & \text{for } I = J \\ 0, & \text{for } I \neq J \end{cases} \tag{60}$$

has to be evaluated. The vectorial functions $\hat{\boldsymbol{q}}_{m-1}^I$ can be chosen as given in Table 2, Table 10 and Table 13. This leads to J systems of equations which have to be solved in order to find the unknown coefficients. Entering in (45) yields the basis functions which now have to be Piola transformed, see Equation (51) and Equation (52).

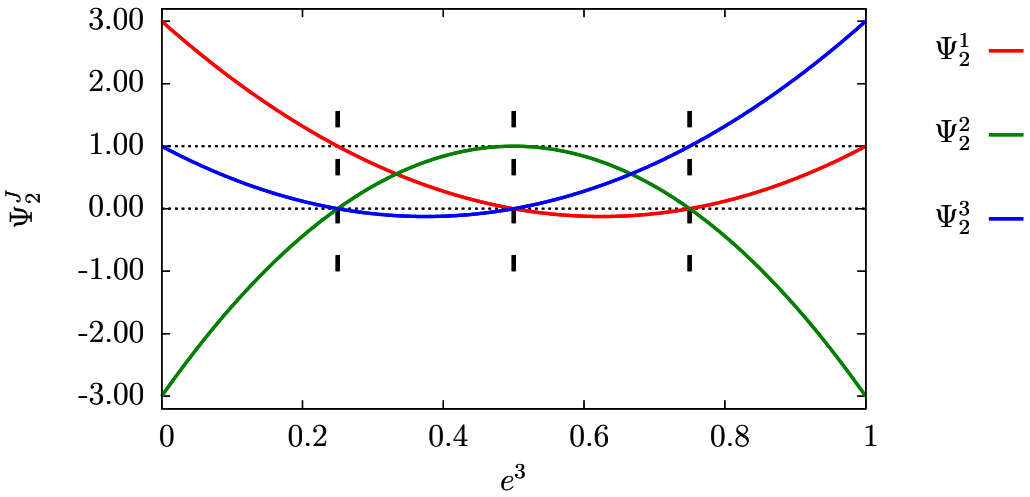

Figure 8: Plot of the alternative Raviart-Thomas functions Ψ_2^J over the edge e^3 on a unit triangular domain

Furthermore, they have to be normalized, see Equation (54), in order to obtain the vector-valued Raviart-Thomas interpolation functions Ψ_m^J as well as their divergence $\operatorname{div} \Psi_m^J$. Again, exemplary for edge e^3, the roots of the functions as well as the point, where the functions evaluate to be one can be seen, which is now at the nodal coordinates for this alternative basis functions, see also Figure 8. The coefficients for the vectorial basis functions for $m = 1$, $m = 2$ and $m = 3$ are given in a tabular form in the Appendix, see the chapters A.3, A.4 and A.5. In Figure 9 several vector-valued basis functions of RT_2 are plotted over the unit triangular domain. Here it becomes viewable, that the normals of the basis functions vanish at the edges, which are not associated with the interpolation site. For the inner nodes all normals to the edges of the basis functions vanish.

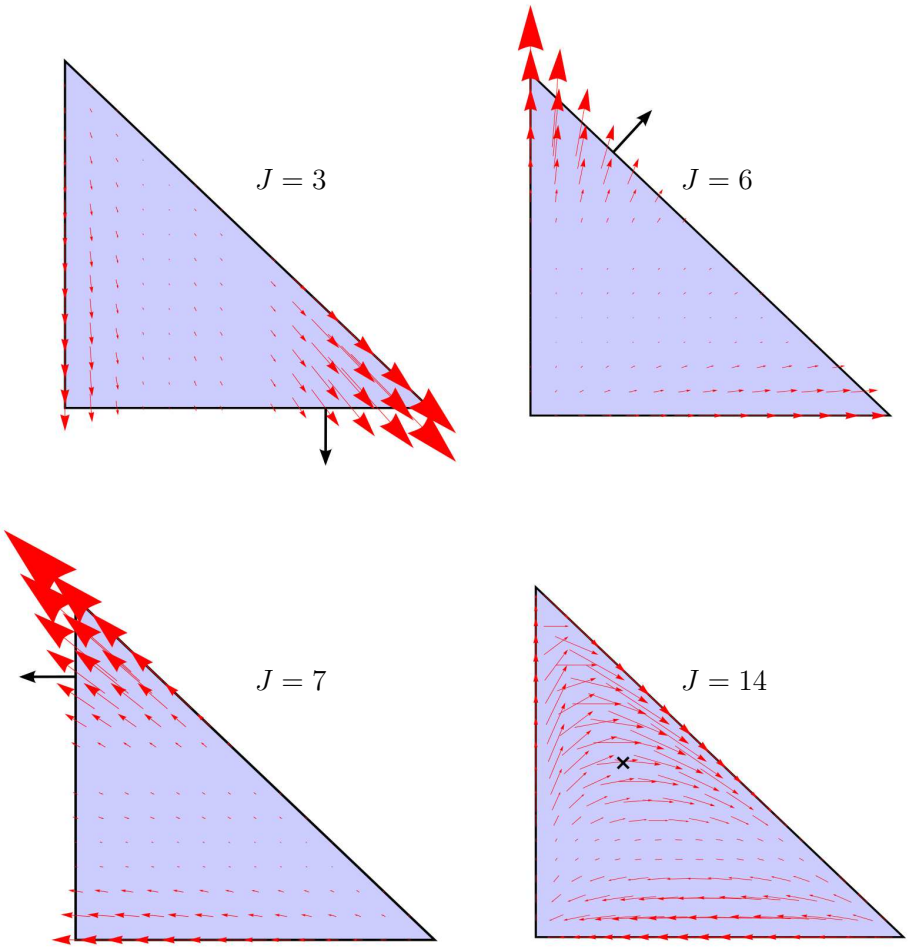

Figure 9: Plot of the basis functions $\hat{\boldsymbol{v}}_2^3, \hat{\boldsymbol{v}}_2^6, \hat{\boldsymbol{v}}_2^7$ and $\hat{\boldsymbol{v}}_2^{14}$.

4 The least-squares mixed finite element method

In this chapter the construction of least-squares functionals and the variations of a functional for finding the minimum are considered. Besides the general approach, a least-squares setup for hyperelastic materials described by free energy functions is provided. Furthermore, for a deeper understanding of the method, a one-dimensional introductory example is discussed, where all steps starting from the differential equation and the least-squares functional up to the solution of a simple boundary value are shown in detail. In addition to that, some remarks will be given concerning the boundary conditions and the implementation. Finally, all used element types will be presented. For the details on the standard tasks of the finite element method, as e.g. discretization, transformation, integration and assembly the reader is referred to state of the art FEM textbooks as e.g. Bathe [1995], Zienkiewicz and Taylor [2000], Wriggers [2001], Zhu et al. [2005] and Belytschko et al. [2000].

4.1 Construction of least-squares functionals

An advantage of the least-squares method is the flexibility to design suited functionals directly approximating the unknown field variables of interest. Hence, the first step is the construction of a functional containing the governing equations. In general there are different possibilities, e.g. different norms, in order to define a least-squares functional, see Bochev and Gunzburger [2009]. In this contribution a squared $L^2(\mathcal{B})$-norm is used for the construction, formally given by

$$||\boldsymbol{a}||^2_{L^2(\mathcal{B})} = \int_{\mathcal{B}} |\boldsymbol{a}|^2 \, \mathrm{d}V \,. \tag{61}$$

In order to define the minimization problem, the squared $L^2(\mathcal{B})$-norm is applied directly to a first-order system of i differential equations written in residual forms $\mathcal{R}_i = \mathbf{0}$, as

$$\mathcal{F}(\mathcal{U}) = \sum_i \frac{1}{2} ||\omega_i \mathcal{R}_i||^2_{L^2(\mathcal{B})} = \sum_i \int_{\mathcal{B}} \frac{1}{2} \omega_i^2 \, \mathcal{R}_i \bullet \mathcal{R}_i \; \mathrm{d}V \rightarrow \min \,, \tag{62}$$

with the weights ω_i and the vector of unknown fields $\mathcal{U}$. Here, the general scalar product of two quantities is denoted by "$\bullet$". In order to find the unknowns $\mathcal{U}_j$ which minimize the functional $\mathcal{F}(\mathcal{U})$, the variational calculus is used. Thus, the first variations with respect to the vector of unknown fields $\mathcal{U}$ have to vanish, i.e.

$$\delta_{\mathcal{U}_j} \mathcal{F} \;=\; \frac{\partial \mathcal{F}}{\partial \mathcal{U}_j} \delta \mathcal{U}_j \;=\; \sum_i \int_{\mathcal{B}} \omega_i^2 \, \delta_{\mathcal{U}_j} \mathcal{R}_i \bullet \mathcal{R}_i \, dV \;=\; 0 \,. \tag{63}$$

In case of linear elasticity, the discretized form of (63) directly yields a linear system of algebraic equations. In case of non-linearities, iterative procedures as for example a standard Newton scheme can be used in order to obtain the final solution. Therefore, the

second variation has to be provided as

$$\Delta_{\mathcal{U}_k}\delta_{\mathcal{U}_j}\mathcal{F} \;=\; \frac{\partial(\delta_{\mathcal{U}_j}\mathcal{F})}{\partial\mathcal{U}_k}\Delta\mathcal{U}_k \;=\; \sum_i \int_{\mathcal{B}} \omega_i^2(\Delta_{\mathcal{U}_k}\delta_{\mathcal{U}_j}\mathcal{R}_i \bullet \mathcal{R}_i + \delta_{\mathcal{U}_j}\mathcal{R}_i \bullet \Delta_{\mathcal{U}_k}\mathcal{R}_i)\, dV. \tag{64}$$

The general concept of finite element methods enables to solve differential equations on arbitrary domains. Therefore, the domain of consideration $\mathcal{B}$ has to be discretized into a finite number of polygonal elements $\mathcal{B}^e$. The approximated $\mathcal{B}^h$ domain is then given as the union of the finite element domains

$$\mathcal{B} \approx \mathcal{B}^h = \bigcup_{e=1}^{n_{ele}} \mathcal{B}^e\,, \tag{65}$$

with n_{ele} denoting the number of elements. The resulting functional (as well as the variations) are then given as the sum of the functional (variations) evaluated on each finite element,

$$\mathcal{F} = \sum_{e=1}^{n_{ele}} \mathcal{F}^e\,, \quad \delta\mathcal{F} = \sum_{e=1}^{n_{ele}} \delta\mathcal{F}^e \quad \text{and} \quad \Delta\delta\mathcal{F} = \sum_{e=1}^{n_{ele}} \Delta\delta\mathcal{F}^e\,, \tag{66}$$

with $\mathcal{F}^e$ ($\delta\mathcal{F}^e$, $\delta\Delta\mathcal{F}^e$) denoting the contribution of a typical element.

4.2 General setup for the hyperelastic least-squares formulation

For the development of a hyperelastic least-squares formulation, the general rules described in Chapter 4.1 are used. The formulation of consideration uses the displacements $\boldsymbol{u}$ and the first Piola-Kirchhoff stresses $\boldsymbol{P}$ as unknowns yielding the vector of unknown fields $\mathcal{U} = (\boldsymbol{u}, \boldsymbol{P})^T$. As a starting point for the construction of a least-squares functional for hyperelasticity the residuals

$$\begin{aligned}
\mathcal{R}_1 &= \operatorname{Div}\boldsymbol{P} + \boldsymbol{f} &&= \boldsymbol{0} \rightarrow \text{balance of momentum}\,,\\
\mathcal{R}_2 &= \boldsymbol{P} - \rho_0\partial_F\psi(\boldsymbol{C}) &&= \boldsymbol{0} \rightarrow \text{constitutive relation}\,,\\
\mathcal{R}_3 &= \boldsymbol{F}^{-1}\boldsymbol{P} - (\boldsymbol{F}^{-1}\boldsymbol{P})^T &&= \boldsymbol{0} \rightarrow \text{stress symmetry}
\end{aligned} \tag{67}$$

are defined, where $\boldsymbol{f}$ denotes the body force. From the mathematical point of view the third residual is redundant and could be neglected, which has been proven by Cai and Starke [2004] for the linear elastic case, since the constitutive relation with its associated residual takes care of the fulfillment of this property. However, from a practial point of view it seems to be advantageous to control the lack of symmetry of the stress quantity (associated to the balance of moment of momentum) directly, see e.g. Schwarz et al. [2014]. Following (62), a general least-squares functional for hyperelasticity with the solution quantities displacements and first Piola-Kirchhoff stress tensor for one element

is obtained as

$$\begin{aligned}\mathcal{F}^e(\boldsymbol{P},\boldsymbol{u}) &= \frac{1}{2}\int_{\mathcal{B}^e}\omega_1^2(\operatorname{Div}\boldsymbol{P}+\boldsymbol{f})\cdot(\operatorname{Div}\boldsymbol{P}+\boldsymbol{f})\,dV\\ &+ \frac{1}{2}\int_{\mathcal{B}^e}\omega_2^2(\boldsymbol{P}-\rho_0\partial_F\psi(\boldsymbol{C})):(\boldsymbol{P}-\rho_0\partial_F\psi(\boldsymbol{C}))\,dV\\ &+ \frac{1}{2}\int_{\mathcal{B}^e}\omega_3^2(\boldsymbol{F}^{-1}\boldsymbol{P}-(\boldsymbol{F}^{-1}\boldsymbol{P})^T):(\boldsymbol{F}^{-1}\boldsymbol{P}-(\boldsymbol{F}^{-1}\boldsymbol{P})^T)\,dV\,.\end{aligned} \tag{68}$$

For the minimization the first variations needs to be zero leading to

$$\begin{aligned}\delta_u\mathcal{F}^e &= \sum_{i=1}^{3}\int_{\mathcal{B}^e}\omega_i^2\delta_u\mathcal{R}_i\bullet\mathcal{R}_i\,dV=0\,,\\ \delta_P\mathcal{F}^e &= \sum_{i=1}^{3}\int_{\mathcal{B}^e}\omega_i^2\delta_P\mathcal{R}_i\bullet\mathcal{R}_i\,dV=0\,,\end{aligned} \tag{69}$$

with

$$\delta\boldsymbol{u}=0\text{ on }\partial\mathcal{B}_u\quad\text{and}\qquad\delta\boldsymbol{P}=0\text{ on }\partial\mathcal{B}_P\,. \tag{70}$$

The linearization for the application of a Newton scheme yields

$$\begin{aligned}\Delta_u\delta_u\mathcal{F}^e &= \sum_{i=1}^{3}\int_{\mathcal{B}^e}\omega_i^2(\Delta_u\delta_u\mathcal{R}_i\bullet\mathcal{R}_i+\delta_u\mathcal{R}_i\bullet\Delta_u\mathcal{R}_i)\,dV\,,\\ \Delta_P\delta_u\mathcal{F}^e &= \sum_{i=1}^{3}\int_{\mathcal{B}^e}\omega_i^2(\Delta_P\delta_u\mathcal{R}_i\bullet\mathcal{R}_i+\delta_u\mathcal{R}_i\bullet\Delta_P\mathcal{R}_i)\,dV\,,\\ \Delta_u\delta_P\mathcal{F}^e &= \sum_{i=1}^{3}\int_{\mathcal{B}^e}\omega_i^2(\Delta_u\delta_P\mathcal{R}_i\bullet\mathcal{R}_i+\delta_P\mathcal{R}_i\bullet\Delta_u\mathcal{R}_i)\,dV\,,\\ \Delta_P\delta_P\mathcal{F}^e &= \sum_{i=1}^{3}\int_{\mathcal{B}^e}\omega_i^2(\Delta_P\delta_P\mathcal{R}_i\bullet\mathcal{R}_i+\delta_P\mathcal{R}_i\bullet\Delta_P\mathcal{R}_i)\,dV\,.\end{aligned} \tag{71}$$

The non-trivial variations are given by

$$\begin{aligned}\delta_P\mathcal{R}_1 &= \operatorname{Div}\delta\boldsymbol{P},\\ \delta_u\mathcal{R}_2 &= -\rho_0\partial^2_{FF}\psi(\boldsymbol{C})\delta\boldsymbol{F},\quad\delta_P\mathcal{R}_2=\delta\boldsymbol{P},\\ \delta_u\mathcal{R}_3 &= \delta\boldsymbol{F}^{-1}\boldsymbol{P}-(\delta\boldsymbol{F}^{-1}\boldsymbol{P})^T,\\ \delta_P\mathcal{R}_3 &= \boldsymbol{F}^{-1}\delta\boldsymbol{P}-(\boldsymbol{F}^{-1}\delta\boldsymbol{P})^T\end{aligned} \tag{72}$$

and the associated linear increments appear as

$$\begin{aligned}\Delta_P\mathcal{R}_1 &= \operatorname{Div}\Delta\boldsymbol{P},\\ \Delta_u\mathcal{R}_2 &= -\rho_0\partial^2_{FF}\psi(\boldsymbol{C})\Delta\boldsymbol{F},\quad\Delta_P\mathcal{R}_2=\Delta\boldsymbol{P},\\ \Delta_u\mathcal{R}_3 &= \Delta\boldsymbol{F}^{-1}\boldsymbol{P}-(\Delta\boldsymbol{F}^{-1}\boldsymbol{P})^T,\\ \Delta_P\mathcal{R}_3 &= \boldsymbol{F}^{-1}\Delta\boldsymbol{P}-(\boldsymbol{F}^{-1}\Delta\boldsymbol{P})^T\,.\end{aligned} \tag{73}$$

The non-vanishing terms for the second variation are

$$\begin{aligned}
\Delta_u\delta_u\mathcal{R}_2 &= -\partial_F(\partial^2_{FF}\psi(\boldsymbol{C})\delta\boldsymbol{F})\Delta\boldsymbol{F},\\
\Delta_u\delta_u\mathcal{R}_3 &= \Delta\delta\boldsymbol{F}^{-1}\boldsymbol{P} - (\Delta\delta\boldsymbol{F}^{-1}\boldsymbol{P})^T,\\
\Delta_P\delta_u\mathcal{R}_3 &= \delta\boldsymbol{F}^{-1}\Delta\boldsymbol{P} - (\delta\boldsymbol{F}^{-1}\Delta\boldsymbol{P})^T,\\
\Delta_u\delta_P\mathcal{R}_3 &= \Delta\boldsymbol{F}^{-1}\delta\boldsymbol{P} - (\Delta\boldsymbol{F}^{-1}\delta\boldsymbol{P})^T\,.
\end{aligned} \tag{74}$$

4.3 Interpolation of field quantities

Both unknown fields have to be suitably interpolated. For convenience and generality in the following interpolation matrices are introduced. For details on the used interpolation spaces and the interpolation functions see Chapter 3 and for the resulting different element types see Chapter 4.5. First, the displacement vector $\boldsymbol{u}$, the related test function $\delta\boldsymbol{u}$ and the related increment $\Delta\boldsymbol{u}$ are introduced. It is obtained with the interpolation matrix $\boldsymbol{N}$

$$\boldsymbol{u} = \sum_I \boldsymbol{N}^I \overset{u}{\boldsymbol{d}}{}^I\,, \quad \delta\boldsymbol{u} = \sum_I \boldsymbol{N}^I \delta\overset{u}{\boldsymbol{d}}{}^I \quad \text{and} \quad \Delta\boldsymbol{u} = \sum_I \boldsymbol{N}^I \Delta\overset{u}{\boldsymbol{d}}{}^I\,, \tag{75}$$

with the nodal displacement vector $\overset{u}{\boldsymbol{d}}{}^I$ and the interpolation sites for the displacement denoted by I. The displacement gradient is then interpolated by

$$\nabla\boldsymbol{u} = \sum_I \bar{\boldsymbol{B}}^I \overset{u}{\boldsymbol{d}}{}^I\,, \quad \nabla\delta\boldsymbol{u} = \sum_I \bar{\boldsymbol{B}}^I \delta\overset{u}{\boldsymbol{d}}{}^I \quad \text{and} \quad \nabla\Delta\boldsymbol{u} = \sum_I \bar{\boldsymbol{B}}^I \Delta\overset{u}{\boldsymbol{d}}{}^I\,, \tag{76}$$

where $\bar{\boldsymbol{B}}$ contains the derivatives of the interpolation functions. The first Piola-Kirchhoff stress tensor is interpolated as

$$\boldsymbol{P} = \sum_J \boldsymbol{A}^J \overset{P}{\boldsymbol{d}}{}^J\,, \quad \delta\boldsymbol{P} = \sum_J \boldsymbol{A}^J \delta\overset{P}{\boldsymbol{d}}{}^J \quad \text{and} \quad \Delta\boldsymbol{P} = \sum_J \boldsymbol{A}^J \Delta\overset{P}{\boldsymbol{d}}{}^J\,, \tag{77}$$

with $\boldsymbol{A}$ denoting the suitable interpolation matrix for the interpolation of the stresses and $\overset{P}{\boldsymbol{d}}{}^J$ denoting the nodal degrees of freedom of the stresses at each stress interpolation site J. The divergence of the first Piola-Kirchhoff stress tensor is obtained by

$$\operatorname{Div}\boldsymbol{P} = \sum_J \boldsymbol{D}\boldsymbol{A}^J \overset{P}{\boldsymbol{d}}{}^J\,. \tag{78}$$

The detailed structure of the presented interpolation matrices is dependent on the element type used and is shown in Chapter 4.5.2. In the next subsection, for a deeper understanding of the method, an illustrative one-dimensional example for a mixed problem exploiting all steps in detail for the treatment of a boundary value problem with the LSFEM is provided.

4.4 Introductory example in 1D

For a deeper understanding of the method an easy application of the mixed least-squares finite element method in one dimension is taken under consideration. Here, for convenience, our notation for the used quantities is simplified to

$$\begin{array}{ccccc} \boldsymbol{P} & \xrightarrow{\text{1D}} & P_{11} & \longrightarrow & P \\ \text{Div}\,\boldsymbol{P} & \xrightarrow{\text{1D}} & P_{11,1} & \longrightarrow & P' \\ \boldsymbol{f} & \xrightarrow{\text{1D}} & f_1 & \longrightarrow & f \\ \boldsymbol{F} = \mathbf{I} + \nabla \boldsymbol{u} & \xrightarrow{\text{1D}} & F_{11} = \delta_{11} + u_{1,1} & \longrightarrow & F = 1 + u' \\ \boldsymbol{C} = \boldsymbol{F}^T \boldsymbol{F} & \xrightarrow{\text{1D}} & C_{11} = F_{11} F_{11} & \longrightarrow & C = F^2 \end{array} \tag{79}$$

In 1D, the derivative of the displacement u yields the strain u'. We start from the balance of linear momentum, an elliptic differential equation of second order (in u), given as

$$(P(u'))' + f = 0 \tag{80}$$

on a domain $\mathcal{B}$, where P is a function of the derivative of the displacements. For the suitable interpolation of u, $\mathcal{C}^1$ continuous functions have to be chosen, since second-order derivatives of u arise in the differential equation. In order to circumvent this and enabling the use of $\mathcal{C}^0$ continuous interpolation functions, the differential equation of second order is transformed into a system of differential equations of first order. Therefore, the stresses are introduced as an additional unknown field and a further residual equation describing the relation between stresses and strains is added. This relation is given by the constitutive law. Here, P is given as the derivative of a function

$$\psi = (\frac{\lambda}{4} + \frac{\mu}{2})\,(F^2 - 1) - (\frac{\lambda}{2} + \mu)\ln(F)\,, \tag{81}$$

which is comparable to the free energy presented in Section 2.3.1, Equation (28.1) under the assumption of no transversal contraction (Poisson's ratio $\nu = 0$) leading to a material parameter $\lambda = 0$. Nevertheless, λ is maintained in the derivation for the sake of completeness. Differentiating (81) with respect to F yields the (first Piola-Kirchhoff) stresses

$$P = \partial_F \psi = (\frac{\lambda}{2} + \mu)(F - \frac{1}{F})\,. \tag{82}$$

The nonlinear material behavior is depicted as a "stress-strain"- curve (chosing $\lambda = 0, \mu = 1$), see Figure 10. The first-order system in residual form is obtained as

$$\mathcal{R}_1 = P' + f = 0 \quad \text{and} \quad \mathcal{R}_2 = P - (\frac{\lambda}{2} + \mu)(F - \frac{1}{F}) = 0 \tag{83}$$

with the boundary conditions

$$u = g \quad \text{on } \partial\mathcal{B}_u \subseteq \partial\mathcal{B} \quad \text{and} \quad P = h \quad \text{on } \partial\mathcal{B}_P \subseteq \partial\mathcal{B} \tag{84}$$

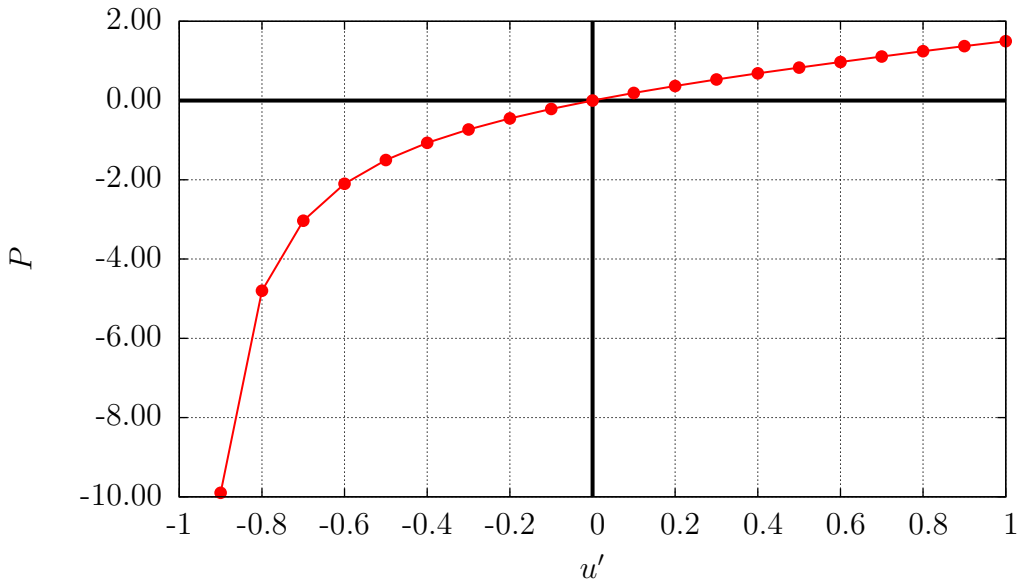

Figure 10: Stress-strain- curve ($\lambda = 0, \mu = 1$), 1D.

and the decomposition

$$\partial\mathcal{B} = \partial\mathcal{B}_u \cup \partial\mathcal{B}_P \ \wedge \ \partial\mathcal{B}_u \cap \partial\mathcal{B}_P = \emptyset \,. \tag{85}$$

Applying a squared $L^2(\mathcal{B})$-norm and a weighting for the residuals leads to the least-squares functional

$$\begin{aligned} \mathcal{F} &= \frac{1}{2}||\omega_1\mathcal{R}_1||^2_{L^2(\mathcal{B})} + \frac{1}{2}||\omega_2\mathcal{R}_2||^2_{L^2(\mathcal{B})} \\ &= \frac{1}{2}\int_{\mathcal{B}} \omega_1^2\mathcal{R}_1^2 \,\mathrm{d}X + \frac{1}{2}\int_{\mathcal{B}} \omega_2^2\mathcal{R}_2^2 \,\mathrm{d}X \quad \rightarrow \quad \min\,, \end{aligned} \tag{86}$$

which has to be minimized. Thus, the first variations $\delta_u\mathcal{F}$ and $\delta_P\mathcal{F}$ with respect to the solution variables (u, P) have to be zero. With $\delta F = \delta u'$ Equation (63) yields

$$\begin{aligned} \delta_u\mathcal{F} &= \omega_2^2 \int_{\mathcal{B}} \delta_u\mathcal{R}_2 \ \mathcal{R}_2 \,\mathrm{d}X = 0\,, \\ \delta_P\mathcal{F} &= \omega_1^2 \int_{\mathcal{B}} \delta_P\mathcal{R}_1 \ \mathcal{R}_1 \,\mathrm{d}X + \omega_2^2 \int_{\mathcal{B}} \delta_P\mathcal{R}_2 \ \mathcal{R}_2 \,\mathrm{d}X = 0\,, \end{aligned} \tag{87}$$

with

$$\delta_u\mathcal{R}_2 = -\delta F \left(\frac{\lambda}{2} + \mu\right)\left(1 + \frac{1}{F^2}\right), \quad \delta_P\mathcal{R}_1 = \delta P' \quad \text{and} \quad \delta_P\mathcal{R}_2 = \delta P \tag{88}$$

and the conditions

$$\delta u = 0 \text{ on } \partial\mathcal{B}_u \quad \text{and} \quad \delta P = 0 \text{ on } \partial\mathcal{B}_P\,. \tag{89}$$

Since (87) is nonlinear (the terms $\mathcal{R}_2$ and $\delta_u\mathcal{R}_2$ are broken rational in u'), a Newton scheme is applied to find the root. Therefore, the non-zero second variations of (64) are given as

$$\begin{aligned}
\Delta_u\delta_u\mathcal{F} &= \omega_2^2 \int_{\mathcal{B}} \Delta_u\delta_u\mathcal{R}_2\ \mathcal{R}_2 + \delta_u\mathcal{R}_2\ \Delta_u\mathcal{R}_2\ \mathrm{d}X\,,\\
\Delta_P\delta_u\mathcal{F} &= \omega_2^2 \int_{\mathcal{B}} \delta_u\mathcal{R}_2\ \Delta_P\mathcal{R}_2\ \mathrm{d}X\,,\\
\Delta_u\delta_P\mathcal{F} &= \omega_2^2 \int_{\mathcal{B}} \delta_P\mathcal{R}_2\ \Delta_u\mathcal{R}_2\ \mathrm{d}X\,,\\
\Delta_P\delta_P\mathcal{F} &= \omega_1^2 \int_{\mathcal{B}} \delta_P\mathcal{R}_1\ \Delta_P\mathcal{R}_1\ \mathrm{d}X + \omega_2^2 \int_{\mathcal{B}} \delta_P\mathcal{R}_2\ \Delta_P\mathcal{R}_2\ \mathrm{d}X\,,
\end{aligned} \tag{90}$$

with the terms

$$\begin{gathered}
\Delta_u\delta_u\mathcal{R}_2 = \delta F\left(\frac{\lambda}{2}+\mu\right)\frac{2}{F^3}\Delta F\,,\quad \Delta_u\mathcal{R}_2 = -\left(\frac{\lambda}{2}+\mu\right)\left(1+\frac{1}{F^2}\right)\Delta F\,,\\
\Delta_P\mathcal{R}_1 = \Delta P' \quad\text{and}\quad \Delta_P\mathcal{R}_2 = \Delta P\,,
\end{gathered} \tag{91}$$

with $\Delta F = \Delta u'$. For the discretization mixed finite elements are used consisting of a combination of a quadratic three-noded element (for u) and a linear two-noded element (for P) with one degree of freedom at each node. This leads to a reference element in the parameter space (ξ) with three nodes. Here, the first two nodes have two degrees of freedom and the midnode has one degree of freedom, see Figure 11.

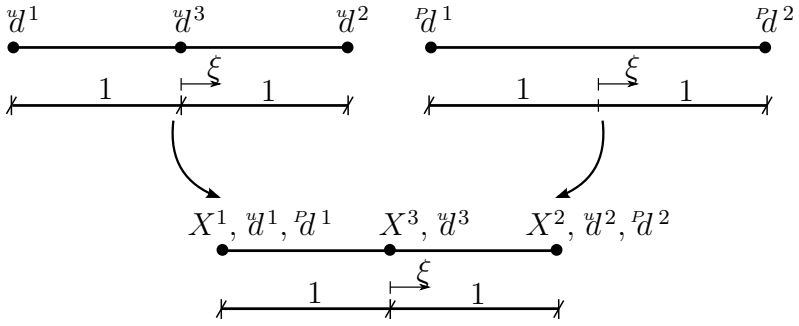

Figure 11: Mixed reference element (Ω^e) in 1D.

The vectors of the nodal degrees of freedom for u, P and the geometry X are given as

$$\overset{u}{\boldsymbol{d}} = [{}^{u}d^1, {}^{u}d^2, {}^{u}d^3]^T,\quad \overset{P}{\boldsymbol{d}} = [{}^{P}d^1, {}^{P}d^2]^T \quad\text{and}\quad \boldsymbol{X} = [X^1, X^2, X^3]^T\,. \tag{92}$$

For the approximation of the unknown field u and the geometry X quadratic polynomial interpolation on the reference element $\Omega^e = [-1, 1]$ is used with the shape functions summarized in a vector $\boldsymbol{N}_u$,

$$\boldsymbol{N}_u(\xi) = [N_u^1,\, N_u^2,\, N_u^3] = \left[\frac{1}{2}(\xi^2 - \xi),\, \frac{1}{2}(\xi^2 + \xi),\, 1 - \xi^2\right] \tag{93}$$

and the corresponding vector $\boldsymbol{B}_u(\xi) = \partial_X \boldsymbol{N}_u(\xi)$ containing the derivatives of the shape functions with respect to X

$$\boldsymbol{B}_u(\xi) = [B_u^1,\, B_u^2,\, B_u^3] = \frac{2}{l^e}\left[\xi - \frac{1}{2},\, \xi + \frac{1}{2},\, -2\xi\right] . \tag{94}$$

Here, the derivatives of the shape functions are derived by the chain rule

$$\frac{\partial N}{\partial X} = \frac{\partial N}{\partial \xi}\frac{\partial \xi}{\partial X} = \frac{\partial N}{\partial \xi} J_{11}^{-1} \tag{95}$$

with the transformation J_{11}. With $\boldsymbol{X} = (0, l^e, l^e/2)^T$

$$J_{11} = \frac{\partial X}{\partial \xi} = \sum_{I=1}^{3} N_{u,\xi}^I X^I = (\xi - \frac{1}{2})0 + (\xi + \frac{1}{2})l^e - (2\xi)\frac{l^e}{2} = \frac{l^e}{2} \tag{96}$$

is obtained. With the element nodes $I = 1, 2, 3$ the interpolation of u' and the variations δF, ΔF are given by

$$u'(\xi) = \boldsymbol{B}_u(\xi)\, \overset{u}{\boldsymbol{d}}, \quad \delta F(\xi) = \delta u'(\xi) = \boldsymbol{B}_u(\xi) \delta \overset{u}{\boldsymbol{d}}, \quad \Delta F(\xi) = \Delta u'(\xi) = \boldsymbol{B}_u(\xi) \Delta \overset{u}{\boldsymbol{d}} \tag{97}$$

and the geometry approximation is

$$X(\xi) = \boldsymbol{N}_u(\xi)\boldsymbol{x} \,. \tag{98}$$

For the approximation of P polynomial interpolation of order one on the reference element domain $\Omega^e = [-1, 1]$ is chosen. The choice of a linear approach for P is reasonable. This is based on the quadratic interpolation of u, the resulting interpolation order of u' and its relation to P. Here, the free choice of the interpolation orders for the unknowns is possible due to the fact, that least-squares mixed finite elements are not restricted to the LBB-condition, unlike e.g. mixed Galerkin elements compare for instance Jiang [1998], Bochev and Gunzburger [2009] and Braess [1997]. The vector of the shape functions of first order $\boldsymbol{N}_P$ appears as

$$\boldsymbol{N}_P(\xi) = [N_P^1,\, N_P^2] = \left[\frac{1}{2}(1 - \xi), \frac{1}{2}(1 + \xi)\right] . \tag{99}$$

The vector of the derivatives of the shape functions $\boldsymbol{B}_P(\xi) = \partial_X \boldsymbol{N}_P(\xi)$ has the form

$$\boldsymbol{B}_P(\xi) = [B_P^1, B_P^2] = \frac{2}{l^e}\left[-\frac{1}{2},\, \frac{1}{2}\right] . \tag{100}$$

With the interpolation of P, P' and their variations δP and $\delta P'$, the matrix expressions are obtained as

$$\begin{aligned} P(\xi) &= \sum_{J=1}^{2} N_P^J \overset{P}{d}{}^J = \boldsymbol{N}_P \overset{P}{\boldsymbol{d}} \;, \quad \delta P(\xi) = \sum_{J=1}^{2} N_P^J \, \delta \overset{P}{d}{}^J = \boldsymbol{N}_P \, \delta \overset{P}{\boldsymbol{d}} \;, \\ P'(\xi) &= \sum_{J=1}^{2} B_P^J \overset{P}{d}{}^J = \boldsymbol{B}_P \overset{P}{\boldsymbol{d}} \;, \quad \delta P'(\xi) = \sum_{J=1}^{2} B_P^J \, \delta \overset{P}{d}{}^J = \boldsymbol{B}_P \, \delta \overset{P}{\boldsymbol{d}} \end{aligned} \tag{101}$$

The domain is discretized with n_{ele} finite elements, i.e. $\mathcal{B} = \mathcal{B}^h = \bigcup_{e=1}^{n_{ele}} \mathcal{B}^e$. The first and the second variation follow as

$$\begin{aligned} \delta\mathcal{F} &= \delta_u\mathcal{F} + \delta_P\mathcal{F} = \sum_e \delta\mathcal{F}^e \quad \text{and} \\ \Delta\delta\mathcal{F} &= \Delta_u\delta_u\mathcal{F} + \Delta_u\delta_P\mathcal{F} + \Delta_P\delta_u\mathcal{F} + \Delta_P\delta_P\mathcal{F} = \sum_e \Delta\delta\mathcal{F}^e \end{aligned} \tag{102}$$

with the contributions of a typical element

$$\delta\mathcal{F}^e = \delta \overset{u}{\boldsymbol{d}}{}^T \underbrace{\int_{\mathcal{B}^e} -\boldsymbol{B}_u^T \omega_2^2 \left(\frac{\lambda}{2} + \mu\right) (1 + \frac{1}{F^2}) \, \mathcal{R}_2 \, \mathrm{d}x}_{\boldsymbol{r}_u^e} + \delta \overset{P}{\boldsymbol{d}}{}^T \underbrace{\int_{\mathcal{B}^e} \boldsymbol{B}_P^T \, \omega_1^2 \, \mathcal{R}_1 + \boldsymbol{N}_P^T \, \omega_2^2 \, \mathcal{R}_2 \, \mathrm{d}x}_{\boldsymbol{r}_P^e} \tag{103}$$

and

$$\begin{aligned} \Delta\delta\mathcal{F}^e = {} & \delta \overset{u}{\boldsymbol{d}}{}^T \underbrace{\int_{\mathcal{B}^e} \boldsymbol{B}_u^T \left[\omega_2^2 \left(\frac{\lambda}{2} + \mu\right) \frac{2}{F^3} \mathcal{R}_2 + \omega_2^2 \left(\left(\frac{\lambda}{2} + \mu\right) (1 + \frac{1}{F^2}) \right)^2 \right] \boldsymbol{B}_u \, \mathrm{d}x}_{\boldsymbol{K}_{uu}^e} \, \Delta \overset{u}{\boldsymbol{d}} \\ & - \delta \overset{u}{\boldsymbol{d}}{}^T \underbrace{\int_{\mathcal{B}^e} \boldsymbol{B}_u^T \left[\omega_2^2 \left(\left(\frac{\lambda}{2} + \mu\right) (1 + \frac{1}{F^2}) \right) \right] \boldsymbol{N}_P \, \mathrm{d}x}_{\boldsymbol{K}_{uP}^e} \, \Delta \overset{P}{\boldsymbol{d}} \\ & - \delta \overset{P}{\boldsymbol{d}}{}^T \underbrace{\int_{\mathcal{B}^e} \boldsymbol{N}_P^T \left[\omega_2^2 \left(\left(\frac{\lambda}{2} + \mu\right) (1 + \frac{1}{F^2}) \right) \right] \boldsymbol{B}_u \, \mathrm{d}x}_{\boldsymbol{K}_{Pu}^e} \, \Delta \overset{u}{\boldsymbol{d}} \\ & + \delta \overset{P}{\boldsymbol{d}}{}^T \underbrace{\int_{\mathcal{B}^e} \boldsymbol{B}_P^T \, \omega_1^2 \, \boldsymbol{B}_P + \boldsymbol{N}_P^T \, \omega_2^2 \, \boldsymbol{N}_P \, \mathrm{d}x}_{\boldsymbol{K}_{PP}^e} \, \Delta \overset{P}{\boldsymbol{d}} \;. \end{aligned} \tag{104}$$

Here, $\boldsymbol{K}^e_{uu}, \boldsymbol{K}^e_{uP}, \boldsymbol{K}^e_{Pu}, \boldsymbol{K}^e_{PP}$ denote the submatrices of the element stiffness matrix $\boldsymbol{K}^e$ and $\boldsymbol{r}^e_u$ and $\boldsymbol{r}^e_P$ denotes the entries of the element right-hand-side vector $\boldsymbol{r}^e$. This leads to the system of equations for one element of the form

$$\underbrace{\begin{bmatrix} \boldsymbol{K}^e_{uu} & \boldsymbol{K}^e_{uP} \\ \boldsymbol{K}^e_{Pu} & \boldsymbol{K}^e_{PP} \end{bmatrix}}_{\boldsymbol{K}^e} \underbrace{\begin{bmatrix} \Delta\, {}^{u}\boldsymbol{d}^e \\ \Delta\, {}^{P}\boldsymbol{d}^e \end{bmatrix}}_{\Delta\boldsymbol{d}^e} = - \underbrace{\begin{bmatrix} \boldsymbol{r}^e_u \\ \boldsymbol{r}^e_P \end{bmatrix}}_{\boldsymbol{r}^e}, \tag{105}$$

with the element vector of the increments of the degrees of freedom $\Delta\boldsymbol{d}^e = [\,\Delta\, {}^{u}\boldsymbol{d}^e,\, \Delta\, {}^{P}\boldsymbol{d}^e]^T$. The transformation of the integral from the physical space (here $\mathrm{d}x$) to the reference domain $\Omega^e = [-1, 1]$ (here $\mathrm{d}\xi$) is based on

$$\int_{\mathcal{B}^e} \mathrm{d}x = \int_{\Omega^e} J_{11}\, \mathrm{d}\xi\,, \tag{106}$$

where the Jacobian J_{11} given in (96). The evaluation of the integral expressions can be done analytically or, as mostly used in the field of finite element formulations by numerical integration schemes as, for instance, Gaussian quadrature, see e.g. Wriggers [2001]. Transformation and evaluation of the integral leads to a nonlinear system of equations which can be solved using a Newton scheme.
As a simple example, a one-dimensional boundary value problem with essential displacement boundary conditions on both sides ($u(0) = u(l) = 0$) and a bodyforce $f = 2$ is considered, compare Figure 12. The domain is discretized by one element with an el-

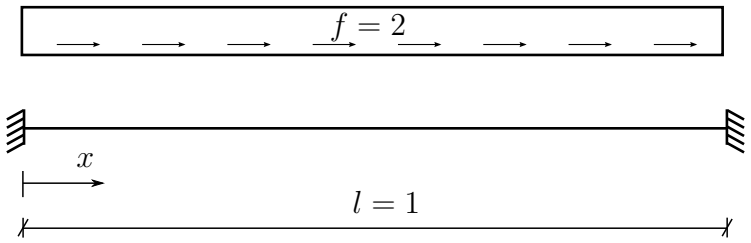

Figure 12: Setup boundary value problem in 1D.

ement length of $l^e = l = 1$. The material parameters are chosen as $\lambda = \mu = 1$ and the weights as $\omega_1 = \omega_2 = 1$. Due to the essential boundary conditions for the displacements, ${}^{u}d^1 = {}^{u}d^2 = 0$. The initial values for the Newton iteration are given as zero for all remaining nodal degrees of freedom

$$\boldsymbol{d}_{\mathrm{red},0} = [\,{}^{u}d^3_0,\, {}^{p}d^1_0,\, {}^{p}d^2_0]^T = \boldsymbol{0} \tag{107}$$

and will be updated as

$$\boldsymbol{d}_{\mathrm{red},n+1} = \boldsymbol{d}_{\mathrm{red},n} + \Delta\boldsymbol{d}_{\mathrm{red}} \tag{108}$$

after each Newton step. Since only one element is considered, no assembly procedure is necessary. The resulting reduced system of equations (due to the boundary conditions and (89)) reads

$$\underbrace{\left[\begin{pmatrix} 48 & -2 & 2 \\ -2 & \frac{4}{3} & -\frac{5}{6} \\ 2 & -\frac{5}{6} & \frac{4}{3} \end{pmatrix}\right]}_{\boldsymbol{K}_{\mathrm{red}}} \underbrace{\begin{bmatrix} \Delta\, {}^{u}\!d^{3} \\ \Delta\, {}^{p_1}\!d^{1} \\ \Delta\, {}^{p_1}\!d^{2} \end{bmatrix}}_{\Delta\boldsymbol{d}_{\mathrm{red}}} = - \underbrace{\begin{bmatrix} 0 \\ -2 \\ 2 \end{bmatrix}}_{\boldsymbol{r}_{\mathrm{red}}}, \tag{109}$$

with the reduced stiffness matrix $\boldsymbol{K}_{\mathrm{red}}$, the increments of the reduced vector of degrees of freedom $\Delta\boldsymbol{d}_{\mathrm{red}}$ and the reduced right-hand-side vector $\boldsymbol{r}_{\mathrm{red}}$. The increments of the degrees of freedom as well as the updated ones for each Newton iteration (NI) are obtained as

NI	$\Delta\boldsymbol{d}_{\mathrm{red}}$	$\boldsymbol{d}_{\mathrm{red}}$
0	$[0, 0, 0]^T$	$[0, 0, 0]^T$
1	$[0.0833333, 1., -1.]^T$	$[0.0833333, 1., -1.]^T$
2	$[-0.00147549, -0.055534, -0.0556075]^T$	$[0.0818578, 0.944466, -1.05561]^T$
3	$[-39.1677, -3.15172, 70.2618]^T \times 10^{-6}$	$[0.0818187, 0.944463, -1.05554]^T$
4	$[-3.56342, -12.5686, -7.70844]^T \times 10^{-9}$	$[0.0818187, 0.944463, -1.05554]^T$

(110)

and the residual norms $|\boldsymbol{r}_{\mathrm{red}}|$ at the end of each Newton iteration yields

NI	$\lvert\boldsymbol{r}_{\mathrm{red}}\rvert$
0	2.82843
1	0.169474
2	0.0019758
3	2.02438×10^{-7}
4	2.23428×10^{-15}

(111)

The solution of the Newton iteration yields $\boldsymbol{d}_{\mathrm{red}} = [0.0818187, 0.944463, -1.05554]^T$. For comparison the differential equation of second order

$$\left(\frac{\lambda}{2} + \mu\right)\left(u''(X) + \frac{u''(X)}{1 + u'(X)^2}\right) + 2 = 0 \tag{112}$$

resulting from (80) with (79) and (81) on the domain $X = [0, 1]$ with the boundary conditions u(0)=u(1)=0 is solved using the command NDSolve of *Mathematica* (where "Explicit Euler" is chosen as the method). This leads to the result $u(0.5) = 0.0818432$, $u'(0) = 0.363335 \rightarrow P(0) = 0.94476$ and $u'(1) = -0.291704 \rightarrow P(1) = -1.05532$. Furthermore, the result for a discretization with ten least-squares elements compared to the numerical solution of *Mathematica* is shown in Figure 13. It can be concluded, that the provided least-squares mixed finite element formulation is able to solve the given differential equation of second order in an appropriate way.

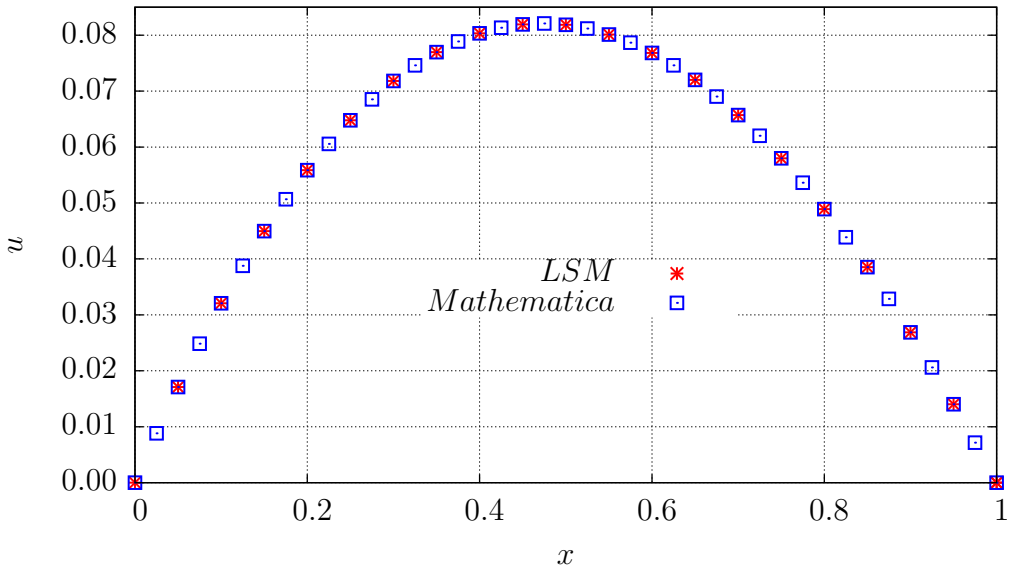

Figure 13: Solution for the displacements u, *Mathematica* vs LSM, 1D.

4.5 Different least-squares element types under investigation

Considering solid materials, the displacement field is, under some technical assumptions (e.g. no cracks), in general continuous. Hence, an approximation in the space $W^{1,p}(\mathcal{B})$ is a suitable choice, as it ensures continuity of the overall interpolated field from element to element. Therefore, standard interpolation polynomials are chosen for the approximation of the displacements. The solution for the stresses can naturally be found in the Sobolev space $W^q(\mathrm{div}, \mathcal{B})$. This is due to the fact, that stresses are normal continuous, see also Figure 2. That means, that the normal entries of the stresses, which can be denoted by the so-called traction vector ($\boldsymbol{t} = \boldsymbol{\sigma n}$, $\boldsymbol{T} = \boldsymbol{PN}$) are continuous. Therefore, the choice of vector-valued Raviart-Thomas functions for the interpolation of the stresses are a suitable choice, due to their ability to ensure a conforming discretization in $W^q(\mathrm{div}, \mathcal{B})$. We obtain the approximations as $\left\{\boldsymbol{u} \in W^{1,p}(\mathcal{B})^d : \boldsymbol{u}|_{\mathcal{B}_e} \in P_k(\mathcal{B}_e)^d; \forall\, \mathcal{B}_e\right\}$ and $\left\{\boldsymbol{P} \in W^q(\mathrm{div}, \mathcal{B})^d : \boldsymbol{P}|_{\mathcal{B}_e} \in RT_m(\mathcal{B}_e)^d \,\forall\, \mathcal{B}_e\right\}$, with d denoting the dimension. These resulting elements of type RT_mP_k where m denotes the polynomial order of the stress interpolation and k the polynomial order of the standard interpolation polynomials for the interpolation of the displacements has primarily been developed by Cai and Starke [2003]. An alternative way might be the interpolation of the stresses in $W^{1,p}(\mathcal{B})$. Unfortunately, due to the fact that the $W^{1,p}(\mathcal{B})$ space is more restricted (all entries are continuous) than the $W^q(\mathrm{div}, \mathcal{B})$ space (just the normal entries have to be continuous), maybe a so-

lution cannot (at least locally) be found, as $W^{1,p}(\mathcal{B})$ is a subspace of $W^q(\mathrm{div}, \mathcal{B})$, see also Equation (113).

$$\begin{array}{ccccc} (P_k(\mathcal{B}))^d & \subseteq & RT_k(\mathcal{B}) & \subseteq & (dP_{k+1}(\mathcal{B}))^d \\ \cap\mathrel{|} & & \cap\mathrel{|} & & \cap\mathrel{|} \\ (W^{1,p}(\mathcal{B}))^d & \subseteq & W^q(\mathrm{div}, \mathcal{B}) & \subseteq & (L^2(\mathcal{B}))^d \end{array} \tag{113}$$

But, because of the treatment of all restrictions in a least-squares sense, the arising error might be negligible small especially for fine meshes. The approximation is given by $\left\{\boldsymbol{u} \in W^{1,p}(\mathcal{B})^d : \boldsymbol{u}|_{\mathcal{B}_e} \in P_k(\mathcal{B}_e)^d; \forall\, \mathcal{B}_e\right\}$ and $\left\{\boldsymbol{P} \in W^{1,p}(\mathcal{B})^d : \boldsymbol{P}|_{\mathcal{B}_e} \in P_k(\mathcal{B}_e)^d \;\forall\, \mathcal{B}_e\right\}$. This element type is denoted by P_mP_k, where m and k indicate the interpolation order for the stresses and the displacements. Investigations in this field for a linear elastic material has been done by Steeger et al. [2015]. Here, the authors mainly considered the performance of several interpolation combinations with respect to a tip displacement. In the following the two-dimensional element types used in the framework of this thesis are presented. Therefore, the approximations using RT and P are considered seperately. The interpolations are limitted to the orders $1, 2, 3$ and 4 for P and for RT to the orders $0, 1, 2$ and 3.

4.5.1 Position of the interpolation sites and number of element degrees of freedom In Figure 14 the resulting elements for an interpolation using vector-valued Raviart-Thomas interpolation functions, compare Section 3.3, are presented.

Here, the interpolation sites are denoted by arrows respectively crosses. The elements for the interpolation with standard interpolation polynomials are depicted in Figure 15, compare also Chapter 3.2, where the interpolation sites are denoted by bullets. Combining the interpolation of the displacements and the stresses yields the latter mentioned element types RT_mP_k respectively P_mP_k. In Table 4 the different element types with the resulting number of nodes per element (nen) and the element degrees of freedom (edof) are shown in the form (nen,edof).

It becomes clear that the P_mP_k elements have a higher number of degrees of freedom per element. This is due to the interpolation of the stresses in $W^{1,p}(\mathcal{B})$, as all entries of the stress tensor are degrees of freedom, whereas for RT_mP_k only the entries of the local traction vector are used as degrees of freedom. In Chapter 5.1 the performance of the different element types, with respect to the displacement approximation, under consideration of a bending dominated boundary value problem is investigated. Since the difference between the two element types is the interpolation space for the stresses, in Chapter 5.4 the effect of different interpolation spaces for the stresses is considered. Therefore the stress distribution over a quartered plate consisting of four different materials is computed and investigated, especially at the material interfaces.

4.5.2 Resulting interpolation matrices The general interpolation of the unknown field quantities is shown in Chapter 4.3. Therefore, several interpolation matrices have been introduced. The detailed structure of these matrices in dependence of the element

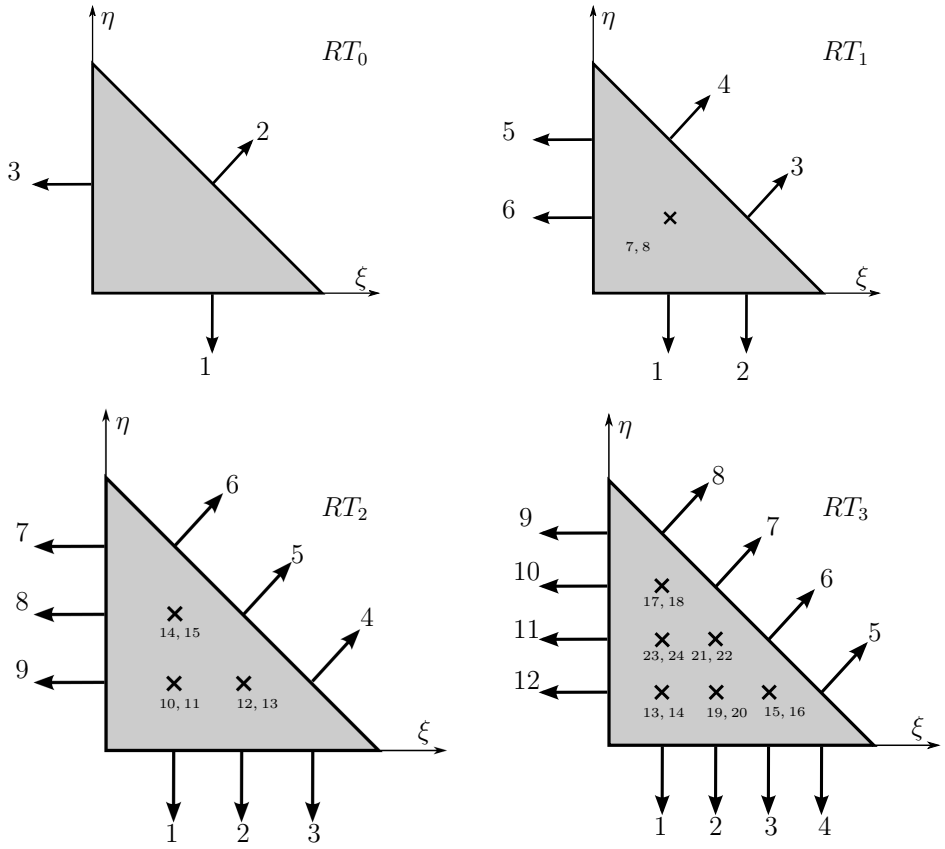

Figure 14: Arrangement of element nodes J for RT.

(nen,edof)	$P_1\,(3,6)$	$P_2\,(6,12)$	$P_3\,(10,20)$	$P_4\,(15,30)$
$P_1\,(3,12)$	$(6,18)$	$(9,24)$	$(13,32)$	$(18,42)$
$P_2\,(6,24)$	$(9,30)$	$(12,36)$	$(16,44)$	$(21,54)$
$P_3\,(10,40)$	$(13,46)$	$(16,52)$	$(20,60)$	$(25,70)$
$P_4\,(15,60)$	$(18,66)$	$(21,72)$	$(25,80)$	$(30,90)$
$RT_0\,(3,6)$	$(6,12)$	$(9,18)$	$(13,26)$	$(18,36)$
$RT_1\,(8,16)$	$(11,22)$	$(14,28)$	$(18,36)$	$(23,46)$
$RT_2\,(15,30)$	$(18,36)$	$(21,42)$	$(25,50)$	$(30,60)$
$RT_3\,(24,48)$	$(27,54)$	$(30,60)$	$(34,68)$	$(39,78)$

Table 4: Number of element nodes (nen) and number of degrees of freedom per element (edof) for the different two-dimensional element types under consideration.

type is shown in the following under consideration of the quantity itself, as the variation and the increment are analoguously. For all vectorial quantities the structure is maintained, whereas all tensorial quantities are restored as vectors. The matrices are given for the three-dimensional case but can be easily reduced to the two-dimensional case.

For the interpolation of the displacement field in Equation (75) the matrix $\boldsymbol{N}$ (respectively $\bar{\boldsymbol{B}}$ for the gradient) is introduced. As both element types use standard interpolation

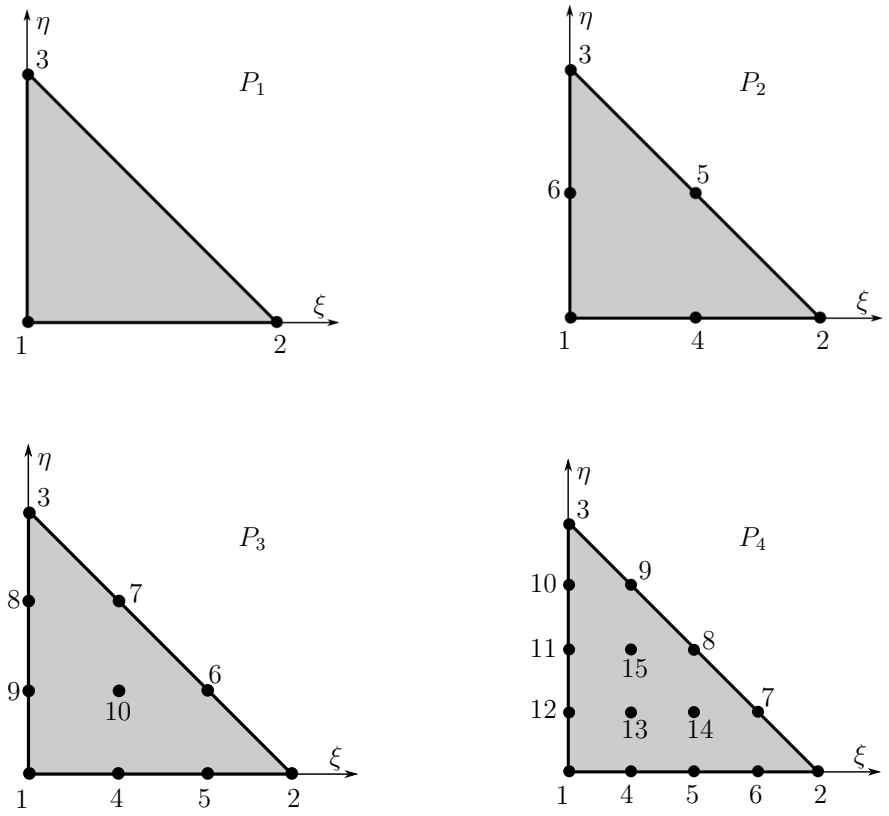

Figure 15: Arrangement of element nodes I for P.

polynomials for the interpolation of the displacement field (and its gradient) the matrices are obtained as

$$\boldsymbol{u} = \begin{bmatrix} u_1 \\ u_2 \\ u_3 \end{bmatrix} = \sum_I \boldsymbol{N}^I \, {}^u\boldsymbol{d}^I = \sum_I \begin{bmatrix} N^I & 0 & 0 \\ 0 & N^I & 0 \\ 0 & 0 & N^I \end{bmatrix} \begin{bmatrix} {}^u d_1^I \\ {}^u d_2^I \\ {}^u d_3^I \end{bmatrix}, \tag{114}$$

$$\nabla\boldsymbol{u} = \begin{bmatrix} u_{1,1} \\ u_{1,2} \\ u_{1,3} \\ u_{2,1} \\ u_{2,2} \\ u_{2,3} \\ u_{3,1} \\ u_{3,2} \\ u_{3,3} \end{bmatrix} = \sum_I \bar{\boldsymbol{B}}^I \, {}^u\boldsymbol{d}^I = \sum_I \begin{bmatrix} N^I_{,1} & 0 & 0 \\ N^I_{,1} & 0 & 0 \\ N^I_{,1} & 0 & 0 \\ 0 & N^I_{,1} & 0 \\ 0 & N^I_{,2} & 0 \\ 0 & N^I_{,3} & 0 \\ 0 & 0 & N^I_{,1} \\ 0 & 0 & N^I_{,2} \\ 0 & 0 & N^I_{,3} \end{bmatrix} \begin{bmatrix} {}^u d_1^I \\ {}^u d_2^I \\ {}^u d_3^I \end{bmatrix}. \tag{115}$$

For the interpolation of the stress tensor it is distinguished between the different element

types. For RT_mP_k three degrees of freedom (the local traction vector) per interpolation site are given. The general form of this interpolation is given as

$$\boldsymbol{P} = \begin{bmatrix} P_{11} & P_{12} & P_{13} \\ P_{21} & P_{22} & P_{23} \\ P_{31} & P_{32} & P_{33} \end{bmatrix} = \sum_J \begin{bmatrix} \Psi_1^J \, {}^p\!d_1^J & \Psi_2^J \, {}^p\!d_1^J & \Psi_3^J \, {}^p\!d_1^J \\ \Psi_1^J \, {}^p\!d_2^J & \Psi_2^J \, {}^p\!d_2^J & \Psi_3^J \, {}^p\!d_2^J \\ \Psi_1^J \, {}^p\!d_3^J & \Psi_2^J \, {}^p\!d_3^J & \Psi_3^J \, {}^p\!d_3^J \end{bmatrix}. \tag{116}$$

Restoring the tensor $\boldsymbol{P}$ as a vector yields the interpolation matrix $\boldsymbol{A}$ as

$$\boldsymbol{P} = \begin{bmatrix} P_{11} \\ P_{12} \\ P_{13} \\ P_{21} \\ P_{22} \\ P_{23} \\ P_{31} \\ P_{32} \\ P_{33} \end{bmatrix} = \sum_J \boldsymbol{A}^J \, {}^p\!\boldsymbol{d}^J = \sum_J \begin{bmatrix} \Psi_1^J & 0 & 0 \\ \Psi_2^J & 0 & 0 \\ \Psi_3^J & 0 & 0 \\ 0 & \Psi_1^J & 0 \\ 0 & \Psi_2^J & 0 \\ 0 & \Psi_3^J & 0 \\ 0 & 0 & \Psi_1^J \\ 0 & 0 & \Psi_2^J \\ 0 & 0 & \Psi_3^J \end{bmatrix} \begin{bmatrix} {}^p\!d_1^J \\ {}^p\!d_2^J \\ {}^p\!d_3^J \end{bmatrix}. \tag{117}$$

The divergence of the first Piola-Kirchhoff stress tensor can be obtained by the additional operator matrix $\boldsymbol{D}$,

$$\operatorname{Div} \boldsymbol{P} = \begin{bmatrix} P_{11,1} + P_{12,2} + P_{13,3} \\ P_{21,1} + P_{22,2} + P_{23,3} \\ P_{31,1} + P_{32,2} + P_{33,3} \end{bmatrix} = \sum_J \boldsymbol{D}\boldsymbol{A}^J \, {}^p\!\boldsymbol{d}^J = \sum_J \begin{bmatrix} \frac{\partial}{\partial x_1} & 0 & 0 \\ \frac{\partial}{\partial x_2} & 0 & 0 \\ \frac{\partial}{\partial x_3} & 0 & 0 \\ 0 & \frac{\partial}{\partial x_1} & 0 \\ 0 & \frac{\partial}{\partial x_2} & 0 \\ 0 & \frac{\partial}{\partial x_3} & 0 \\ 0 & 0 & \frac{\partial}{\partial x_1} \\ 0 & 0 & \frac{\partial}{\partial x_2} \\ 0 & 0 & \frac{\partial}{\partial x_3} \end{bmatrix}^T \boldsymbol{A}^J \, {}^p\!\boldsymbol{d}^J. \tag{118}$$

For the interpolation of the stresses in $W^{1,p}(\mathcal{B})$ leading to the element type P_mP_k each interpolation site has nine degrees of freedom, as each entry of the stress tensor is used. The general form of this interpolation is given by

$$\boldsymbol{P} = \begin{bmatrix} P_{11} & P_{12} & P_{13} \\ P_{21} & P_{22} & P_{23} \\ P_{31} & P_{32} & P_{33} \end{bmatrix} = \sum_J \begin{bmatrix} N^J \, {}^P\!d^J_{11} & N^J \, {}^P\!d^J_{12} & N^J \, {}^P\!d^J_{13} \\ N^J \, {}^P\!d^J_{21} & N^J \, {}^P\!d^J_{22} & N^J \, {}^P\!d^J_{23} \\ N^J \, {}^P\!d^J_{31} & N^J \, {}^P\!d^J_{32} & N^J \, {}^P\!d^J_{33} \end{bmatrix} . \tag{119}$$

Rewriting the stress tensor as a vector yields a different interpolation matrix $\hat{\boldsymbol{A}}$ and a different vector of stress degrees of freedom as

$$\boldsymbol{P} = \begin{bmatrix} P_{11} \\ P_{12} \\ P_{13} \\ P_{21} \\ P_{22} \\ P_{23} \\ P_{31} \\ P_{32} \\ P_{33} \end{bmatrix} = \sum_J \hat{\boldsymbol{A}}^J \, {}^P\!\boldsymbol{d}^J = \sum_J \begin{bmatrix} N^J & 0 & 0 & 0 & 0 & 0 & 0 & 0 & 0 \\ 0 & N^J & 0 & 0 & 0 & 0 & 0 & 0 & 0 \\ 0 & 0 & N^J & 0 & 0 & 0 & 0 & 0 & 0 \\ 0 & 0 & 0 & N^J & 0 & 0 & 0 & 0 & 0 \\ 0 & 0 & 0 & 0 & N^J & 0 & 0 & 0 & 0 \\ 0 & 0 & 0 & 0 & 0 & N^J & 0 & 0 & 0 \\ 0 & 0 & 0 & 0 & 0 & 0 & N^J & 0 & 0 \\ 0 & 0 & 0 & 0 & 0 & 0 & 0 & N^J & 0 \\ 0 & 0 & 0 & 0 & 0 & 0 & 0 & 0 & N^J \end{bmatrix} \begin{bmatrix} {}^P\!d^J_{11} \\ {}^P\!d^J_{12} \\ {}^P\!d^J_{13} \\ {}^P\!d^J_{21} \\ {}^P\!d^J_{22} \\ {}^P\!d^J_{23} \\ {}^P\!d^J_{31} \\ {}^P\!d^J_{32} \\ {}^P\!d^J_{33} \end{bmatrix} . \tag{120}$$

The divergence can be obtained by using Equation (118) under consideration of the matrix $\hat{\boldsymbol{A}}$ of Equation (120).

4.6. Boundary conditions

For the solution of a boundary value problem, the application of boundary conditions is important. With the displacements $\boldsymbol{u}$ and the stresses $\boldsymbol{P}$ as field quantities, the boundary can be divided into

$$\partial\mathcal{B} = \partial\mathcal{B}_u \cup \partial\mathcal{B}_P \;\wedge\; \partial\mathcal{B}_u \cap \partial\mathcal{B}_P = \emptyset \, . \tag{121}$$

In general two different kinds of boundary conditions are given, essential boundary conditions and natural boundary conditions. The essential boundary conditions are used for primary variables, whereas natural boundary conditions are used for the derivative of a primary variable. Thus for the considered least-squares mixed finite element formulation, all boundary conditions can be seen as essential ones,

$$\boldsymbol{u} = \boldsymbol{g} \quad \text{on } \partial\mathcal{B}_u \subseteq \partial\mathcal{B} \quad \text{and} \quad \boldsymbol{P} = \boldsymbol{h} \quad \text{on } \partial\mathcal{B}_P \subseteq \partial\mathcal{B} \, , \tag{122}$$

with vanishing variations on the boundaries,

$$\delta\boldsymbol{u} = 0 \text{ on } \partial\mathcal{B}_u , \qquad \delta\boldsymbol{P} = 0 \text{ on } \partial\mathcal{B}_P \, . \tag{123}$$

The application of the displacement boundary conditions can be done as in standard solely displacement based finite element methods. Therefore, for static analysis, all rigid-body motions have to be prevented. In the standard displacement-based FEM the zero Neumann boundary conditions for stress-free edges (natural boundary conditions) are generally fulfilled apriori (due to the resulting term in the weak form). In the framework of the provided mixed least-squares stress-displacement formulation this is not the case and therefore also zero-stress boundary conditions have to be defined explicitly. The acting stress at a boundary can be described by the so-called traction vector, see also Chapter 2.2. For simplification the following explanations are restricted to the two dimensional case ($x_1 - x_2$ plane), see Figure 16, where just the positive cutting surfaces are marked.

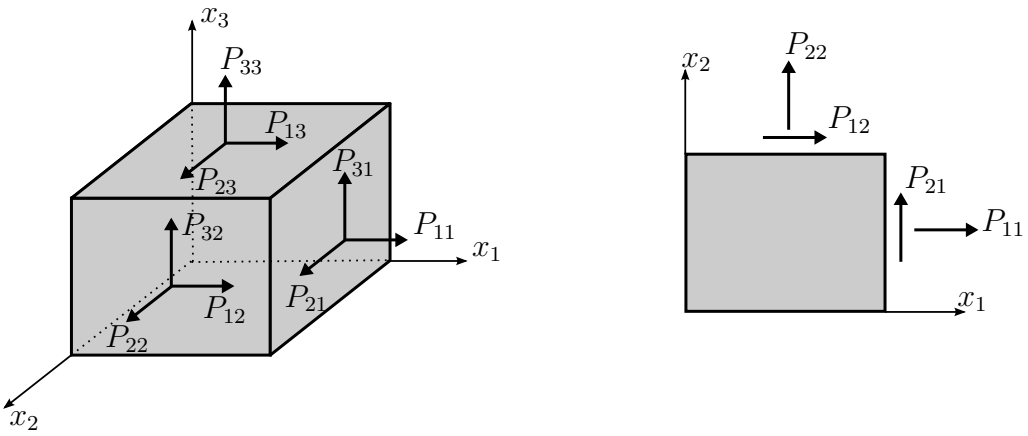

Figure 16: Stress state of an infinitesimal part.

With this definition of the stress tensor respectively the entries of the local traction vector shown in Figure 16 the boundary conditions are given for a simple example for both element types, RT_mP_k and P_mP_k.

4.6.1. Example for the application of boundary conditions As a simple example an uniaxial tension test is considered, see Figure 17.

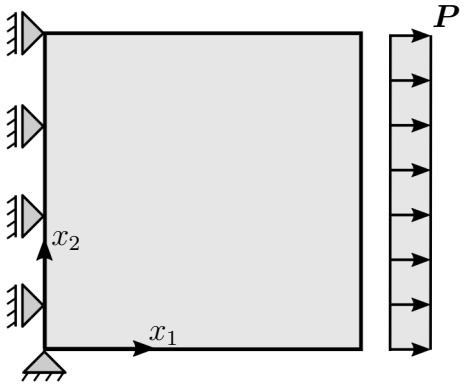

Figure 17: Geometry of the uniaxial tension test.

For both element types, RT_mP_k and P_mP_k the boundary conditions for the displacements are applied via the vector of nodal displacements $\overset{w}{\boldsymbol{d}}{}^I = (\overset{w}{d}{}_1^I, \overset{w}{d}{}_2^I)^T$. Considering this ex-

ample that means that all displacement nodes on the left side are bounded in x_1 direction and the node in the origin is additionally fixed in x_2 direction. The upper and lower side of the domain are stress free. Therefore, all stress nodes on the upper and lower side yield $\boldsymbol{T} = \boldsymbol{PN} = (P_{12}, P_{22})^T = \boldsymbol{0}$. For RT_mP_k this results in $\mathcal{d}_1^I = \mathcal{d}_2^I = 0$ and for P_mP_k in $\mathcal{d}_{12}^I = \mathcal{d}_{22}^I = 0$. On the left side only the shear stress has to be bounded, as the normal direction is already bounded by a displacement boundary (RT_mP_k: $\mathcal{d}_2^I = 0$, P_mP_k: $\mathcal{d}_{21}^I = 0$). On the right side a P_{11} stress is applied leading to the boundary conditions for RT_mP_k of $\mathcal{d}_1^I = P_{11}$, $\mathcal{d}_2^I = 0$ and for P_mP_k of $\mathcal{d}_{11}^I = P_{11}$, $\mathcal{d}_{21}^I = 0$. It should be remarked, that the application of the boundary conditions for P_mP_k could lead to problems, as the entries of the local traction vector are, under consideration of nonrectangular domains, not equal to entries of the local stress tensor. In order to circumvent this, the stress boundaries can e.g. be applied in a least-squares sense via an additional residual which is only defined at the stress boundaries. Therefore, in the framework of this thesis, the functional given in Equation (68) is extended by a boundary residual

$$\mathcal{R}_{\partial\mathcal{B}_P} = \boldsymbol{PN} - \boldsymbol{T} = \boldsymbol{0} \tag{124}$$

to the general least-squares functional for hyperelastcity leading to

$$\begin{aligned}
\mathcal{F}^e(\boldsymbol{P}, \boldsymbol{u}) &= \frac{1}{2}\int_{\mathcal{B}^e} \omega_1^2(\operatorname{Div}\boldsymbol{P} + \boldsymbol{f}) \cdot (\operatorname{Div}\boldsymbol{P} + \boldsymbol{f})\,\mathrm{d}V \\
&+ \frac{1}{2}\int_{\mathcal{B}^e} \omega_2^2(\boldsymbol{P} - \rho_0\partial_F\psi(\boldsymbol{C})) : (\boldsymbol{P} - \rho_0\partial_F\psi(\boldsymbol{C}))\,\mathrm{d}V \\
&+ \frac{1}{2}\int_{\mathcal{B}^e} \omega_3^2(\boldsymbol{F}^{-1}\boldsymbol{P} - (\boldsymbol{F}^{-1}\boldsymbol{P})^T) : (\boldsymbol{F}^{-1}\boldsymbol{P} - (\boldsymbol{F}^{-1}\boldsymbol{P})^T)\,\mathrm{d}V \\
&+ \frac{1}{2}\int_{\partial\mathcal{B}_P^e} (\boldsymbol{PN} - \boldsymbol{T}) \cdot (\boldsymbol{PN} - \boldsymbol{T})\,\mathrm{d}A\,.
\end{aligned} \tag{125}$$

Furthermore, applying the interpolation functions of Raviart-Thomas type (RT_m) given in Chapter 3.3 could be unconvenient for $m \geq 2$, as the interpolation functions are not one at its site and zero at the other sides due to the construction. Hence, for more convenience, the alternative functions given in Chapter 3.4 should be used.

4.7. Remarks on the implementation

In this subsection some basic remarks on the implementation are given. The detailed setup of least-squares elements is described in the internal Wiki for AceGen and AceFEM, see AceDoc [2016]. It should be remarked, that the notation over time has changed. Hence the notation in this thesis differs slightly from AceDoc [2016].

4.7.1. General remarks Mainly all explanations are restricted to the two-dimensional case. In the framework of this thesis, all given quantities as e.g. dimensions and material parameters are denoted without any units and have to be chosen in a consistent manner (e.g. in SI units). The element implementations and computations have been done using

the *AceGen* and *AceFEM* packages (version 6.503 – 6.808), see e.g. Korelc [1997; 2002] and Korelc and Wriggers [2016], of *Mathematica* (version 10.1–10.4), see Wolfram Research [2015]. Furthermore, for the visualizations *Paraview* (version 4.3.1), see Ahrens et al. [2005], has been used. Basis for the contour plots of the stresses are the quantities evaluated at the corner nodes of each triangle. Inside an element the values are interpolated linearly, between elements the plot is discontinuous. The used mixed Galerkin element T_2P_0 is based on the three field Hu-Washizu potential, compare Simo et al. [1984]

$$\Pi(\boldsymbol{u}, p, \theta) = \int_{\mathcal{B}_0} \psi(\overline{\boldsymbol{F}})\ \mathrm{d}V + \int_{\mathcal{B}_0} p(J-\theta)\ \mathrm{d}V + \Pi^{\mathrm{ext}} \quad \rightarrow \quad \text{stat.}$$

with $\overline{\boldsymbol{F}} = (\frac{\theta}{J})^{1/3}\boldsymbol{F}$. The displacement $\boldsymbol{u}$ is interpolated using quadratic standard interpolation polynomials whereas p and θ are interpolated constant and discontinuous from element to element. All provided two-dimensional computations assume plain strain conditions.

4.7.2. General element setup in AceGen For the implementation it is distinguished between nodes associated to stresses and nodes associated to displacements, even if they are at the same coordinate. This results in the number of nodes given in Chapter 4.5, Table 4. A linear three-noded triangular element is chosen as a basis for each element (thus the provided elements are restricted to straight edges). All further nodes are added using the "SMSAdditionalNodes" command, see exemplary for an RT_1P_2 in Figure 18.

```
"SMSAdditionalNodes"→
Hold[{#1+2 (#2-#1)/4, #2+2 (#3-#2)/4, #3+2 (#1-#3)/4,
    #1+(#2-#1)/3, #1+2 (#2-#1)/3, #2+(#3-#2)/3, #2+2 (#3-#2)/3,
    #3+(#1-#3)/3, #3+2 (#1-#3)/3, #1+(#2-#1)/3+(#3-#1)/3, #1+(#2-#1)/3+(#3-#1)/3}&]
```

Figure 18: Adding further additional nodes using the "SMSAdditionalNodes" command exemplary for RT_1P_2.

The nodes are marked with the "SMSNodeID" command using the denotations "D" for a displacement node and "Sig" for a stress node. Each displacement node has two degrees of freedom. Each stress node for RT_mP_k two degrees of freedom and for P_mP_k four degrees of freedom. The arising integrals are solved using Gaussian quadrature with a sufficient number of integration points. The isoparametric concept is used, that means that for the interpolation of the geometry the same interpolation functions as for the interpolation of the displacement field are used,

$$\boldsymbol{u} = \sum_I N^I\, {}^{u}\boldsymbol{d}^I \quad \text{and} \quad \boldsymbol{X} = \sum_I N^I \boldsymbol{X}^I\,. \tag{126}$$

After defining the necessary fields for the degrees of freedom, the kinematical quantities are computed, see Figure 19.

```
∇u=SMSD[{ux,uy,uz},{dX,dY,dZ},
"Dependency"→{{ξ,η,ζ},{dX,dY,dZ},SMSSimplify[SMSInverse[dJm]]}];
SMSFreeze[F,IdentityMatrix[3]+∇u];
SMSFreeze[C,Transpose[F].F,"Symmetric"→True];
{I1,I2,I3}=SMSInvariantsI[C];
```

Figure 19: Computation of the kinematic quantities.

For $P_m P_k$ no special treatment is neccesary for the interpolation respectively implementation of the stress degrees of freedom, as all entries of the stress tensor are degrees of freedom at each node. For $RT_m P_k$ it has to be taken under consideration, that the degrees of freedom are the local traction vector. Since this is dependent on the position of the element edge of consideration, the local normal has to be computed. Unfortunately, the normals $N_{1,1}$ and $N_{2,1}$ of two neighbouring elements E_1 and E_2 are diametrically opposed, see Figure 20 (left).

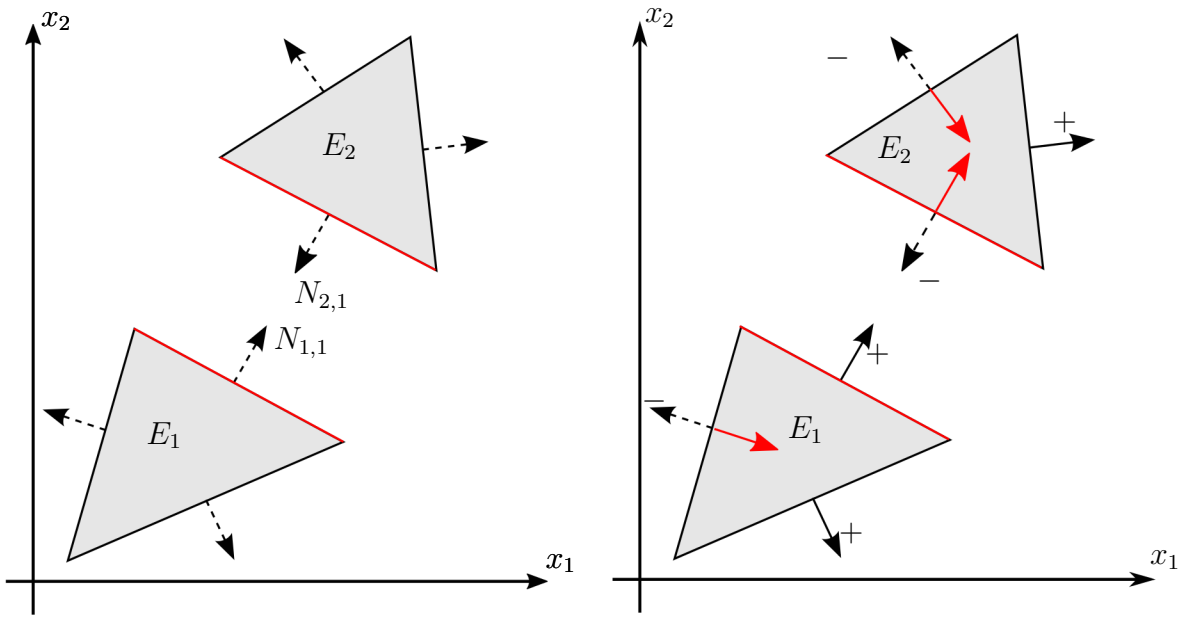

Figure 20: Two elements sharing one edge, orientation of the normal for the local traction vector.

Since at one edge only one normal can exist (because at a shared node on this edge the local traction vector has to be the same for both element), a "positive" normal direction is defined. That means that all normals pointing towards the positive x_1 direction maintain their normal, whereas the other normal becomes turned (multiplied by minus one), see Figure 20 (right). In borderline cases the positive x_2 direction is decisive. In the sequel the free energy of consideration is defined in terms of the principal invariants of the right Cauchy-Green tensor $\boldsymbol{C}$, see exemplary a Neo-Hooke free energy in Figure 21.

The second residual demands the first Piola-Kirchhoff stress tensor $\boldsymbol{P}$ to be equal to the derivative of the free energy function with respect to the deformation gradient $\boldsymbol{F}$. The

```
Ψiso := 1/4 λ (I3-1) - (λ/2 + μ) Log[SMSSqrt[I3]] + 1/2 μ (I1-3);
```

Figure 21: Definition of the free energy function.

derivative is executed using automatic differentiation, which is a main feature of AceGen, see Figure 22.

```
dΨdF := SMSD[Ψ, F, "IgnoreNumbers" → True];
```

Figure 22: Automatic differentiation of the free energy with respect to the deformation gradient $\boldsymbol{F}$.

Now the least squares functional $\mathcal{F}$ is built using the squared $L^2(\mathcal{B})$-norms of the residuals. Utilizing automatic differentiation, the first and the second variation are then computed, see Figure 23.

```
SMSDo[i, 1, Length[at]];
δℱ := SMSD[ℱ, at, i] dvol;
SMSExport[SMSResidualSign δℱ, p$$[i], "AddIn" → True];
SMSDo[j, i, Length[at]];
Δδℱ = SMSD[δℱ, at, j];
SMSExport[Δδℱ, s$$[i, j], "AddIn" → True];
SMSEndDo[];
```

Figure 23: Applying automatic differentiation and filling right-hand-side and stiffness matrix.

5 Investigation of the performance of different element types under consideration of different physical quantities and influence of scalar weighting

In this section, the ability of the provided least-squares formulation to compute reliable results for all quantities of interest is investigated. Therefore, several benchmark problems are taken under consideration. In order to compare the results to well known discretization schemes, a standard (T_2) as well as a mixed Galerkin finite element (T_2P_0) is used.
First, the solution for the displacement field is considered. As mentioned before, a benefit of the method is the free choice of interpolation orders for the field quantities of the mixed least-squares elements. This leads to the question, if there are any interpolation combinations which perform better than other ones. Therefore, an extensive convergence study considering the boundary value problem of a cantilever beam is provided. Here, beside different interpolation orders also different interpolation space combinations for the unknown quantities and different resulting element types, see also Chapter 4.5, are investigated.
The second example considers the same boundary value problem and aims to investigate the influence of the scalar weighting factor ω_3 on the performance of bending domiated problems. The constitutive relation used for this example is given by a free energy function of Mooney-Rivlin type, see Chapter 2.3.2.
For all further computations considering isotropic materials, the constitutive relation is given by a free energy function of Neo-Hookean type, compare Chapter 2.3.1. The next boundary value problem under consideration is the well known Cook's Membrane problem. Here, the stress distribution of the provided least-squares finite element is compared to a standard (T_2) and a mixed Galerkin element (T_2P_0) for an incompressible material, since the approximation of the stresses for incompressible materials is a well-known issue for standard Galerkin elements. Furthermore, the ability of the provided least-squares formulation to compute support reactions is investigated on this example.
As the natural space for the interpolation of the stresses is $W^q(\mathrm{div}, \mathcal{B})$, the interpolation of the stresses in $W^{1,p}(\mathcal{B})$ may lead to problems in the case of material transitions. This is due to the fact of a possible physical discontinuity of the non-normal components of the stress tensor. The following example of a quartered plate aims to show the performance and possible issues of the different element types with respect to the computation of stresses for a boundary value problem consisting of different materials.
In the next example the benchmark of the compression test is provided, compare Reese and Wriggers [2000]. Here, especially the compliance with the incompressibility constraint is taken under consideration.
Taking into account a three-dimensional example, the benchmark problem of a clamped plate is taken under consideration. Here, the convergence of the tip displacement for an element of type RT_0P_2 and the resulting stress distribution over the domain is shown and compared to a standard Galerkin element. The investigated material is assumed to be compressible.
In the last example in this chapter, the performance of the least-squares formulation under assumption of a transversely isotropic material is shown. The free energy function is given in Chapter 2.3.3. Considering the boundary value problem of a cantilever under the assumption of a compressible material the deflection of the beam under different angles of the preferred direction γ are investigated. As a reference solution a standard Galerkin element (T_2) is used.

5.1 Cantilever beam, performance study

First, the performance of the provided element formulation with the residuals weighted as $\omega_1 = 1, \omega_2 = \omega_3 = 1/\mu$ is considered. In detail, the convergence of the vertical displacement at the upper right node of a cantilever beam, see Figure 24, under plain strain conditions, using different interpolation orders for the displacements ($k = 1, 2, 3, 4$) and the stresses ($m = 0, 1, 2$) for the elements RT_mP_k respectively $m = 1, 2, 3, 4$, $k = 1, 2, 3, 4$ for the element types P_mP_k is investigated.

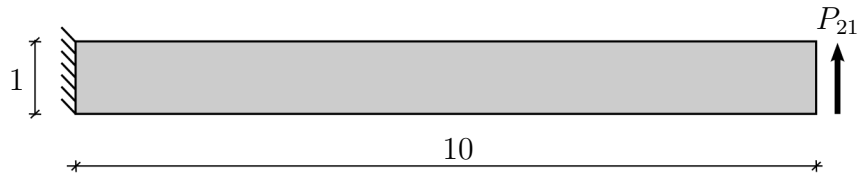

Figure 24: Geometry of the cantilever beam.

As already mentioned, the polynomial orders could be chosen arbitrary since the method is not restricted to the LBB-condition. For comparison a mixed Galerkin element (triangle, quadratic displacement, constant pressure $\rightarrow T_2P_0$) is used. The material is given by a free energy function of Mooney-Rivlin type, see Chapter 2.3.2, with the parameters $\lambda = 172.84, \mu = 74.0741, \xi = 0.5$ (Young's modulus $E = 200$, Poisson's ratio $\nu = 0.35$). The final outcome of this investigation should be a statement, which interpolation combination is recommendable considering such a bending dominated problem. The left side of the beam has a fixed displacement boundary ($u_1 = u_2 = 0$). The upper and lower edges are assumed to be stress-free ($\boldsymbol{PN} = (0, 0)^T$). The system is loaded by a shear-stress on the right side with $\boldsymbol{PN} = (0, 0.1)^T$. In Figure 25 the convergence of the tip displacement of the different elements of type RT_mP_k is depicted. It can be seen, that the choice of $m = 0$ for the stress interpolation does not give good results for the provided formulation, even if the interpolation of the displacement is of quartic order. For lower k the performance is even slightly better. This is due to the fact, that the higher interpolation order for the displacement cannot cure the weak approximation of the stresses but leads to more degrees of freedom per element and consequently a higher number of equations *neq*. The results for $m = 1$ show a, more or less, uniform performance for all combinations except for $k = 1$. This effect can also be seen in the results for $m = 2$ and $m = 3$. Hence, considering this boundary value problem and using the proposed weighting factors, the linear interpolation of the displacements is not recommendable as well as the lowest order stress interpolation $m = 0$. Since the stresses are assigned to the derivative of the displacements and the mathematically expected convergence orders in the respective interpolation spaces $W^q(\mathrm{div}, \mathcal{B})$ and $W^{1,p}(\mathcal{B})$ for a choice of $k = m + 1$ are equal and due to the low performance of the lower order combinations, in the following the used two-dimensional elements of type RT_mP_k are used with $k = m+1$ and $k \geq 2$.

The convergence of the tip displacement of the upper right node for the P_mP_k elements is depicted in Figure 26. For this element type already the lowest interpolation order for the stresses with $m = 1$ leads to good results. However, the interpolation order for the stresses should be at least quadratic ($k \geq 2$). The best performance is obtained by choosing the

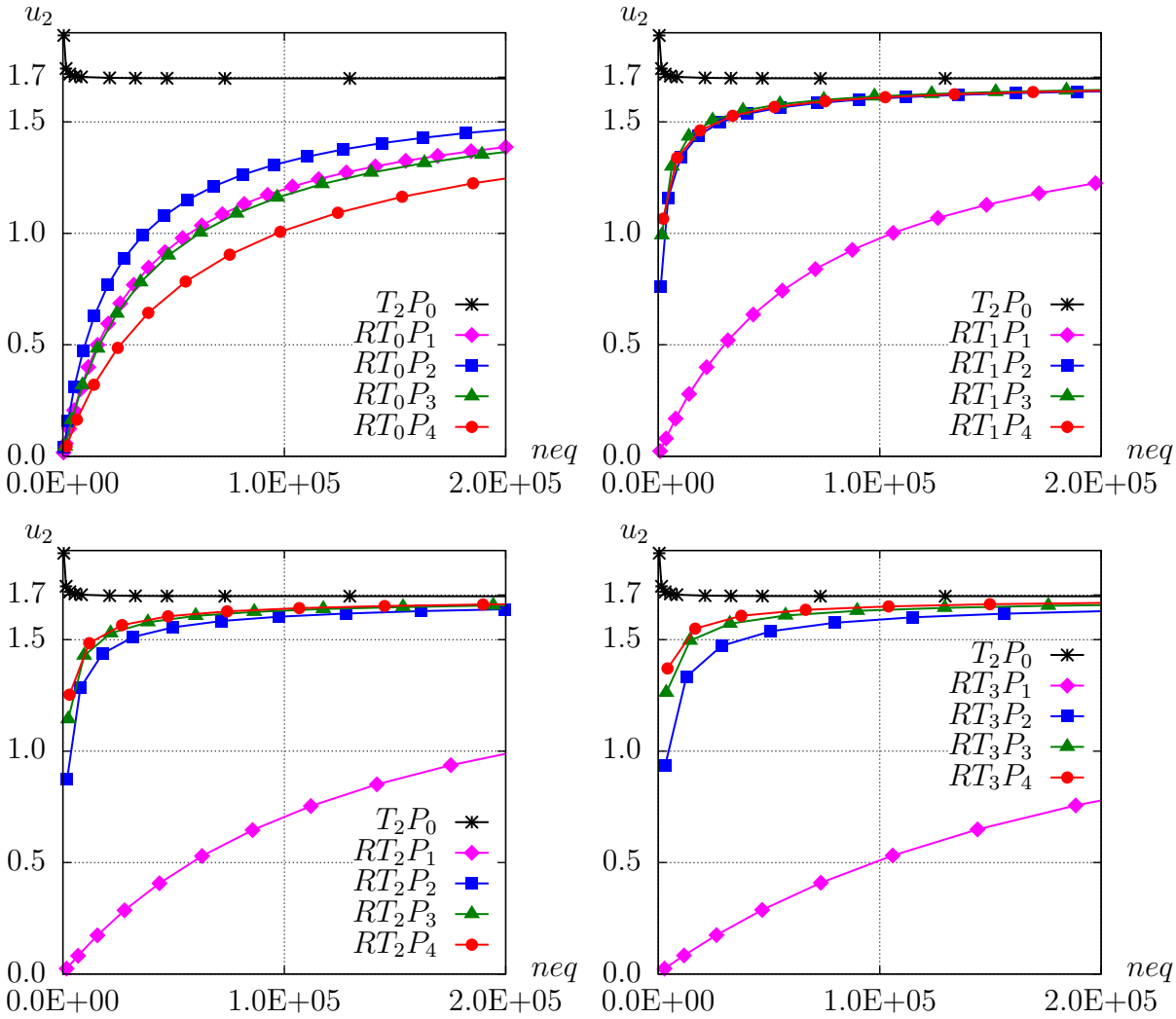

Figure 25: Displacement convergence for u_2 of the upper right node (10,1) over number of equations (neq) of the final system of equations for RT_mP_k .

interpolation order for the stresses one order lower than the interpolation order for the displacements. It can be stated, that the choice of $k = m + 1$ (respectively $k = m$) and $k \geq 2$ leads to the best results for P_mP_k. Therefore, in the following, these interpolation combinations are used. In summary both element types show a satisfying performance for the approximation of the tip displacement under consideration of a suitable interpolation combination and interpolation order. In Figure 27 the results for the recommended interpolation combinations of both element types are compared. Here it becomes viewable, that the elements of type P_mP_k show a slightly better performance. Comparing e.g. RT_1P_2 and P_1P_2 points out this effect. Although the interpolation function of RT_1P_2 has a minimally higher interpolation order for the approximation of the stresses (quasi quadratic compared to linear for P_mP_k), the performance of P_1P_2 is slightly better. The same statement is valid for the comparison of RT_2P_3 versus P_2P_3 and RT_3P_4 versus P_3P_4. This effect becomes even more significant considering the fact, that the P_mP_k elements have, due to the fact that all entries of the stress tensor are used as degrees of freedom, a higher number of element degrees of freedom, as shown in Chapter 4.5. Unfortunately, considering the results of the best elements provided in Figure 27, it can be seen, that

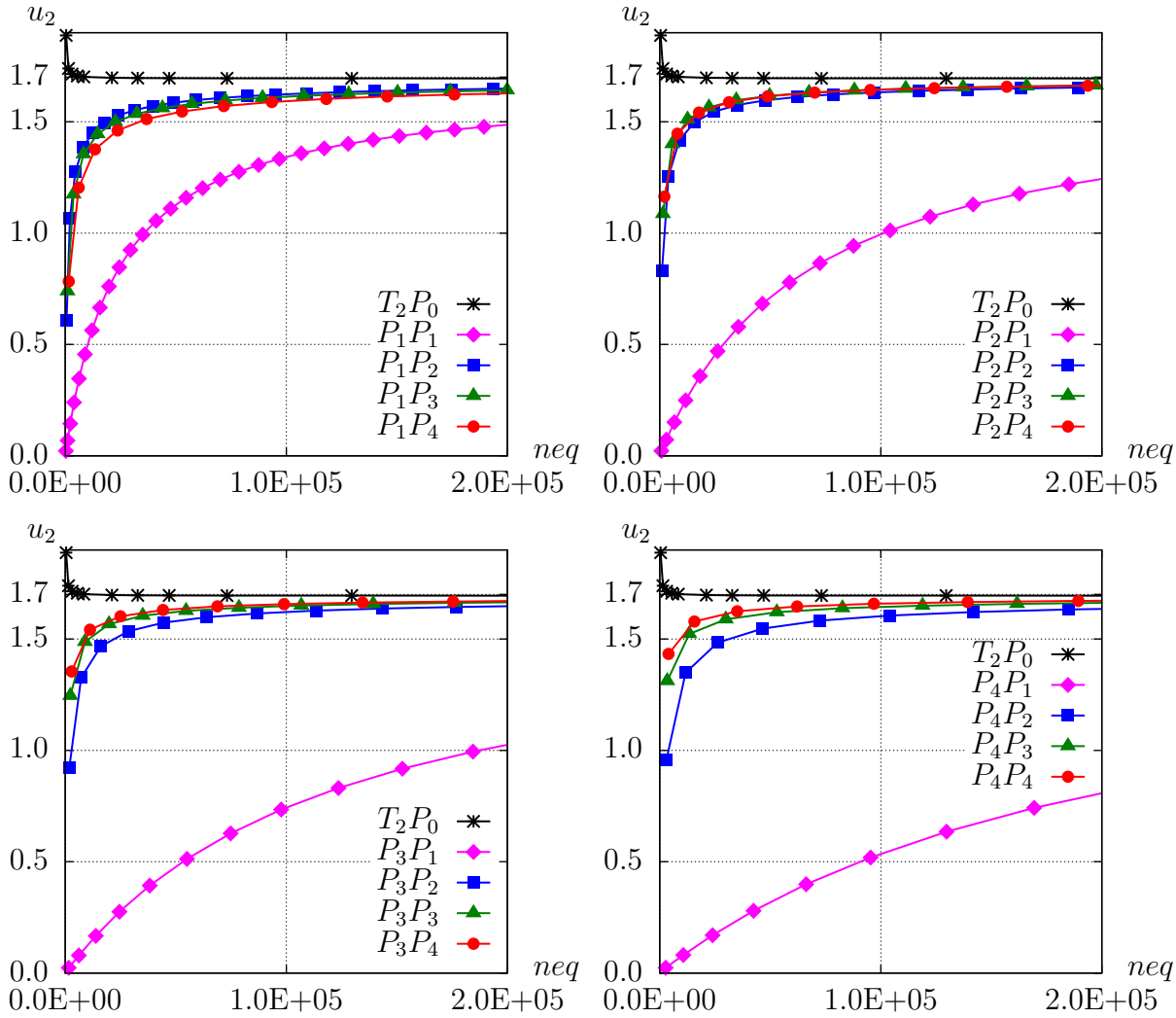

Figure 26: Displacement convergence for u_2 of the upper right node (10,1) over number of equations (neq) of the final system of equations for P_mP_k .

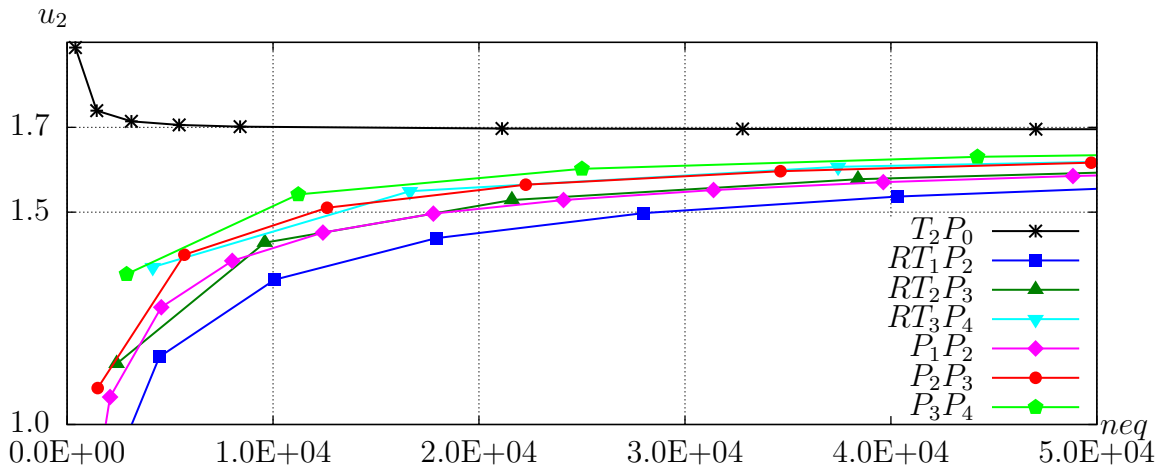

Figure 27: Displacement convergence for u_2 of the upper right node (10,1) over number of equations (neq) of the final system of equations for best tested combinations RT_mP_k and P_mP_k.

no element is able to reach with the used number of elements the solution computed by the mixed Galerkin element T_2P_0, which can be seen as a reference solution. This fact is not satisfactory as many degrees of freedom and high polynomial orders for the interpolation of the unknown fields are used. The reason for this deficiency can be found in the balancing of the residuals by the used weights ω_i. In order to demonstrate this and show the crucial impact of suitable weighting on the performance of the provided least-squares formulation, in the following section the same boundary value problem is investigated using different weighting factors ω_3.

5.2 Cantilever beam, influence of weighting

In this section, the influence of the third (redundant) residual $\mathcal{R}_3$ on the performance is investigated. Therefore, the same boundary value problem, see Figure 24 is considered, with a varying weighting factor $\omega_3 = 0, 1/\mu, 5/\mu, 10/\mu$, whereas $\omega_1 = 1, \omega_2 = 1/\mu$. As an element type RT_1P_2 is chosen. First, the tip displacement is taken under investigation. The results are depicted in Figure 28. In Section 5.1 the weight ω_3 has been chosen

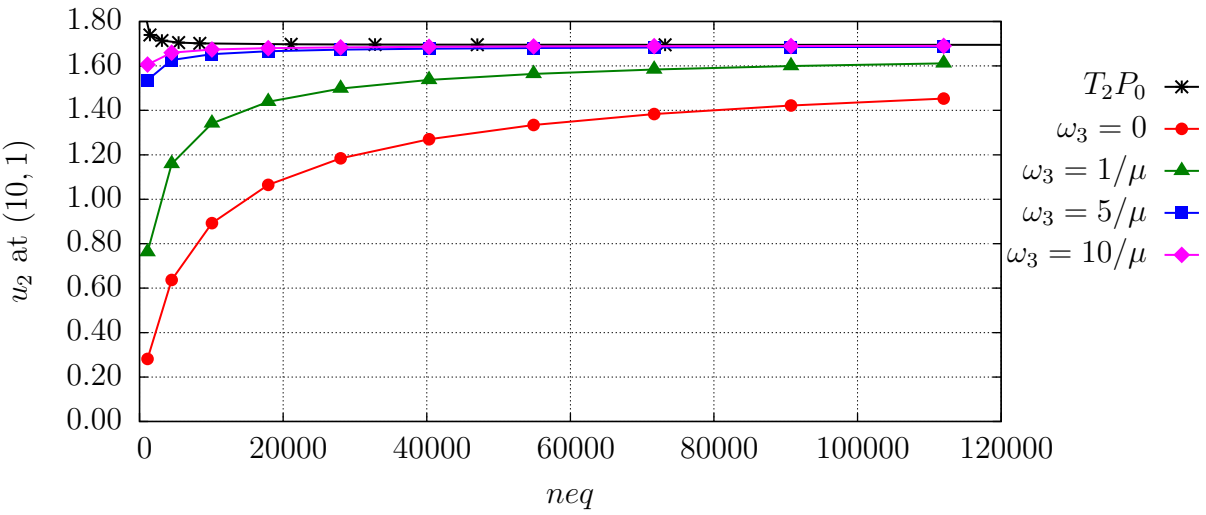

Figure 28: Plot of u_2-displacement of the upper right node (lower) for RT_1P_2 considering different weights ω_3.

as $\omega_3 = 1/\mu$. This result is here depicted by the green line. The crucial impact of a suitable choice of ω_3 can be seen. The raise of the weighting factor ω_3 up to $\omega_3 = 5/\mu$ respectively $\omega_3 = 10/\mu$ leads to an improvement of the solution up to the mixed Galerkin finite element T_2P_0. This effect can be explained by the dependence of the solution on different physical relations. A main assumption of the beam theory of *Bernoulli* is, that the bending of a beam is primary dependent on the bending moment and the bending due to shear forces are comparatively small and therefore neglectable. Considering a bending dominated problem as the cantilever beam, the compliance with the balance of moment of momentum, which can be associated to the symmetry of the stresses directly, has therefore a strong effect of the quality of the solution. Weighting this relation with a higher weight ω_3 the stress symmetry condition gets enforced and thus the solution gets improved. This can be confirmed considering the convergence of the squared $L^2(\mathcal{B})$-norms of the individual residuals ($||\mathcal{R}_i||^2_{L^2(\mathcal{B})}$) respectively the functional error $|\mathcal{F} - \mathcal{F}_h|$ plotted

over logarithmic scales, see Figure 29. Considering the residual values seperately for the different weightings it becomes clear, that the weighting of a residual leads to a stronger fulfillment of this condition, but as the weighting factor is part of the complete functional, it also affects the total functional error. Especially the plot of the functional error $|\mathcal{F}-\mathcal{F}_h|$ shows clearly, that the convergence order (the slope of the provided data) is steeper for $\omega_3 = 5/\mu$ and $\omega_3 = 10/\mu$ than for $\omega_3 = 0$ and $\omega_3 = 1/\mu$. The absolute value of the error for the higher weights $\omega_3 = 5/\mu$ and $\omega_3 = 10/\mu$ is larger, nevertheless, the result for the displacement is better. It is remarked that these results are transferable also on different element types RT_mP_k and interpolation combinations of type P_mP_k.

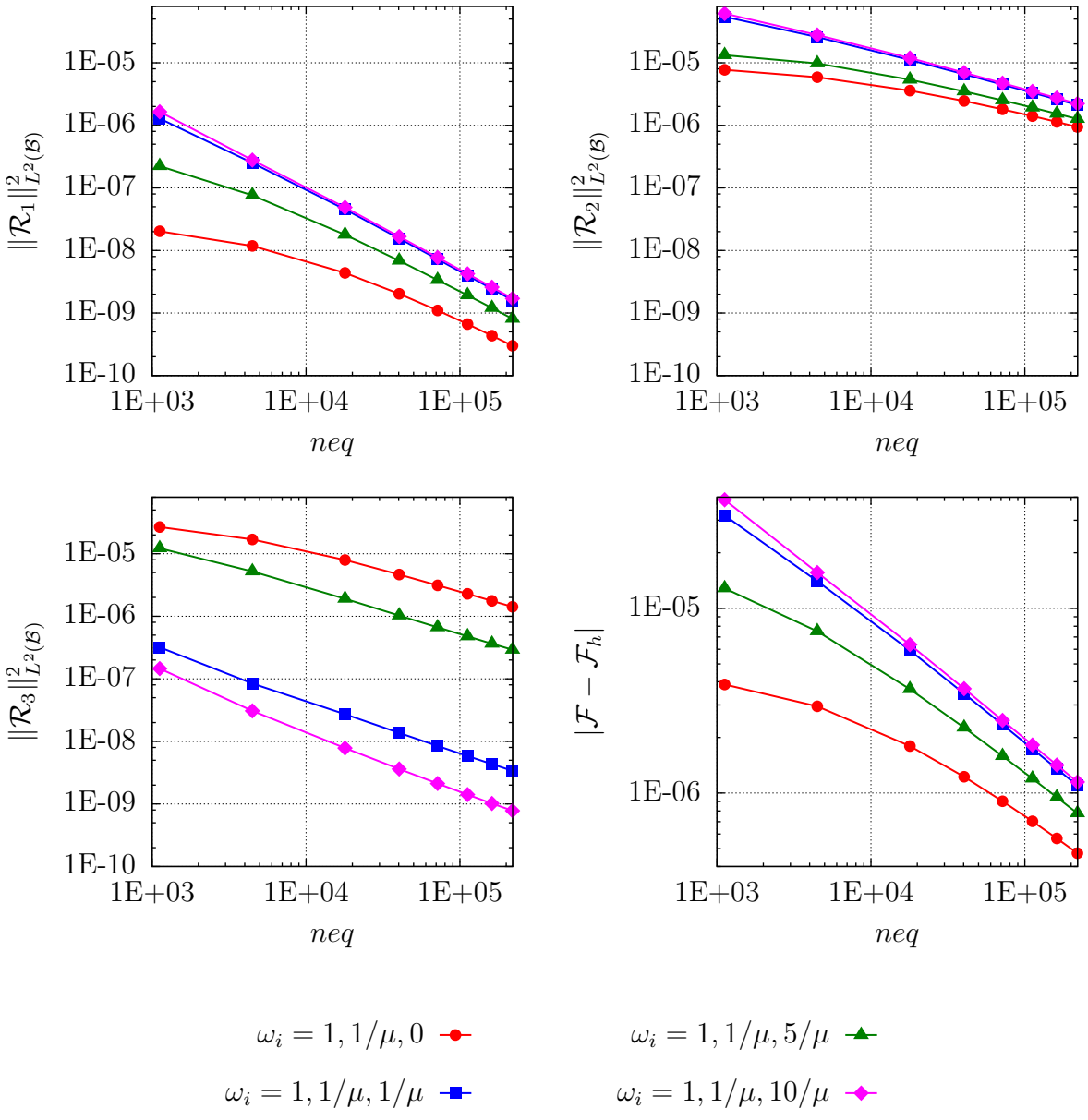

Figure 29: Plot of the squared $L_2(\mathcal{B})$ norms of the individual residuals $\mathcal{R}_i$ and plot of the functional error for different weights ω_i for RT_1P_2 .

5.3 Cook's Membrane, stress distribution and reaction forces

It has been shown in the last example (Section 5.1 and Section 5.2), that the provided formulation can give reliable results with respect to the displacements. In the following example the stress approximation of the mixed least-squares finite element is investigated in detail. Therefore, the well-known Cook's Membrane problem is considered for a quasi-incompressible material. The geometry and the utilized structured mesh with 800 elements is shown in Figure 30.

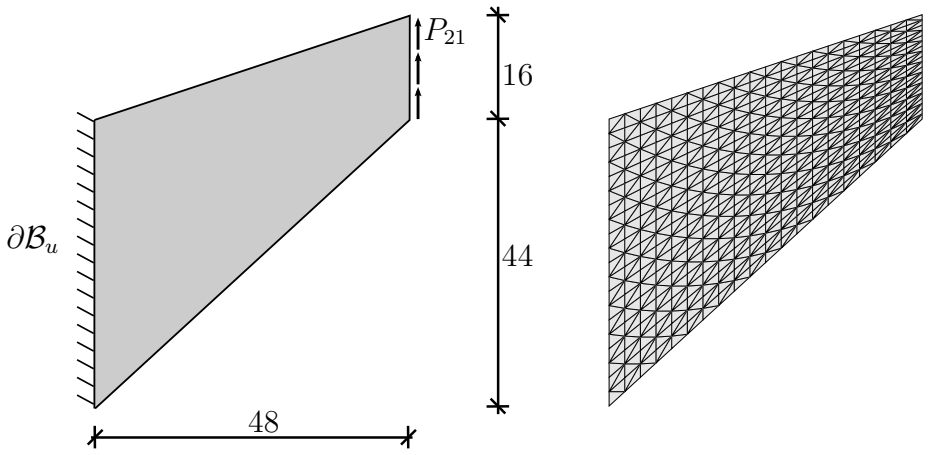

Figure 30: Geometry and mesh (20×20 elements) of the Cook's membrane.

The underlying free energy is of Neo-Hookean type, see Equation (28.1). This benchmark is well suited since it exhibits a stress singularity in the upper left corner. Furthermore, it is known that lower order standard methods produce for quasi-incompressible elastic material behavior an oscillating stress field. The left side of the geometry with dimensions of 48×60 is assumed to be a displacement boundary and clamped. The other edges are stress boundaries with the right edge $\boldsymbol{PN} = (0, 1)^T$ and stress-free boundary conditions at the upper and lower edge. In order to obtain a quasi-incompressible material behavior we apply a Poisson's ratio of $\nu = 0.499$. The Young's modulus is chosen as $E = 200$. The conversion to the Lamé parameters yields $\lambda = 33288.86$ and $\mu = 66.71$. For the comparison of the results a standard Galerkin quadratic triangular element (T_2) and a mixed Galerkin element of type T_2P_0 (triangular element, quadratic displacement, constant pressure) are used. The weights for the least-squares elements are chosen as $\omega_1 = 1, \omega_2 = 1/\mu, \omega_3 = 10/\mu$. First the displacement convergence of the vertical tip displacement is taken under consideration for the Galerkin elements and three least-squares elements (RT_1P_2, RT_2P_3 and RT_3P_4), see Figure 31.

It can be seen, that all used elements lead to the almost same result for the tip displacement. As it would be expected, the highest order least-squares element (RT_3P_4) provides the best solution compared to the elements with a lower interpolation order (RT_1P_2, RT_2P_3). The slight difference to the Galerkin elements can e.g. be overcome by adaptive mesh refinement as, due to the regular refinement and the higher number of element degrees of freedom. In order to show the positive effect of adaptive mesh refinement for the least-squares elements (and the possibility to use the functional as a local error indicator) see Chapter 7, where the raise of performance is shown using the example of a plate with a hole.

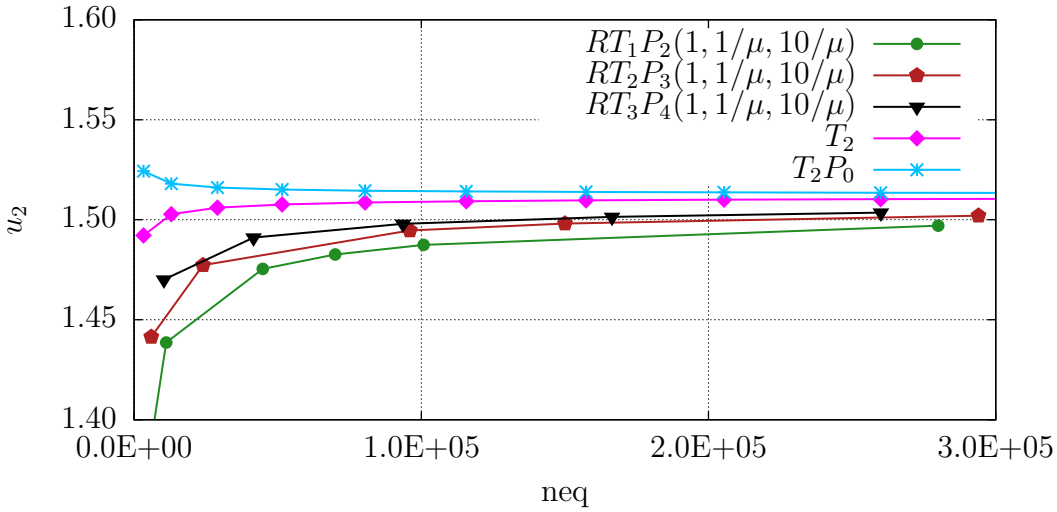

Figure 31: Displacement convergence of the upper right node with the coordinates (48,60) for different elements .

In a second step the approximation of the stress field is taken under consideration. Therefore, in Figure 32, the results for the stress component σ_{11} of the Cauchy stresses are plotted as an "out of the plane"-value. Using this graphical representation, it can be seen clearly, that the standard Galerkin formulation (T_2) shows oscillating stresses over the domain, whereas the mixed Galerkin formulation (T_2P_0) as well as the least-squares mixed finite element (RT_1P_2) provide a smooth stress approximation. Furthermore, quantitatively, the results for T_2P_0 and RT_1P_2 are nearly of the same size, whereas the standard Galerkin element T_2 results, due to its pathologic stresses, in a different range. Especially in the area of the singular corner respectively at the right side of the domain strong oscillations of the stresses for the standard Galerkin element can be considered. Due to this graphical representation of the stresses, the discontinuous stresses for the Galerkin element in contrast to the continuous stress interpolation (for the normal components) for the least-squares element becomes viewable. This results in a smoother stress distribution for the least-squares element. As a further result of the computation also the functional of the least-squares formulation is shown as a contour plot over the domain in Figure 32. Here it can be seen, that the functional error tends to be zero over the whole domain except for the upper left corner and the corners where the load is applied. The higher error at the right hand side is due to the constant load (a parabolic load would circumvent this occurence). The higher functional value at the upper side of the clamping is due to the stress singularity in this corner. Using the least-squares functional as a local error indicator for an adaptive mesh refinement strategy would lead to a refined mesh especially in the area of the singularity and raise the performance of the element crucially, see also Chapter 7.

Additionally the resulting reaction forces at the clamping in horizontal and vertical direction are investigated. Therefore, the different least-squares element types RT_1P_2 and P_1P_2 and the Galerkin elements T_2 and T_2P_0 are used. The considered boundary value problem is the same, see Figure 30, except that the load is reduced to $\boldsymbol{PN} = (0, 0.1)$. As a solution the sum of all forces F^I in horizontal (x_1) and vertical (x_2) direction are expected as

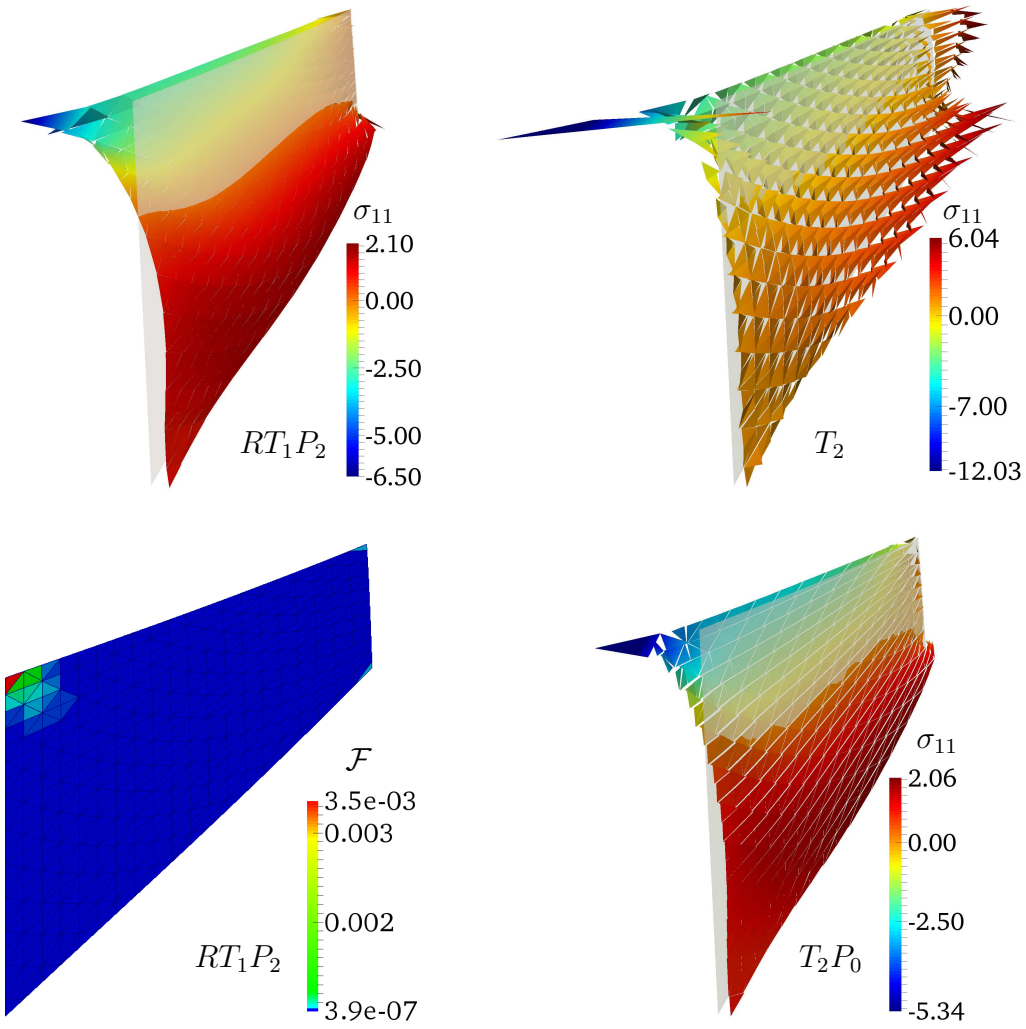

Figure 32: Distribution of the σ_{11} component of the Cauchy stresses for different elements and distribution of the functional error for RT_1P_2 (lower left).

$$\sum_{I\in\partial\mathcal{B}_u} F^I_{x_1} = 0 \quad \text{and} \quad \sum_{I\in\partial\mathcal{B}_u} F^I_{x_2} = 1.6\,.$$

For evaluation the normal component of the Cauchy stresses $\boldsymbol{\sigma n}$ at the boundary are considered for the least-squares elements and for the Galerkin elements. Therefore the function of the stresses is evaluated at the boundary. The integral of the reaction forces over the left clamped boundary is depicted in Figure 33. Here, beside the weighting $\omega_1 = 1, \omega_2 = \omega_3 = 1/\mu$ also a different weighting of $\omega_1 = 100, \omega_2 = 1/\mu$, $\omega_3 = 0$, compare also Müller [2015], is used which, inter alia, strenghtens the fulfillment of the momentum balance.

It becomes viewable, that all elements aim to converge to the right solution. However, the additional strenghtening of the momentum balance ($\omega_1 = 100, \omega_2 = 1/\mu, \omega_3 = 0$) provides a better performance for the least-squares element as the weighting with $\omega_1 = 1, \omega_2 = \omega_3 = 1/\mu$. The reason for this effect is the strenghtening of the "balance of all

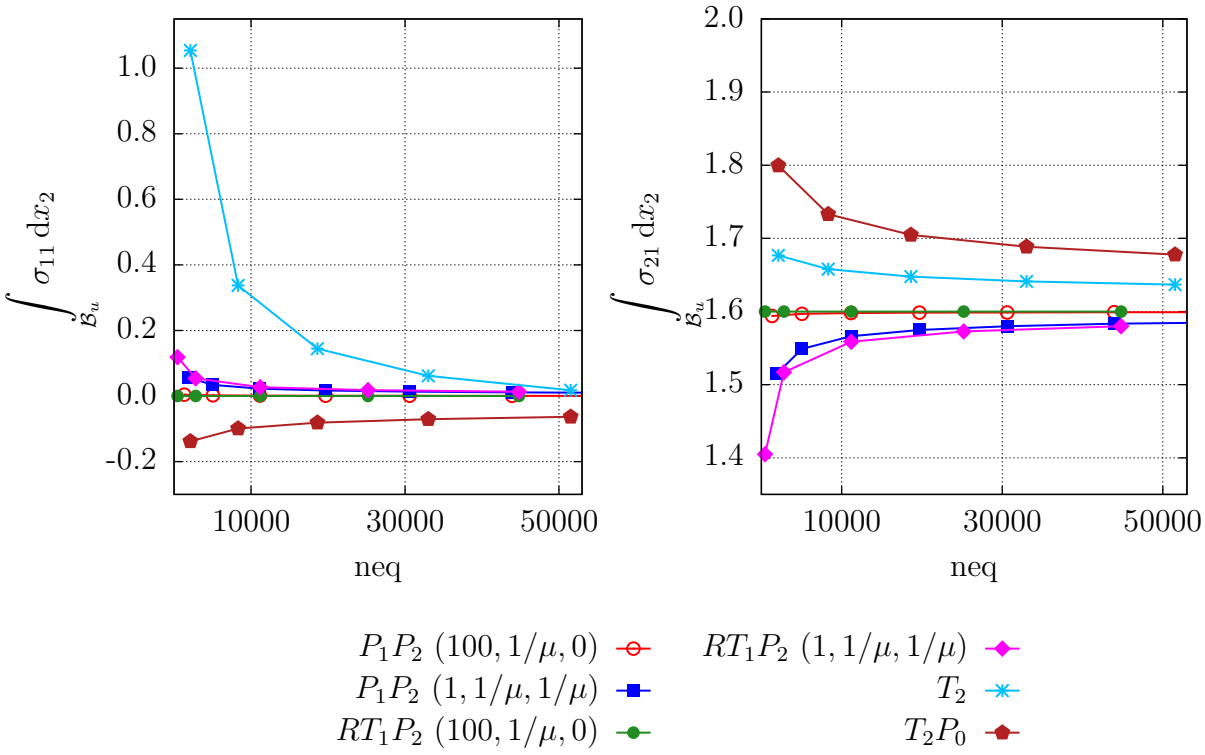

Figure 33: Resulting horizontal and vertical reaction forces for different elements .

(horizontal and vertical) forces" (the stronger weighting of the balance of momentum) and the resulting stronger fulfillment of the condition of equilibrium of all forces. Nevertheless, for a more refined mesh, also the other weighting combination leads to reasonable results.

For a more detailed investigation the course of the reaction forces is considered in the following for the different element types and different meshes. In Figure 34 the courses are depicted for two least-squares elements P_1P_2 and RT_1P_2 under consideration of different weights ω_i. In Figure 35 the results for the standard and the mixed Galerkin element are shown. Further computations can be found in the Appendix, see Chapter A.6. The results show that the standard Galerkin element T_2, as expected, fails to compute the correct course of the reaction forces. The computation of the course of the shear stress is, at least for fine meshes, done adequately, but the normal stress σ_{11} oscillates. This becomes especially viewable in the area of the singular corner, where although this area is completely under pressure, a tension stress appears. The mixed Galerkin element T_2P_0 performs in this regard much better. For coarse meshes the discontinuity of the stresses due the interpolation of the pressure in $L_2(\mathcal{B})$ is obvious, but for more refined meshes this effect is reduced. The least-squares elements compute the resulting stresses at the boundary in an appropriate way. Nevertheless, it has to be mentioned, that the choice of the weighting factors can lead to slightly different results, which is viewable in the upper area of the left boundary.

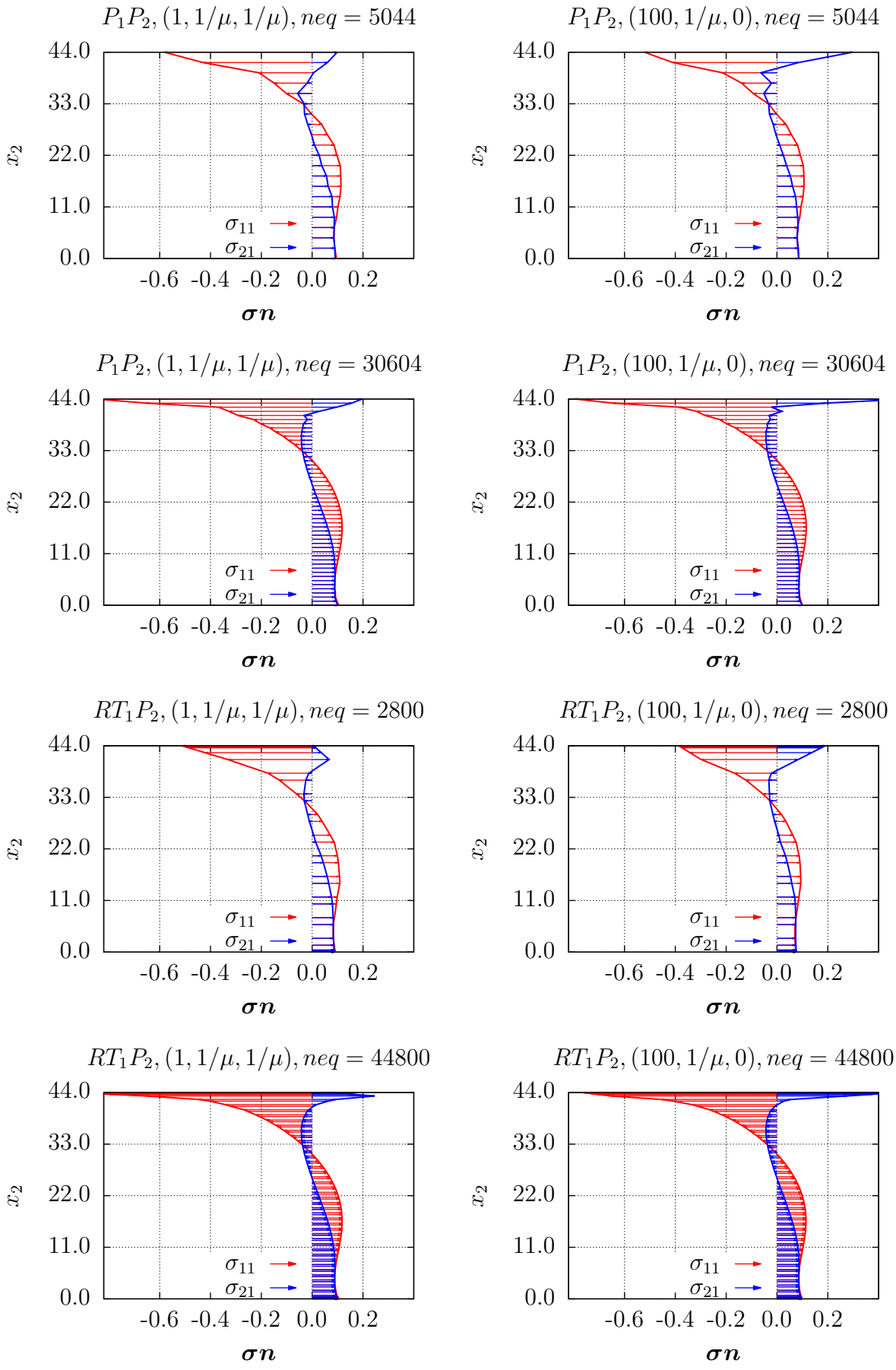

Figure 34: Course of the support reactions for the least-squares elements of type P_1P_2 and RT_1P_2 under consideration of different system sizes neq and different weights ω_i .

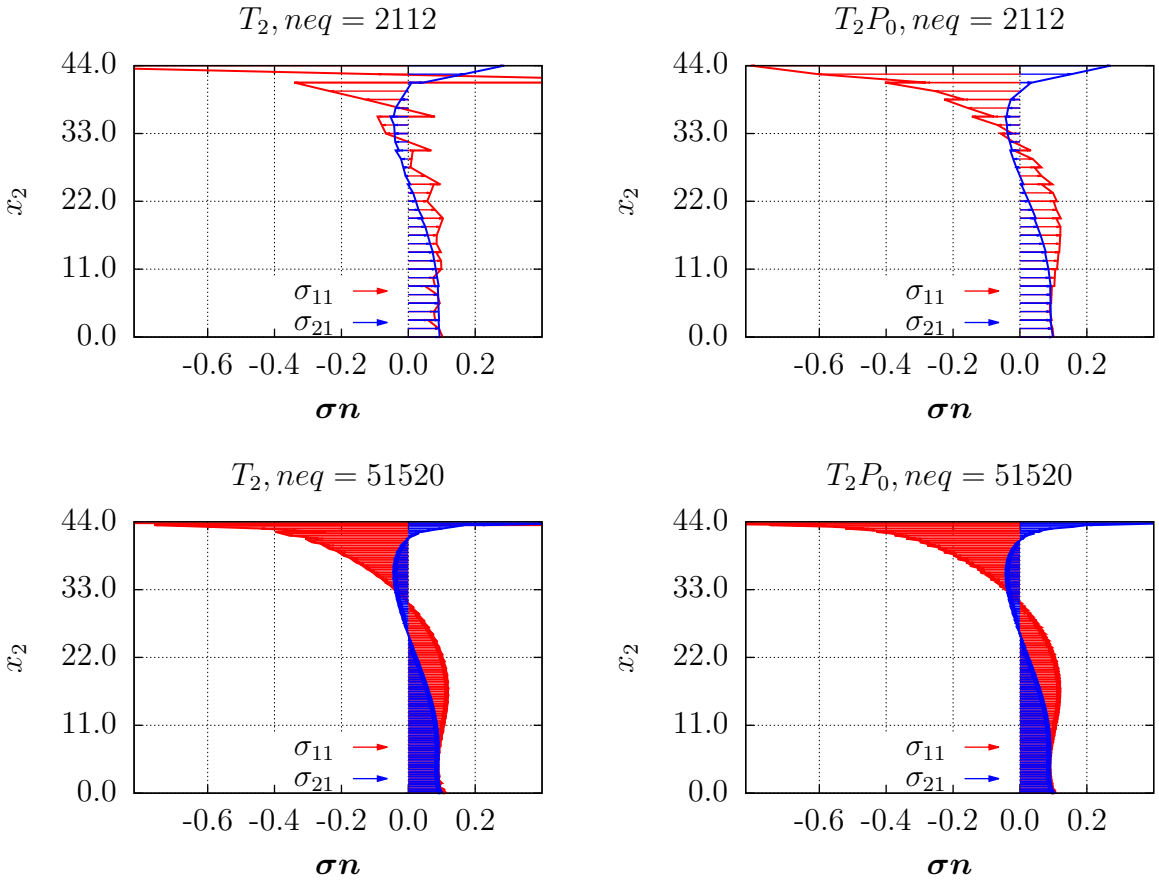

Figure 35: Course of the support reactions for the Galerkin elements T_2 and T_2P_0 under consideration of different system sizes neq .

This is due to the fact, that the stress tensor is not symmetrically constructed. As the balance of moment of momentum gets enforced, the symmetry of the stresses is fullfilled in a stronger sense which has, especially at such sharp corners, an influence on the solution. This effect is different for P_mP_k and RT_mP_k as the boundary conditions are applied in a different way. For RT_mP_k the boundary conditions are directly applied as known values, whereas, due to the nonrectangular domain, the stress boundary conditions for P_mP_k are applied in a "least-squares sense" via a boundary residual $\mathcal{R}_{\partial\mathcal{B}}$, see also Chapter 4.6.

5.4 Quartered plate, convergence of stresses

Since the stresses are physically normal continuous, the approximation in $W^{1,p}(\mathcal{B})$ may lead to problems for example for a body consisting of parts with different material parameters. Therefore, the stress distribution of a quartered plate is considered, where each quarter has a different Young's Modulus, compare also Figure 36 (left). The shear stresses at the boundaries are set to zero and the displacements in direction of the normal of each side are set to one, yielding that the plate is uniformly stretched. For the weighting of the residuals the weights ω_i are chosen as $\omega_1 = 1, \omega_2 = \omega_3 = 1/\mu$. The underlying constitutive relation is of Neo-Hooke type, see Equation (28.1) and the material parameters are chosen as $\nu = 0.35$ and the Young's Moduli $E_i = (100, 200, 300, 400)$.

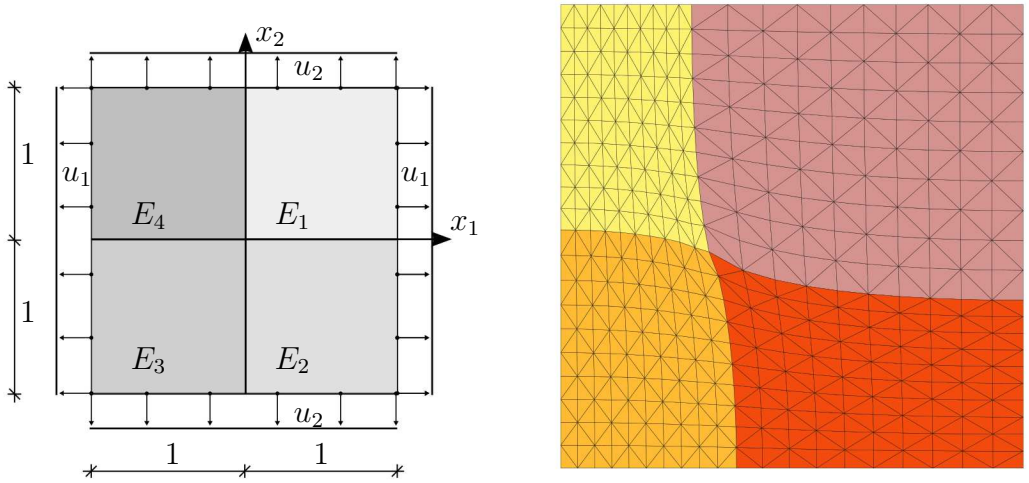

Figure 36: Geometry of the quartered plate (left) and typical mesh on deformed configuration (right), RT_1P_2, 20x20 elements per side.

The distributions of the first Piola-Kirchhoff stress tensor $\boldsymbol{P}$ and the Cauchy stresses $\boldsymbol{\sigma}$ are investigated for different fine meshes. Therefore, the distribution of P_{22} is shown in Figure 37 and the distribution of σ_{22} in Figure 38 for different elements and meshes.

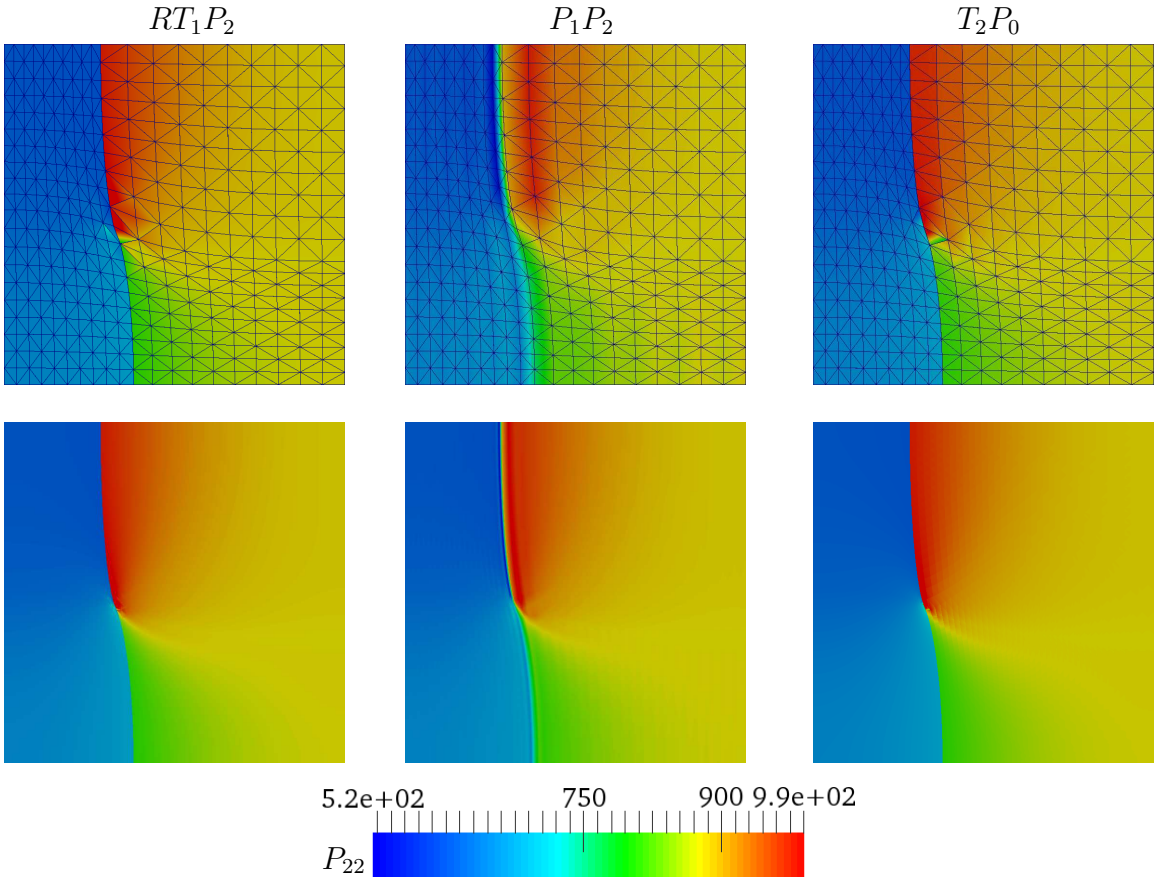

Figure 37: Distribution of the P_{22} stresses for the quartered plate meshed with 20x20 (above) and 80x80 (below) elements.

The plot ranges are the same for each set and are given by the respective legend. For the

coarser mesh the edges of the elements are plotted in Figure 37 (above) to underline the stress approximation in the area of the material transition. The distribution of the shear stress σ_{12} and σ_{21} are depicted in the Appendix, see Chapter A.7.

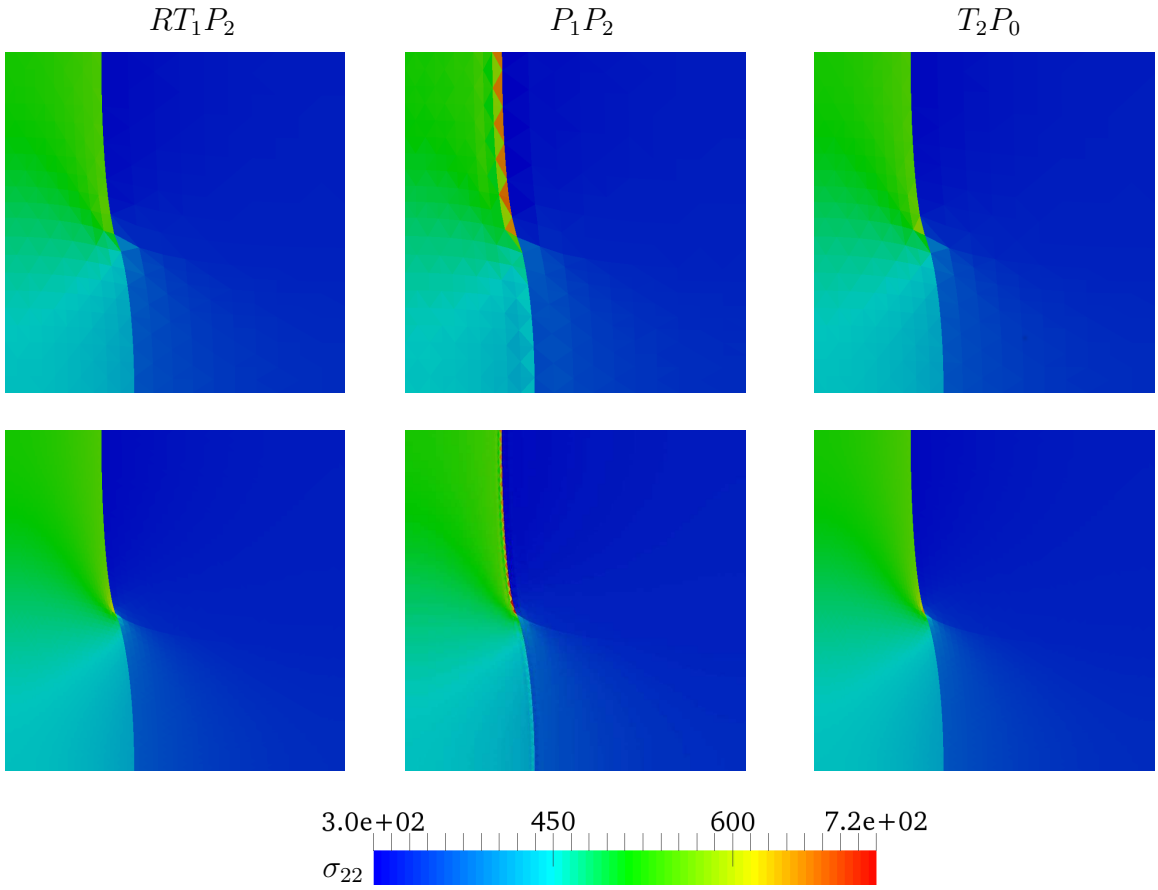

Figure 38: Distribution of the σ_{22} stresses for the quartered plate meshed with 20x20 (above) and 80x80 (below) elements.

The expected (and physically correct) result for the stress distribution of such a boundary value would be that the normal components of the stress tensor (the local traction vector) are continuous, whereas the other components could be discontinuous. That means e.g. for the P_{22} component a continuous course along the horizontal material transition and a probably discontinuous one along the vertical material transition. The figures show, that the stress distribution for RT_1P_2 and T_2P_0 are almost identical. Thus, the interpolation of the stresses in $W^q(\mathrm{div}, \mathcal{B})$ leads to physically correct results for the stress distribution also in the area of the material transition. As the stresses for the T_2P_0 element are by construction discontinuous over element edges the mixed Galerkin formulation is also able to provide a reliable result at the material transition. However, the interpolation of the stresses in $W^{1,p}(\mathcal{B})$ for the element P_1P_2 leads to a different stress distribution, especially in the area of the material transitions. Since all entries of the first Piola-Kirchhoff stress tensor $\boldsymbol{P}$ are degrees of freedom, they are assumed to be continuous. However, this assumption is not physical. The provided least-squares formulation (and the included constitutive relation) aims to solve this arising contradiction at the material transition as good as possible (in a least-square sense). This leads to a smooth crossover of the

P_{22} stresses at the vertical material transition and to an averaged value between both materials. This effect can be seen especially in the upper plot for P_1P_2 in Figure 37 at the material transition (the domain is meshed by 20x20 elements, 10 elements per material). The σ_{22} course in the area of the material transition becomes discontinuous for P_1P_2 (as $\nabla \boldsymbol{u}$ is discontinuous due to the interpolation), but also unphysically high values arise. All stress components, which are on the border, become averaged in a least-squares sense. Thus, the stresses in the region of the material transitions are polluted by this compensating elements. This effect could have a crucial impact e.g. in the case of plasticity, where the actual stresses are used as a local criterion for the occurence of plastic deformation. The results for RT_mP_k and T_2P_0 converge to the same distribution for all stress components. As shown in Figure 73 in the Appendix, the shear stresses for the least-squares elements, however they are not symmetrically interpolated a priori, become symmetric for fine meshes as demanded by the constitutive relation and the additional residual.

Finally it can be said, that the element types show a good performance for different boundary value problems. Nevertheless for the element type P_mP_k problems can arise e.g. in case of material transitions due to the approximation of the stresses in $W^{1,p}(\mathcal{B})$. Therefore, in the following, the computations are restricted to the element type RT_mP_k, as P_mP_k has a major issue. It is remarked, that the following three examples (sections 5.5, 5.6 and 5.7) have already been published in a similar manner in Schröder et al. [2016].

5.5 Compression test, compliance with volume conservation

As a further example a two-dimensional compression test is considered, compare Reese and Wriggers [2000] and see Figure 39.

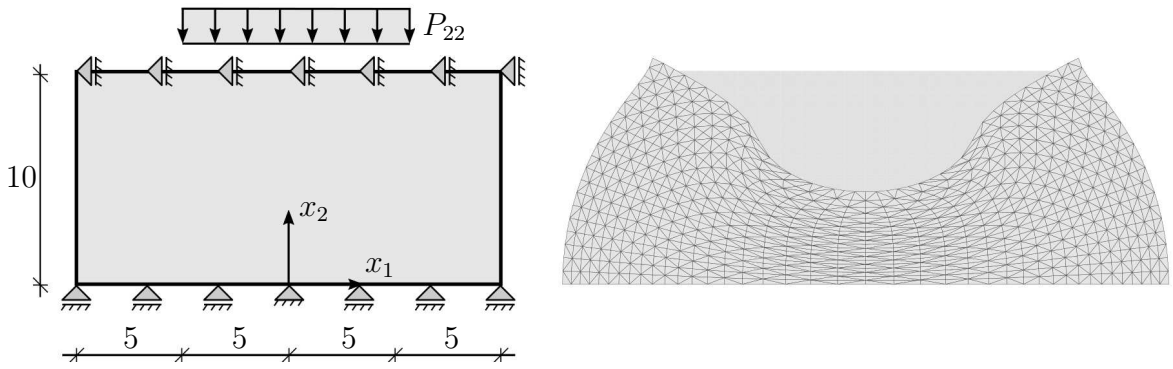

Figure 39: Geometry of the compression test and typical mesh in the deformed configuration for RT_2P_3.

The material is chosen to be nearly incompressible ($E = 240.566$, $\nu = 0.498$) and of Neo-Hookean type, see Equation (28.1). The domain with the dimension 20×10 has a displacement bound in vertical direction for the lower side. The upper side is bounded in horizontal direction. Additionally, the mid-point of the lower side is completely fixed $\boldsymbol{u}(x_1 = 0, x_2 = 0) = (0, 0)^T$. The left and right side of the domain has stress-free boundaries ($\boldsymbol{PN} = (0, 0)^T$), as well as the shear component $P_{12} = 0$ at the lower side. On the upper side the P_{22} stresses are given as $P_{22} = 0$ respectively $P_{22} = -400$. The

weighting factors are chosen as $\omega_1 = 1, \omega_2 = \omega_3 = 1/\mu$. To validate the least-squares formulation, an element of the type RT_2P_3 with $neq = 47999$ is considered. Therefore a structured (and symmetric) mesh with 40×40 triangular elements is chosen to avoid possible influences of mesh anisotropy, as shown in the deformed configuration, as depicetd in Figure 39.

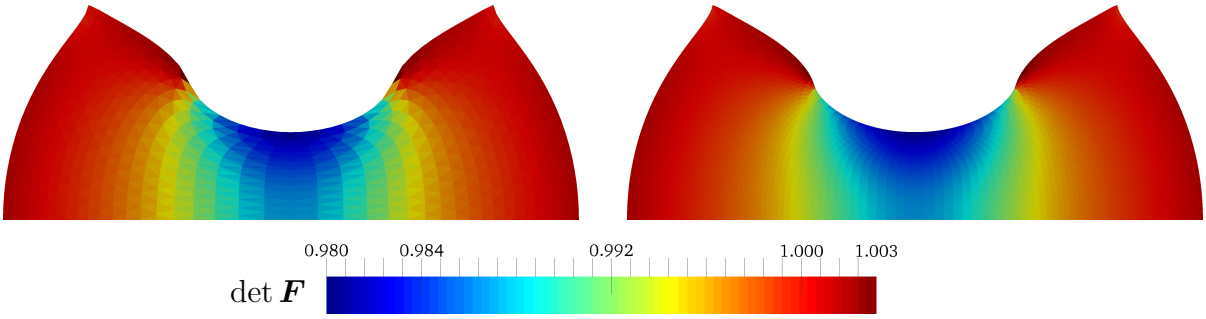

Figure 40: Plot of $\det \boldsymbol{F}$ over the deformed shape of the compression test for the mixed least-squares element RT_2P_3 (left) and the mixed Galerkin element T_2P_0 (right).

For comparison a mixed Galerkin element (T_2P_0, triangular element, quadratic displacement, constant pressure) with $neq = 48620$ is used. Both elements lead to the same solution of $u_2 \approx 5.67$ for the vertical displacement of the upper mid point with the coordinates (0,10). Furthermore, the fulfillment of the incompressibility constraint is checked. Therefore, the distribution of $\det \boldsymbol{F}$, which can be interpreted as the volume dilatation, is plotted over the domain for both elements, see Figure 40. Here, both elements obtain comparable results and show a nearly volume preserving behavior.

5.6 3D plate, displacement convergence and stress distribution

In the following example a three-dimensional plate is investigated. Due to symmetry conditions it is reduced to one fourth of the domain under consideration of symmetry boundary conditions. The reduced geometry is clamped at two sides, see Figure 41.

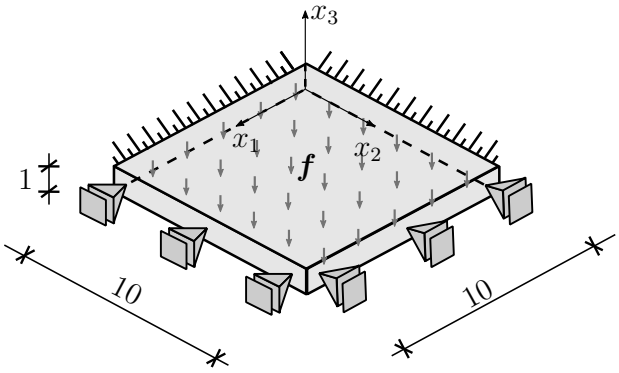

Figure 41: Geometry of the clamped plate.

At the symmetry sides the tangential entries of the local traction vector and the normal displacements are set to zero. The upper and lower faces are stress-free with $\boldsymbol{PN} =$

$(0,0,0)^T$. As a load a body force $\boldsymbol{f} = (0,0,-2)^T$ is applied. The Neo-Hooke material, see Equation (28.1), is assumed to be compressible with the material parameters chosen as $E = 200$ and $\nu = 0.35$. The weighting factors ω_i for the residuals are chosen as $\omega_1 = 1, \omega_2 = \omega_3 = 1/\mu$.

Figure 42 shows a convergence study for the vertical (negative) displacement at the point $(10,10,1)$. Here, the performance of a least-squares element (RT_0P_2) with the a ten-noded standard Galerkin finite element (T_2) is compared. It can be seen, that the provided least-squares element performs well for the given boundary value problem even for a low number of degrees of freedom of the total system of equations.

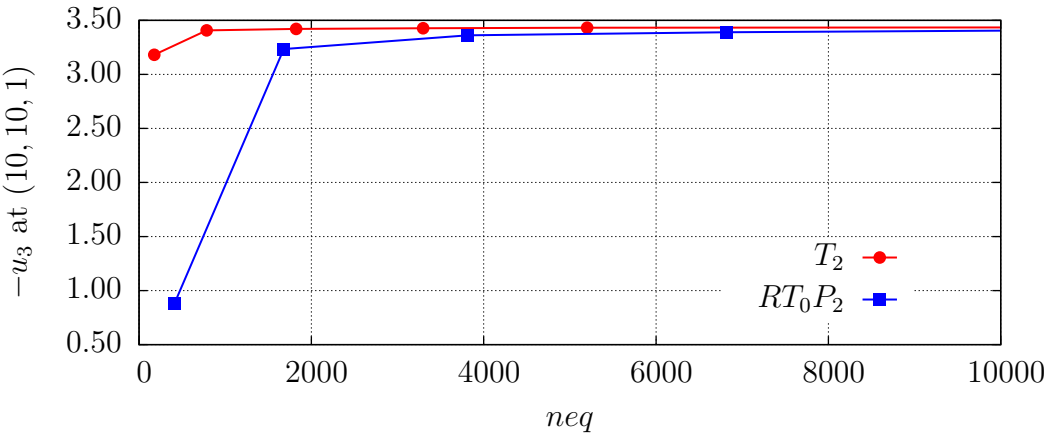

Figure 42: Displacement convergence for u_3 of node $(10,10,1)$ over the number of equations (neq) of the final system of equations for RT_0P_2 and T_2 .

Furthermore, a plot of the P_{11} stresses on the deformed shape of the domain for both elements is provided in Figure 43. Unless the low interpolation order for the stresses, the result for the least-squares element is in line with the solution computed by the Galerkin element.

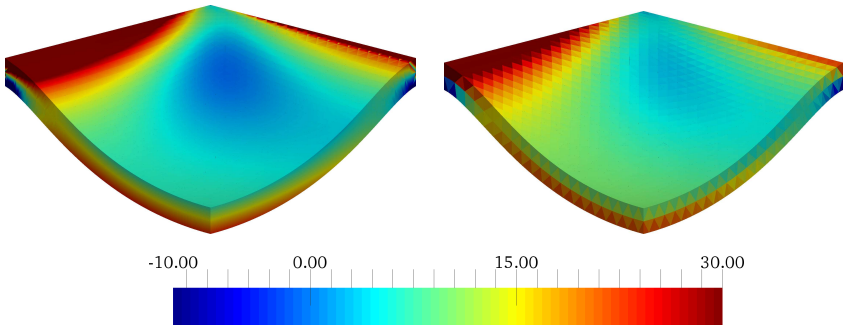

Figure 43: Stress component P_{11} on the deformed shape of the clamped plate under bodyforce for T_2 (left) and RT_0P_2 (right).

5.7 Cantilever beam, influence of transverse isotropy

In this numerical example the influence of a transversely isotropic material behavior on the vertical displacement at the point with the coordinates $(10, 1)$ of the cantilever beam is investigated, see also Figure 44. The underlying isotropic part of is given by a the free energy function of Neo-Hookean type, compare Equation (28.1) and the transverse isotropic part is written in terms of the invariant J_4, see Chapter 2.3.3.

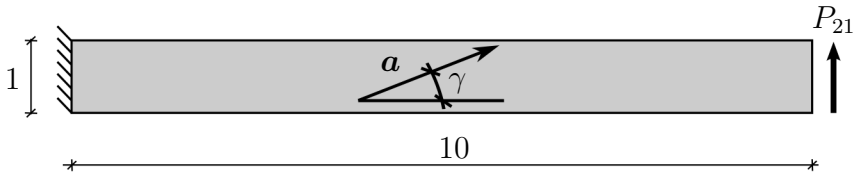

Figure 44: Geometry of the cantilever beam.

Different values for the angle of the preferred direction $0° \leq \gamma \leq 180°$ leading to $\boldsymbol{a} = (\cos[\gamma], \sin[\gamma])^T$ are considered. The domain of consideration has the dimensions 10×1. The left side of the beam has a fixed displacement boundary ($u_1 = u_2 = 0$). The local traction vectors of the upper and lower edges are assumed to be stress-free leading to the essential boundary conditions ($\boldsymbol{PN} = (0, 0)^T$). The system is loaded by a shear-stress on the right side ($\boldsymbol{PN} = (0, 0.1)^T$).

Since a compressible material is considered, a quadratic standard Galerkin element (T_2, $neq = 5440$) is used as a reference solution. For the least-squares mixed finite element formulation the element types RT_1P_2 as well as RT_2P_3 are considered. Due to the outcome of the example in Chapter 5.2, the weights are chosen as $\omega_1 = 1$, $\omega_2 = 1/\mu$ and $\omega_3 = 10/\mu$. The Young's modulus is set to $E = 200$ and the Poisson's ratio to $\nu = 0.35$ ($\lambda = 172.84$ and $\mu = 74.0741$). The material parameters with respect to the transverse isotropy are chosen as $\alpha_1 = 10000$ and $\alpha_2 = 4$.

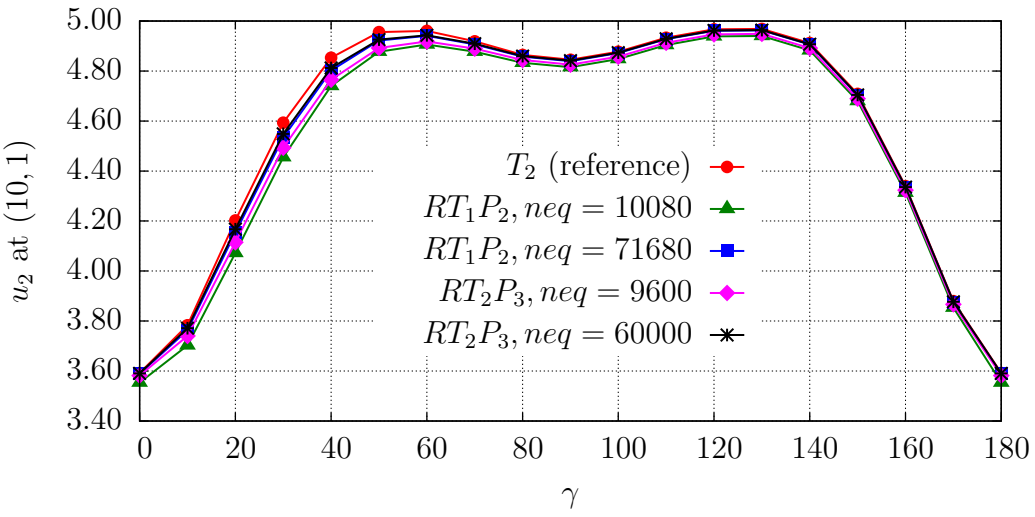

Figure 45: Displacement of the upper right node of the cantilever beam over different angles γ denoting the prefered direction .

Figure 45 shows the vertical displacement of the upper right node of the cantilever beam for different angles of the preferred direction γ. As expected, the results for $\gamma = 0°$ and $\gamma = 180°$ are the same. It can be seen, that both element types (RT_1P_2 and RT_2P_3) almost reach the reference solution. For a comparable number of equations of the final system (stated in the legend), both results are almost the same. It should be remarked, that the proposed formulation shows a great sensitivity with respect to the chosen material parameters (especially the ones for the transverse isotropy). Thus, the application of a transversely isotropic material partially leads to divergence of the numerical scheme. Further investigation with respect to the robustness of the method should be done in future studies, but are not part of the present work.

Preliminary conclusion

The latter examples show the performance of the provided least-squares mixed finite element formulation. Therefore the approximation quality of the displacements and the stresses has been considered. Furthermore, the influence of different scalar weighting parameters ω_i on the quality of the solution has been shown. As an outcome of these examples it can be said, that higher interpolation orders are recommended as well as suitable weights ω_i. The approximation of the stresses in $W^{1,p}(\mathcal{B})$ should not be used in the provided manner, as it could lead to defective values for the stresses e.g. in the case of material transitions. The provided formulation shows a good performance also in the three-dimensional case. The results for a transversely isotropic material are satisfying. At the end of this chapter it can be said, that the provided formulation in combination with the element type RT_mP_k leads to reliable results for the considered boundary value problems. In the following the element formulation will be investigated with respect to locking and their ability to detect bifurcation points adequately. Furthermore, the application of adaptive mesh refinement under usage of the inherent local error estimator will be tested.

6 Locking phenomena

In general the term “locking” is used in the engineering community, if the discrete solution of the finite element formulation is different than the analytical/reference result due to a stiffened numerical approximation of the physical system. The effect of a weak performance of low order elements has been observed firstly e.g. in Veubeke [1965]. First steps to find the root of this effect has been done e.g. by Doherty et al. [1969]. For $h \to 0$ (by mesh refinement) the solution will be reached, but the convergence rate is generally much slower. This effect (numerical defect) is mostly dependent on a parameter (e.g. λ) which has a cruicial impact on the computed solution in that way, that the error to the analytical result raises for a fixed discretization for $\lambda \to \lambda_{\text{crit}}$, with the critical value λ_{crit}. This paramter could be a geometrical parameter (”geometrical“ locking) as e.g. the ratio of length to height leading e.g. to the so-called shear locking, compare e.g. Koschnick [2004]. This effect is mostly restricted to structural elements like beam or shell elements. In the field of finite elements often the occurence of ”material“ locking can be considered, that means, that the numerical defect is dependent on the change of a material parameter. In the field of solid mechanics mainly the locking phenomena is associated with incompressible materials (and the bulk modulus κ respectively the Lamé paramter λ or the Poisson's ration ν) and the so-called volumetric locking or Poisson's locking. In the literature several definitions of locking are given. For further details the work of Koschnick [2004] gives an extensive overview. In the framework of the present thesis, the following definition will be used:
If for a **fixed discretization** (mesh), the (significant) **error of choice** $||\boldsymbol{a}||$ (as e.g. $\|\boldsymbol{u} - \boldsymbol{u}_h\|_{L^2(\mathcal{B})}, \|\boldsymbol{\sigma} - \boldsymbol{\sigma}_h\|_{L^2(\mathcal{B})}, \|\Pi - \Pi_h\|_{L^2(\mathcal{B})}, \mathcal{F}_h ...$) of the approximated solution to the analytical one (respectively an “overkill” solution) is **higher** for a changing parameter λ, we denote this element as **locking**, else as non-locking. Therefore we have to investigate the error (over the whole domain) as well as the change of the convergence rate for $\lambda \to \lambda_{\text{crit}}$ to give a clearer statement about the ”quantity“ of locking behavior of an element formulation. It should be mentioned, that from a mathematical point of view, compare Braess [1997], this effect is nothing else than a more ill-conditioned problem. So it is not surprising, that the influence of the critical parameter can even lead to e.g. divergence of the numerical solution scheme (as e.g. Newton's method) in the case of nonlinear problems.

6.1 Cantilever beam, investigation of locking

For the investigation of volumetric locking, a clamped cantilever beam is considered. The geometrical setup of the boundary value problem is given in Figure 46.

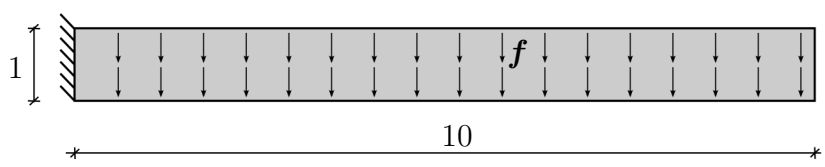

Figure 46: Geometry of the cantilever beam.

The system is loaded by a bodyforce of $\boldsymbol{f} = (0, -0.1)^T$. As seen in Section 5.2, where the performance with respect to different weighting factors has been investigated, a suitable choice for the weighting factors ω_i for this type of boundary value problems is given by $\omega_1 = 1, \omega_2 = 1/\mu$ and $\omega_3 = 10/\mu$. The constitutive relation is defined by the free energy function given in Equation (28.1). As an error the value of the discretized functional $\mathcal{F}_h$, with $\mathcal{F} = 0$ and the computed result F_h and additionally the plot of the u_2-displacement convergence of the upper right node of the cantilever is considered. For the investigation four different element types ($RT_0P_1, RT_1P_2, RT_2P_3$ and RT_3P_4) are used, due to the findings in 5.1. The material parameters used are given by the Lamé parameters $\mu = 100$ and a changing $\lambda_i = \{1\text{E+}01, 1\text{E+}02, 1\text{E+}03, 1\text{E+}04, 1\text{E+}05\}$ respectively Young's Modulus E and Poisson's ratio ν, see Table 5, where the Young's Modulus and the Poisson's ratio are rounded by four respectively five decimal places. So i denotes the amount of incompressibility for the chosen parameter setup. For $i = 1$ the material is fully compressible and with raising i it becomes more and more incompressible.

i	λ	μ	E	ν
1	1E+01	100	209.0909	0.04545
2	1E+02	100	250.0000	0.25000
3	1E+03	100	290.9091	0.45455
4	1E+04	100	299.0099	0.49505
5	1E+05	100	299.9001	0.49950

Table 5: Material parameters used for the investigation of locking.

In the figures 47, 48, 49 and 50 the results of the computations are shown for each element type.

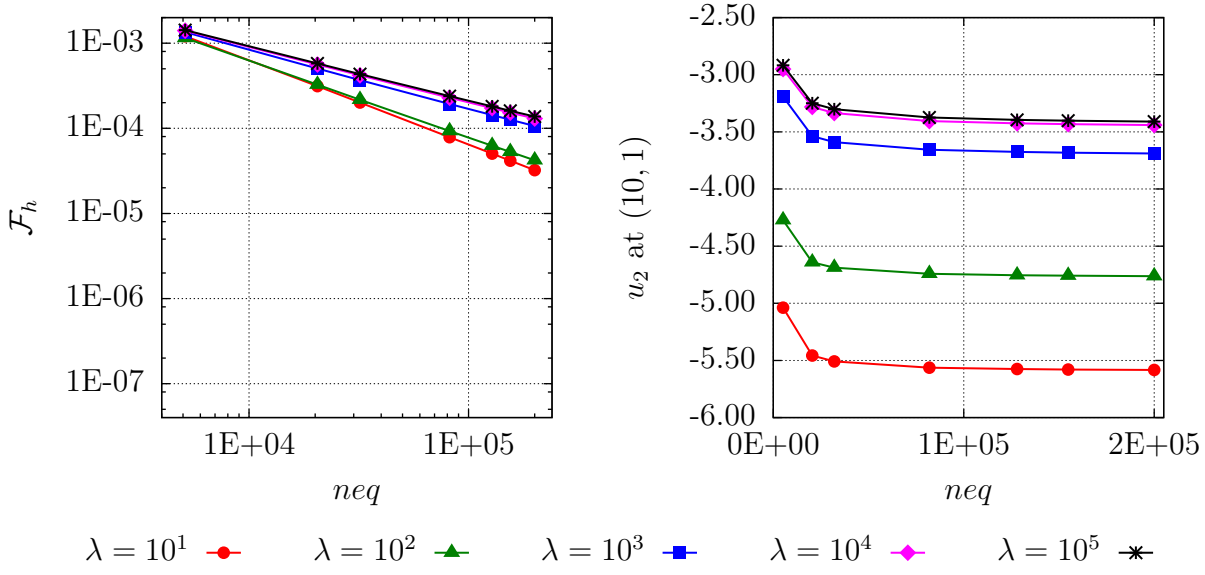

Figure 47: Log-log plot of $\mathcal{F}_h$ (left) and u_2-displacement of the upper right node (right) for RT_0P_1.

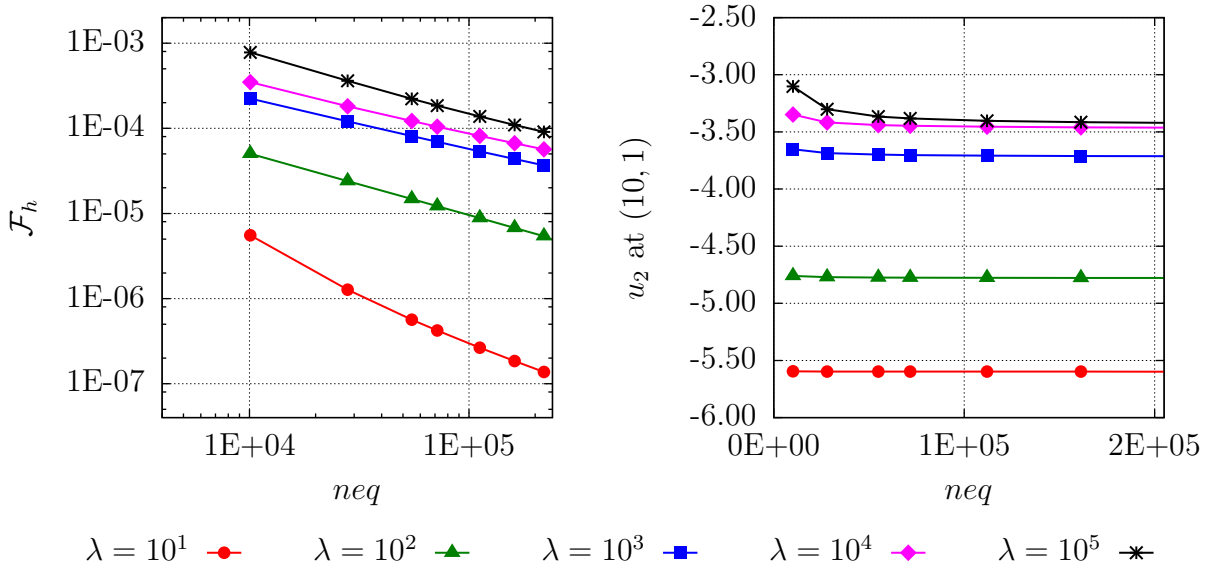

Figure 48: Log-log plot of $\mathcal{F}_h$ (left) and u_2-displacement of the upper right node (right) for RT_1P_2.

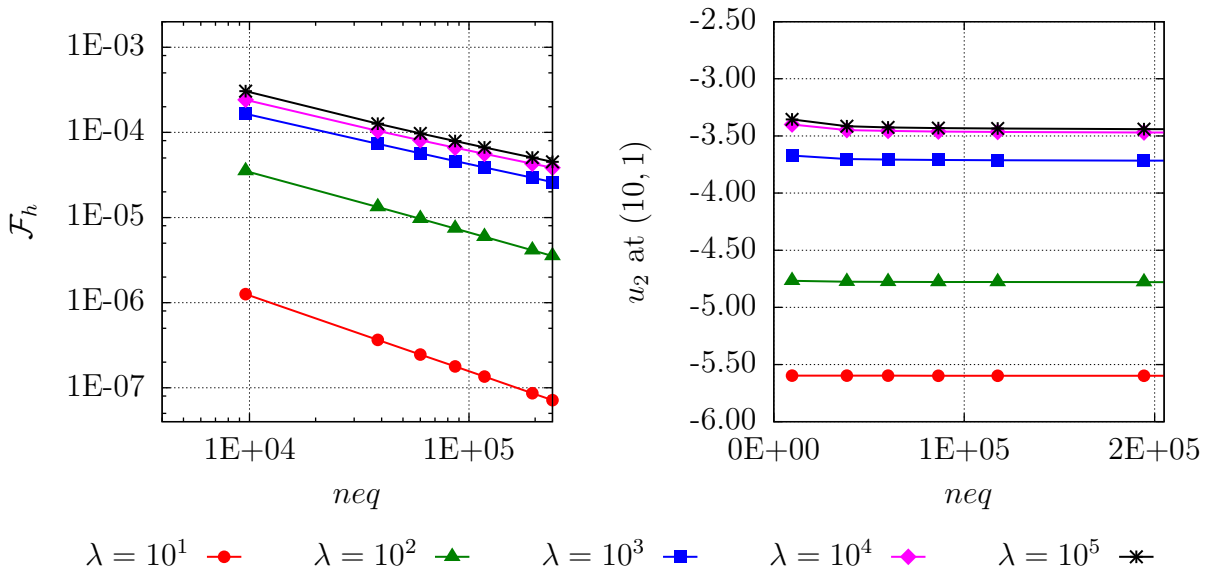

Figure 49: Log-log plot of $\mathcal{F}_h$ (left) and u_2-displacement of the upper right node (right) for RT_2P_3.

On the left plots it can be seen clearly, that the error of the functional raises with a raising Lamé parameter λ. For a better classification of the least-squares results, also the behavior of a quadratic standard Galerkin element is shown, see Figure 51. Here the convergence of the tip displacement of the cantilever beam is shown over the number of equations of the global system (right) as well as the error $|u - u_h|$ of the tip displacement with respect to an "overkill" solution (left). Both axis in the left chart are plotted logarithmically and confirm the statement given e.g. in Braess [1997] that standard polynomial elements are influenced by raising incompressibility.

Furthermore, the convergence rate, which is the (negative) slope of course in the log-log

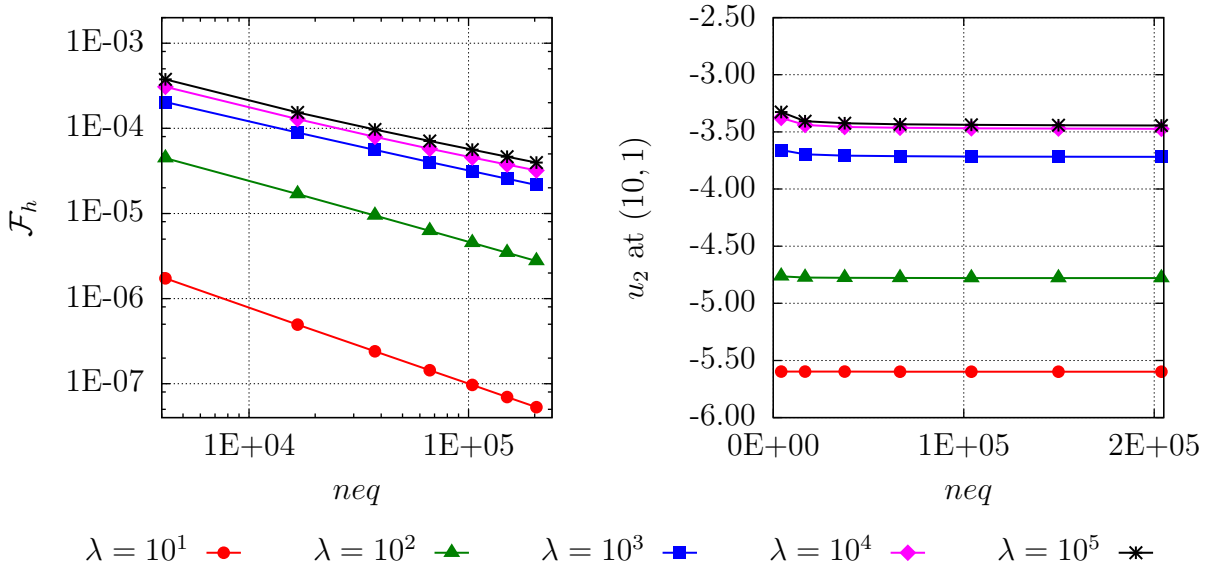

Figure 50: Log-log plot of $\mathcal{F}_h$ (left) and u_2-displacement of the upper right node (right) for RT_3P_4.

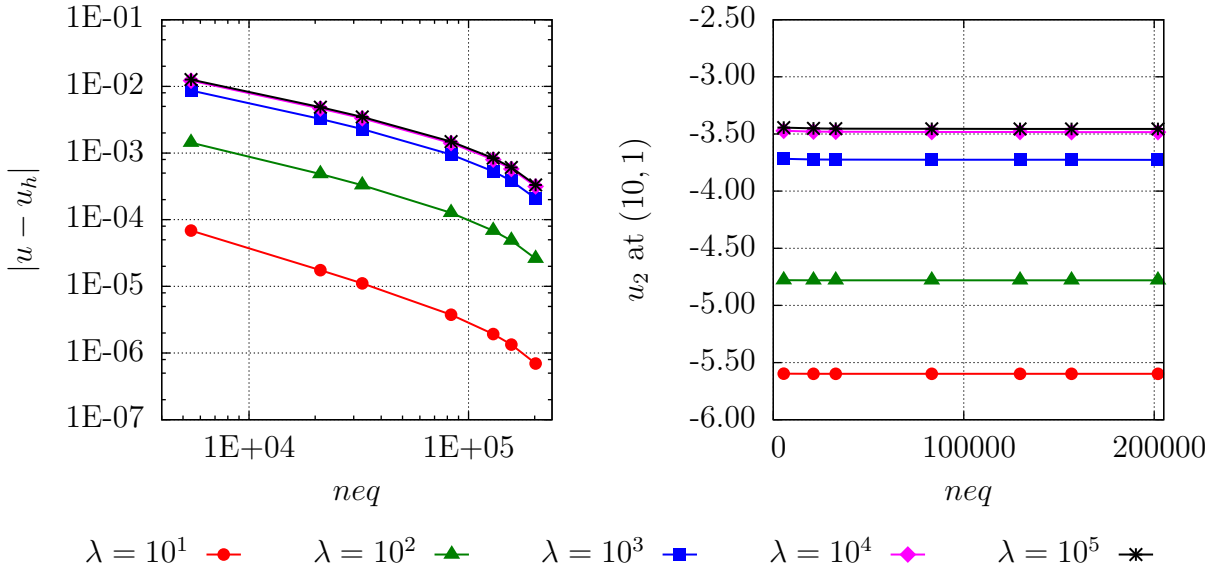

Figure 51: Log-log plot of $|u - u_h|$ (left) and u_2-displacement of the upper right node (right) for T_2.

plot (both the vertical and horizontal axes of a plot are scaled logarithmically) becomes smaller for a raising value of λ for all elements, compare Table 6. The reasons for such "worse" convergence rates for the higher order elements can be found in the regular mesh refinement and the boundary value problem under consideration, which is not regular. Here especially the corners of the domain at the clamped edge have a cruicial influence on the perfomance. To obtain better (and more expected) results, an adaptive mesh refinement strategy should be used, see also Chapter 7. With this findings we can state, that the provided formulation shows a clear locking behavior with regard to a raising value λ. It should be remarked that the quantitative error for the least-squares element could

not be the only indicator for locking (if the functional is considered as a measurement), as a residual weighting somehow by the material parameter λ could weight this effect out of the functional. However, the loss of convergence rate can be seen as a suitable indicator for locking. But, even though the volumetric locking affects the performance of the element with respect to the convergence rate, the stresses for incompressible materials can be computed correctly, see Chapter 5.3.

	$\lambda = 1E{+}01$	$\lambda = 1E{+}02$	$\lambda = 1E{+}03$	$\lambda = 1E{+}04$	$\lambda = 1E{+}05$
RT_0P_1	0.987904	0.902647	0.692433	0.648714	0.638107
RT_1P_2	1.20023	0.72352	0.585584	0.590412	0.698056
RT_2P_3	0.890968	0.713384	0.573722	0.569928	0.593107
RT_3P_4	0.896124	0.714259	0.57671	0.581379	0.577794
T_2	1.28177	1.10451	1.03031	1.00963	1.00652

Table 6: Convergence rates of the elements used for different values of λ.

The computations are restricted here up to $\lambda_5 = 1E{+}05$. Further raising of the parameter λ e.g. to $\lambda = 1E{+}06$ leads to divergence of the numerical scheme (in this case Newton's method). However, the incompressibility constraint is already fulfilled with the chosen values for λ, see Table 7, where the deviation from 1 becomes already very small for $i = 4$. Here, the minimum and maximum values of the determinant of the deformation gradient $\det \boldsymbol{F}$ (the change of volume) are given exemplary for the RT_1P_2 element, computed with $neq = 28000$ for $i = 1..5$.

i	λ	$Min[\det \boldsymbol{F}]$	$Max[\det \boldsymbol{F}]$
1	1E+01	0.888923	1.12198
2	1E+02	0.925533	1.07378
3	1E+03	0.987937	1.01171
4	1E+04	0.998886	1.0011
5	1E+05	0.999916	1.00008

Table 7: Minimum and maximum values of $\det \boldsymbol{F}$ for different values of λ using an RT_1P_2 element with $neq = 28000$.

7 Adaptive mesh refinement

To compute reliable results using finite elements, a suitable mesh has to be chosen. A common approach is the computation of the result for different meshes and the preparation of a convergence study. The convergence of a variable of choice (e.g. a displacement value at a certain point) can then be determined, if the change of the value becomes small (enough) for raising system sizes. In the framework of mesh refinement in general regular refinement strategies are predominant (regular h-refinement). Regular refinement means, that for each computation of the convergence study the mesh is globally refined, see exemplary Figure 52. Unfortunately this approach can be time consuming and the

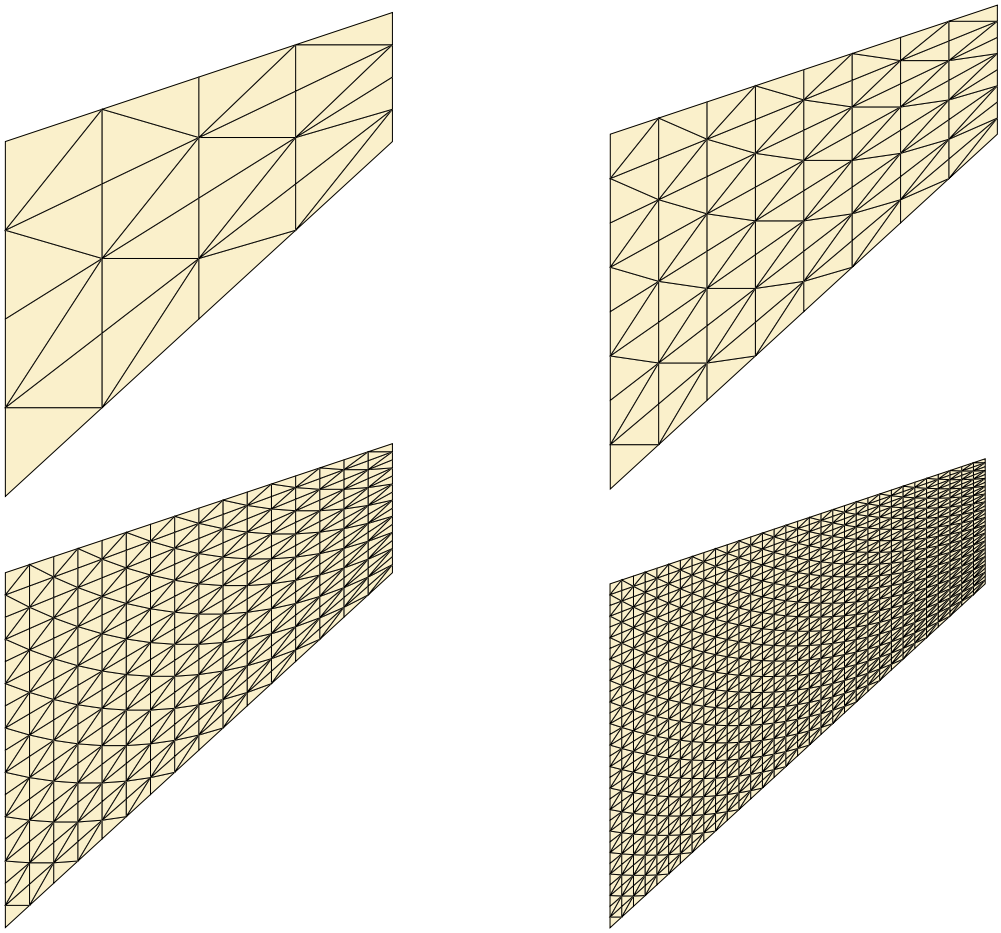

Figure 52: Exemplary regular mesh refinement for the Cook's Membrane problem with $4, 8, 16$ and 32 elements per edge.

memory requirement could be high, especially if the problem is not regular due to e.g. local singularities. These points can have a major influence on the overall accuracy, compare e.g. Verfürth [1994]. An alternative way is an adaptive mesh refinement strategy (adaptive h-refinement). Here the refinement is not done globally but locally at specific spots of the domain. Therefore, starting from a basic disretization, the next refinement level of the mesh (and the spots where the mesh will be refined) results out of the evaluation of a suitable (a posteriori) error indicator, a marking strategy and an appropriate refinement strategy, see Figure 53. For Galerkin based finite element methods, several error estimators exist, see e.g. Zienkiewicz and Zhu [1991]. A major advantage of the least-squares finite element method is, as already mentioned before, that the element-wise

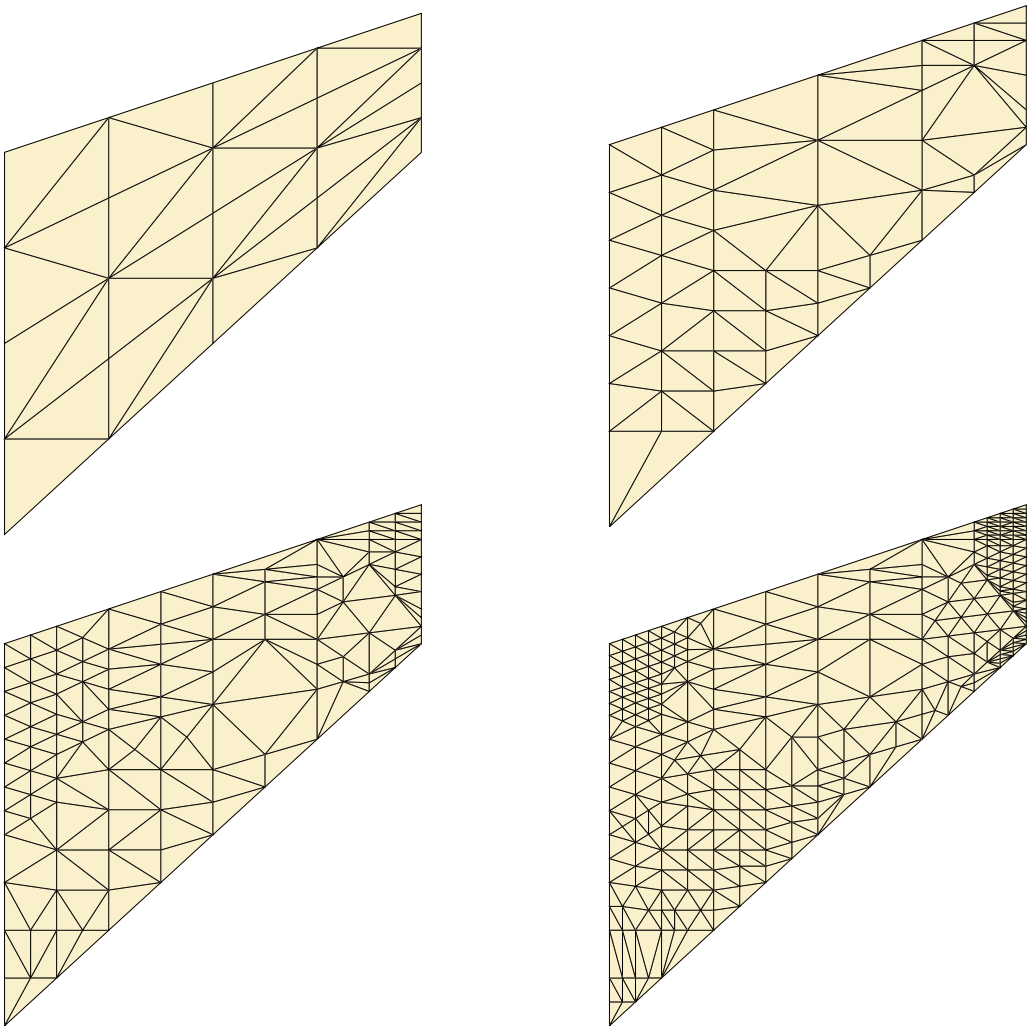

Figure 53: Exemplary adaptive mesh refinement for the Cook's Membrane problem.

evaluation of the least-squares functional can be used as a local error indicator, compare, for instance, Cai and Starke [2004] and Bochev and Gunzburger [2009]. This attractive feature offers the possibility to improve the performance of the method (almost) without any additional costs and achieve reliable results with regard to a specified accuracy with a reasonable expense.

7.1 Marking strategies

The evaluation of the error indicator leads to a local error η^e for each element e of the actual discretization of the domain $\mathcal{B}_h$, containing n triangular elements. The following "marking strategy" selects the elements which have to be refined and form a subset $\mathcal{S}_h \subseteq \mathcal{B}_h$. In the framework of this thesis we compare two different approaches, a **"Element percent marking strategy"** (abbreviated by arE) and an **"Error percent marking strategies"** (abbreviated by arD) in line with Dörfler [1996]. Further marking strategies are e.g. given in Babuška and Rheinboldt [1978], Jarausch [1986] and Johnson [1990].

7.1.1 Element percent marking strategy (arE) The local element error η^e is an outcome of the actual computation. The total error η is then defined as

$$\eta = \sum_{e=1}^{n} \eta^e. \tag{127}$$

It should be remarked that, due to the least-squares functional, all local errors η^e are positive. The amount of marked elements is given by the percentage θ with $\theta = 0\% \Rightarrow \mathcal{S}_h = \emptyset$ and $\theta = 100\% \Rightarrow \mathcal{S}_h = \mathcal{B}_h$. We obtain the size of the subset $\mathcal{S}_h$ as

$$|\mathcal{S}_h|_{\mathcal{C}} = \theta n, \tag{128}$$

containing the θ of the elements with the largest local error indicator.

7.1.2 Error percent marking strategy (arD) In Dörfler [1996] a different marking strategy is proposed. Here, the total error is defined as

$$\eta = \sqrt{\sum_{e=1}^{n} \eta^{e2}}. \tag{129}$$

Now we seek the smallest subset $\mathcal{S}_h \subseteq \mathcal{B}_h$ fulfilling the inequality

$$\eta^{\mathcal{S}_h} = \sqrt{\sum_{e=1}^{n^{\mathcal{S}_h}} \eta^{e2}} \leq \theta\eta = \theta\sqrt{\sum_{e=1}^{n} \eta^{e2}} \tag{130}$$

where $\eta^{\mathcal{S}_h}$ denotes the total error of the subset and $n^{\mathcal{S}_h}$ the number of elements in $\mathcal{S}_h$. Therefore, the errors in η has to be ordered from large to small (the first value in $\eta^{\mathcal{S}_h}$ is the maximum value of η^e. Thus we can conclude, that the marking strategy of Dörfler [1996] marks a percentage of θ of the total error (which is defined as the square root of the sum of the local errors). Beside the strategy, in Dörfler [1996] an efficient algorithm for the implementation of this marking strategy is given without sorting the element errors. However, for simplification, for the computation of the following results a less effecient implementation is chosen. Again, $\theta = 0\% \Rightarrow \mathcal{S}_h = \emptyset$ and $\theta = 100\% \Rightarrow \mathcal{S}_h = \mathcal{B}_h$.

7.2 Refinement strategies

The marked elements can now be refined using a mesh refinement strategy. For a detailed investigation of several mesh refinement strategies the reader is referred to Mitchell [1989] and the references therein. In the framework of this thesis, we restrict ourself on a simple refinement strategy for linear three-noded triangles due to the fact, that we discretize our geometry basically with straight-edged triangles. For refinement we add additional nodes on the marked elements. Based on the "new" nodes (the current and the added ones) we apply a Delaunay triangulation, compare Delaunay [1934] (we use the DelaunayMesh

command of Mathematica), which ensures maximal interior angles. For our example we add three new nodes on each mid point of the edges of the marked elements. Another possible strategy is e.g. to add in total seven additional nodes per marked element, six on the third points of each edge and one in the middle of the element, see also Figure 54.

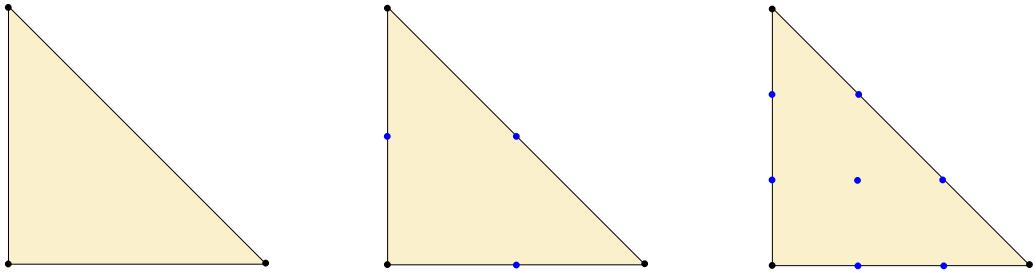

Figure 54: Basis nodes and new nodes for three respectiveley seven additional nodes refinement strategy.

7.3 Plate with a hole, investigation of adaptive mesh refinenemt

In Section 6 the influence of a changing material parameter to our provided formulation has been investigated. Therefore, in Section 6.1 the example of a cantilever beam with an applied body force has been considered. Inter alia the convergence rates of the different element types have been regarded, which shows a relatively poor performance especially for the higher order elements. In the following it will be shown, that the least-squares functional is a suitable error indicator and that the implemented adaptive mesh refinement improves the performance of the method. For comparison to regular refinement the boundary value problem of a plate with a hole is investigated. The side length of the quadratic plate is 20 and the radius of the hole is 1. Due to the symmetry of the problem and for simplification purposes a quarter of the problem is considered, see Figure 55.

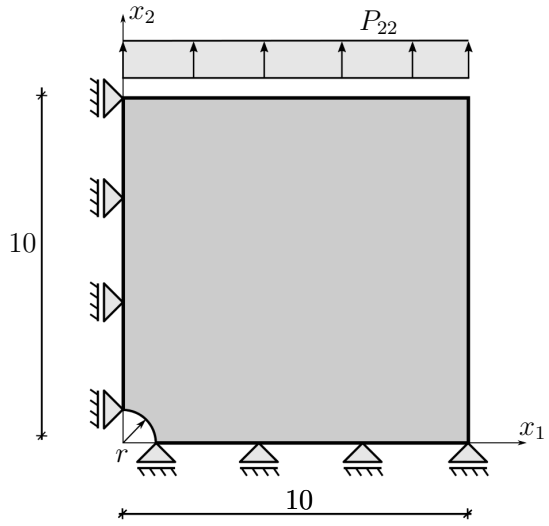

Figure 55: Geometry and boundary conditions of the plate with a hole.

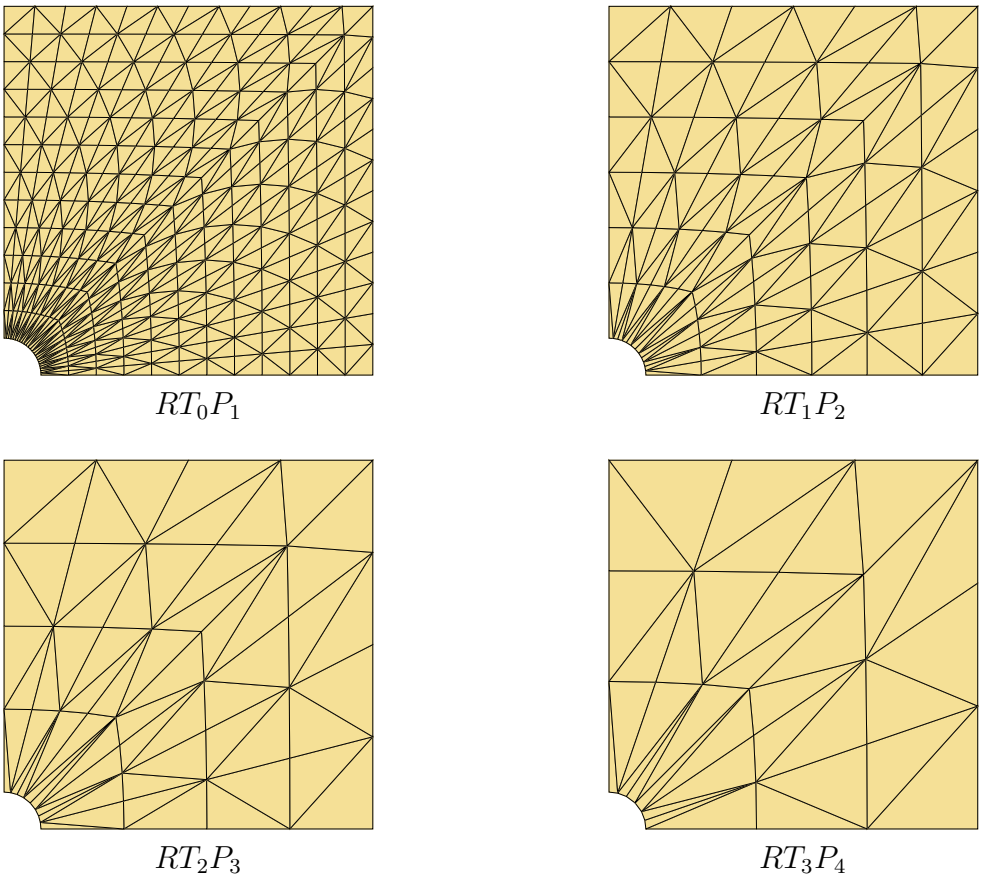

Figure 56: Initial meshes with nearly same system size.

For the displacement field the essential boundary condition $u_2 = 0$ for $x_2 = 0$ and $u_1 = 0$ for $x_1 = 0$ are applied. The essential boundary condition for the stresses are given as zero traction on the right hand side of the domain ($\boldsymbol{PN} = \boldsymbol{T} = (P_{11}, P_{21})^T = \boldsymbol{0}$) and on the upper side $\boldsymbol{PN} = \boldsymbol{T} = (P_{12}, P_{22})^T = (0, 80)^T$. At the symmetry sides for $x_1 = 0$ $P_{21} = 0$ and for $x_2 = 0$ $P_{12} = 0$ is applied. As material parameters for the Neo-Hooke material, see Equation (28.1), $\lambda = 172.84$ and $\mu = 74.0741$ ($E = 200, \nu = 0.35$) are chosen. Four different element types are considered with $\omega_1 = 1, \omega_2 = \omega_3 = 1/\mu$ and as initial meshes different discretizations with n elements over each side are chosen, see Figure 56, leading nearly to the same system size see Table 8. For comparison the result for a regular refinement (abbreviated by rr) is computed. Therefore, the initial meshes is regularly refined by raising the number of elements per side n.

element type	RT_0P_1	RT_1P_2	RT_2P_3	RT_3P_4
n	12	6	4	3
neq	2304	2016	1920	1872

Table 8: Number of eqution of the initial meshes for the different element types.

In the following the performance of both marking strategies are investigated and compared to each other and to the regular refinement. As percentages for the marking strategies $\theta = 90\%$ for the error percent strategy of Dörfler [1996] (arD) and $\theta = 12\%$ for the

element percent strategy (arE) are chosen. For both strategies eight results are computed (that means seven refinement steps are applied). Exemplarily in Figure 57 the resulting meshes for several regular refinement steps and for the adaptive strategies for every second refinement step for the element type RT_1P_2 under consideration of the number of equations (neq) are shown.

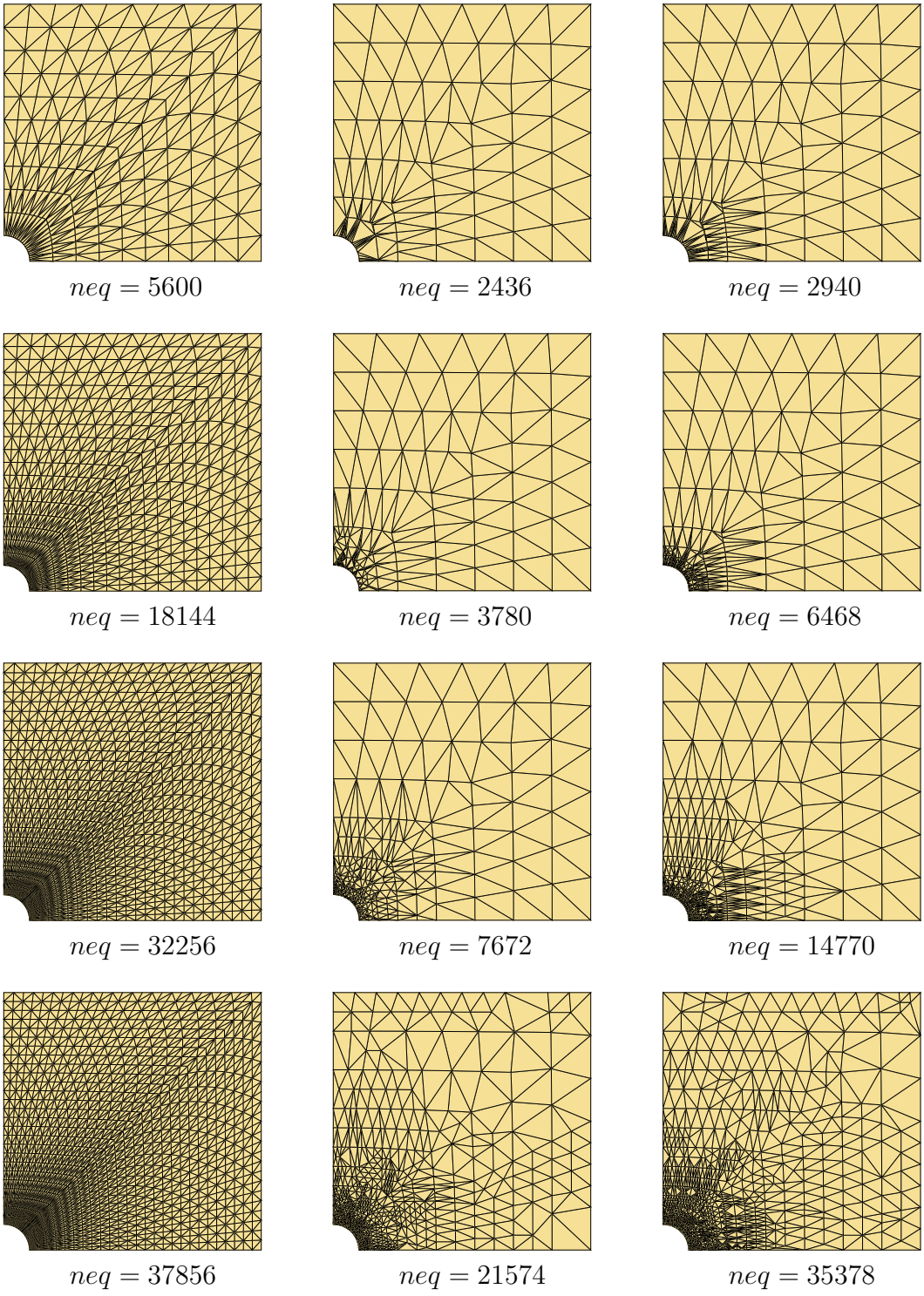

Figure 57: Refinement stages for regular refinemnt (rr, left), error percent marking (arD, middle) and element percent marking (arE, right).

In Figure 58 the results for a regular refinement strategy (rr) as well as the error percent strategy (arD) are shown. Figure 59 shows the results for a regular refinement strategy (rr) and the element error marking strategy (arE). The comparision of both adaptive strategies (arD and arE) are depicted in Figure 60. Evaluating the slope results in different convergence rates, see Table 9.

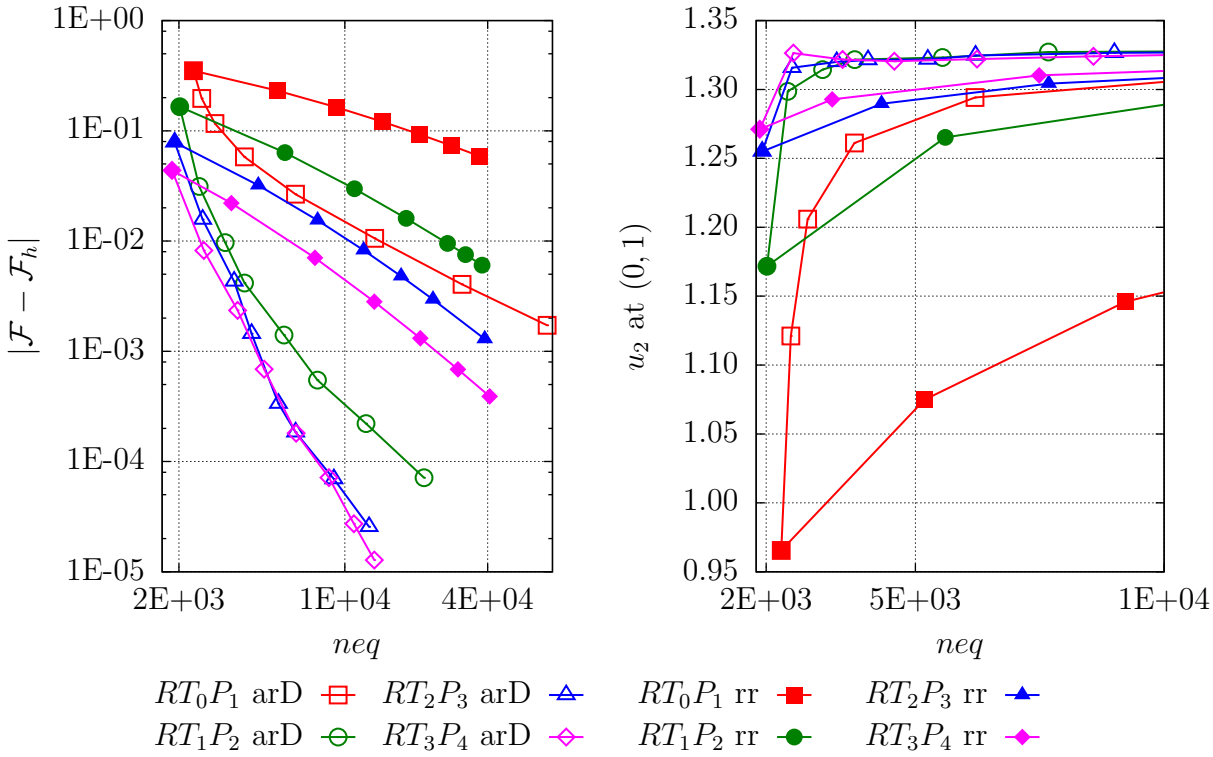

Figure 58: Regular and error percent marking strategy: Log-log plot of $|\mathcal{F} - \mathcal{F}_h|$ (left) and u_2-displacement of the circle node ($x_1 = 0$, $x_2 = 1$) (right).

	regular	adaptive (arD)	adaptive (arE)
RT_0P_1	0.803067	1.038794	1.146551
RT_1P_2	1.374577	2.013812	2.230455
RT_2P_3	1.647342	2.923071	2.941073
RT_3P_4	1.837593	3.832485	3.121928

Table 9: Convergence rates of the elements used for regular and adaptive refinement.

It becomes viewable, that the adaptive mesh refinement cruicially influences the performance of the different element types. The first computed result is equal for all computations due to the fact that we use the same initial mesh. All computations lead to converging results, but the convergence of the regular mesh refinement is much slower than of the adaptive ones. Comparing the adaptive strategies, both marking strategies show a good performance. Considering the convergence rates, the error percent marking strategy of Dörfler [1996] seems to be a little bit stronger for the chosen θ, especially for the higher order elements.

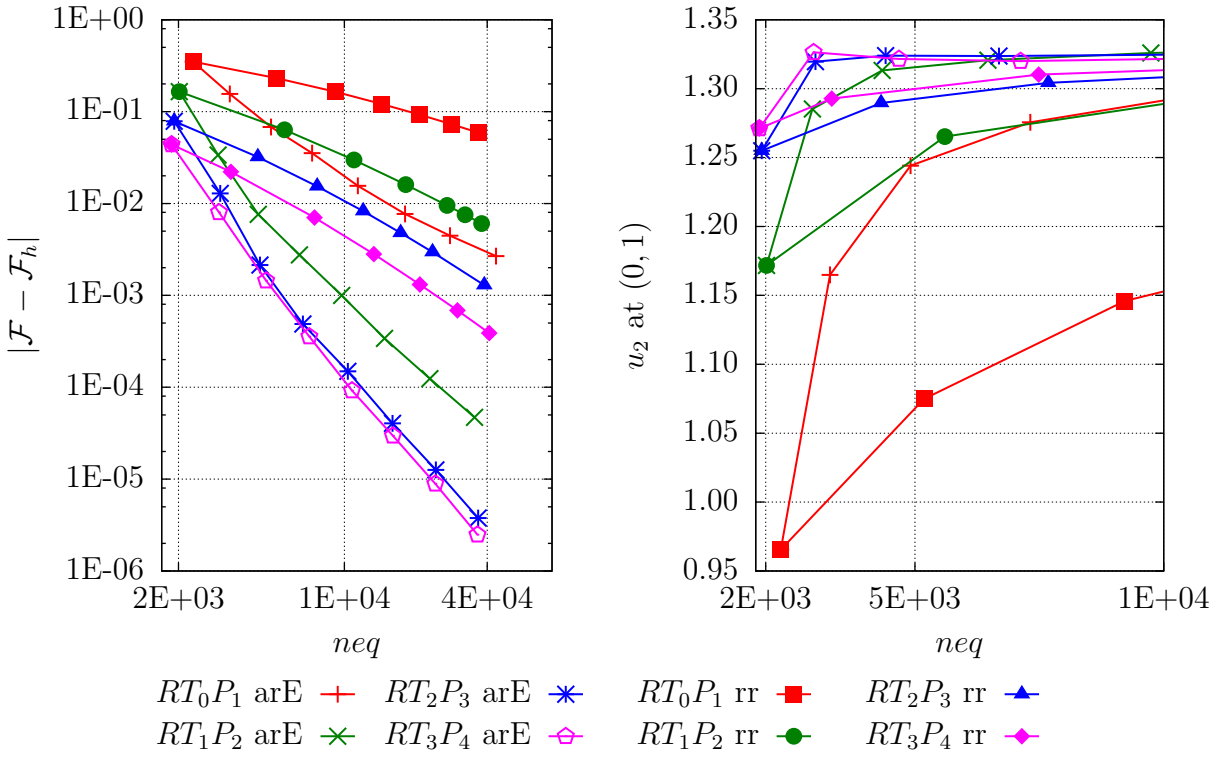

Figure 59: Regular and element percent marking strategy: Log-log plot of $|\mathcal{F} - \mathcal{F}_h|$ (left) and u_2-displacement of the circle node $(x_1 = 0, x_2 = 1)$ (right).

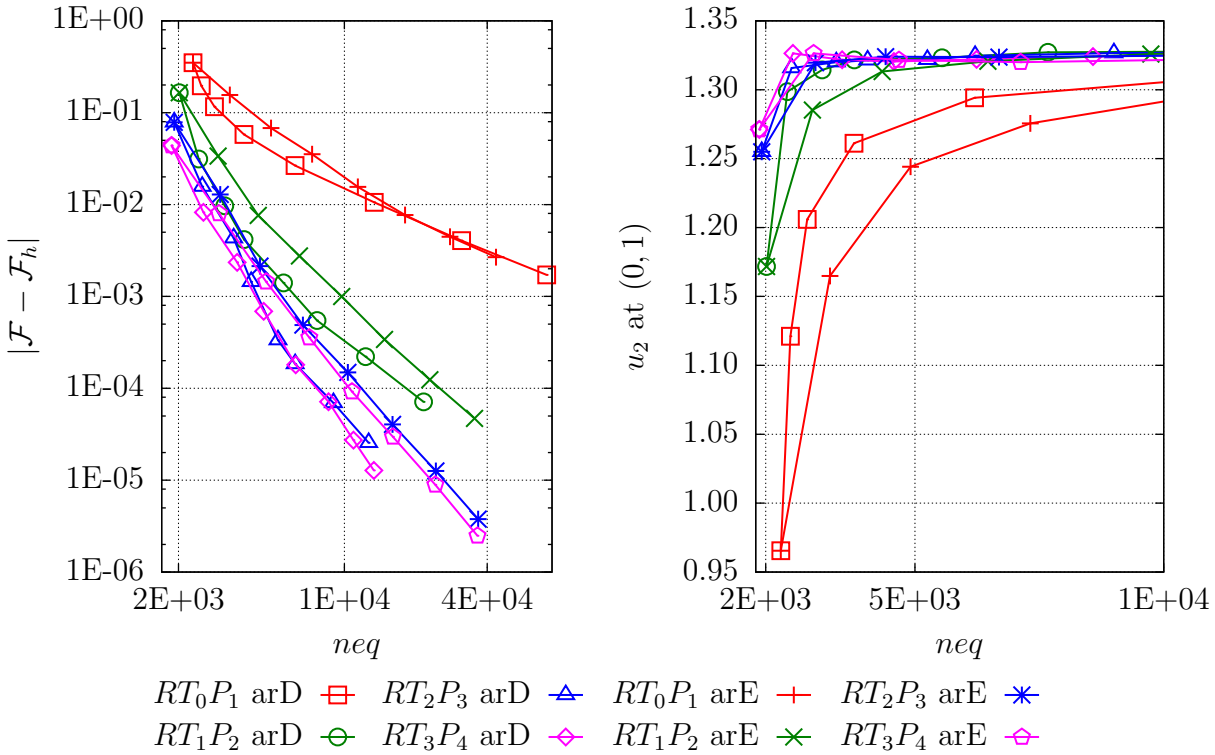

Figure 60: Error percent and element percent marking strategy: Log-log plot of $|\mathcal{F} - \mathcal{F}_h|$ (left) and u_2-displacement of the circle node $(x_1 = 0, x_2 = 1)$ (right).

As already shown e.g. in Cai and Starke [2004] and Bochev and Gunzburger [2009], the least-squares functional is a suitable error indicator. Due to the fact that this tool can be used nearly without any additional computations and costs, it is a strong benefit of the method.
Furthermore the stress distribution is shown exemplary for a RT_3P_4. Therefore, in Figure 61 the von Mises stresses $\boldsymbol{\sigma}_v$ over the deformed shape are depicted for several refinement levels of the error percentage strategy (arD). Here, the converging stress distribution and the expected stress peak at the circular hole can be seen.

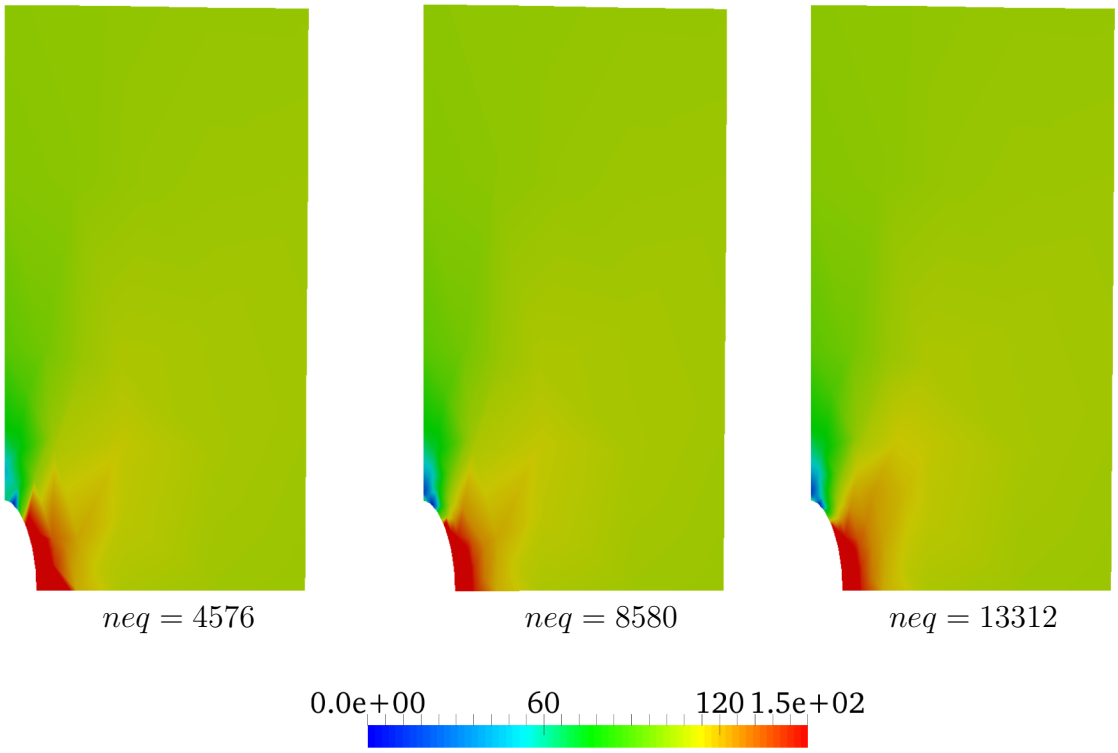

Figure 61: Von Mises stresses over the deformed shape for several refinement levels.

8 Bifurcation analysis

As already seen, the hyperelastic material laws, as e.g. Neo-Hooke result in a nonlinear stress-strain relation respectively a nonlinear (and steady) load-deflection curve. Beside that, physical phenomena as e.g. buckling can occur and have a crucial impact on the stability of the structure. These points where the load (the critical load factor γ_{crit}) causes such a behavior are called instability or bifurcation points. Here, the load-deflection curve leaves its normal (and stable) path, see also Figure 62. Due to the loss of stability of the

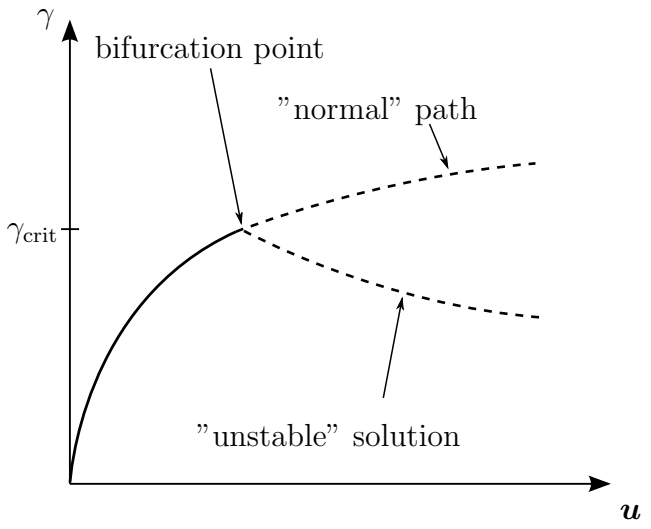

Figure 62: Load-deflection curve with bifurcation point at γ_{crit}.

structure caused by this critical loads and the possible failure of the structure, the used finite elements should be able to provide a reliable and accurate analysis of this bifurcation points. Therefore, a stability analysis of the system has to be done for each equilibrium state to determine a possible bifurcation point. For a detailed investigation of several types of stability problems in the field of elastostatics the reader is referred to Pflüger [1975] and the references therein. In general, in the field of standard Galerkin finite element methods, a simple possibility to detect such points is the investigation of the diagonal elements D_{ii} of the stiffness matrix $\boldsymbol{K}$ with

$$\boldsymbol{K} = \boldsymbol{L}\boldsymbol{D}\boldsymbol{L}^T, \tag{131}$$

where $\boldsymbol{D}$ denotes the diagonal matrix and $\boldsymbol{L}$ a unit lower triangular matrix (with the diagonal entries equal to 1). Consequently L^T denotes a unit upper triangular matrix. An efficient algorithm for the computation is the Cholesky decomposition, see a standard textbook as e.g. Nash [1990]. By examining the diagonal entries with respect to their sign, a statement can be done with respect to the state of equilibrium of the system, compare also Wriggers [2001]. Another way is the evaluation of the eigenvalue problem

$$(\boldsymbol{K} - \omega\mathbf{1})\boldsymbol{\phi} = \mathbf{0}. \tag{132}$$

Here, the instability points are characterized by the first negative eigenvalue ($\omega < 0$), compare e.g. Auricchio et al. [2005; 2010] and Auricchio et al. [2013], where e.g. several mixed finite element formulations are tested with respect to their ability to give an accurate analysis of this bifurcation points. The authors found, inter alia, out, that

> "... all the considered mixed finite element schemes" [MINI, QME, $\mathcal{P}_1 - \text{iso} - \mathcal{P}_2/\mathcal{P}_0$]
> "completely fail in reproducing the stability range of the continuum problem, despite their small strain counterparts are absolutely reliable" (Auricchio et al. [2010]).

For the investigation of such stability points while using the least-squares method, also the evaluation of the eigenvalue problem is a suitable technique. However, due to the quadratic functional and the resulting positive definite matrices, the indicator is different in contrast to the Galerkin method. Here, the smallest eigenvalue (the local minimum of the course of the eigenvalues) is the indicator for a bifurcation point, compare also Müller et al. [2014]. In the following the provided formulation is used to compute bifurcation points. Therefore, several numerical examples are considered. The first example are the classical basis Euler buckling cases and the second example is in line with Auricchio et al. [2010] and Auricchio et al. [2013].

8.1 Euler buckling cases

The basis for the first example are two of the classical basic Euler buckling cases, compare Euler [1744], in detail case 1 and case 3, see Figure 63. In both cases the lower edge of the geometry is clamped and on the upper edge a load of $\gamma\, \boldsymbol{PN}$ with $\boldsymbol{PN} = (0, -1)^T$ is applied. Additionally, for the third case, the mid point of the lower edge has a horizontal displacement of zero. The remaining boundaries are assumed to be stress free $\boldsymbol{PN} = (0, 0)^T$. The critical loads (for Hooke's law, linear elasticity) for these cases are given as

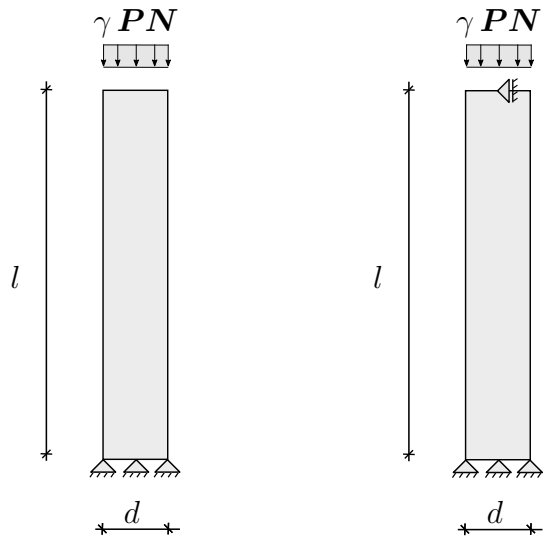

Figure 63: First and third Euler case.

$$\text{case 1: } \gamma_{\text{crit}} = \frac{\pi^2 E\, I}{(2l)^2} \quad \text{and} \quad \text{case 3: } \gamma_{\text{crit}} = \frac{\pi^2 E\, I}{(0.7l)^2}\,, \tag{133}$$

with the length of the column l, Young's Modulus E and the moment of inertia I. A Young's modulus of $E = 200$ and a length of $l = 10$ is assumed and a quadratic cross section area ($d \times d = 1 \times 1$) which yields $I = 1/12$. The Poisson's ratio is set to $\nu = 0$. This yields the critical loads

$$\text{case 1: } \gamma_{\text{crit}} \approx 0.41 \quad \text{and} \quad \text{case 3: } \gamma_{\text{crit}} \approx 3.36. \tag{134}$$

The main goal of this example is, to find the first critical load γ_{crit} where, beside the classical solution, a further solution (equilibrium path) appears.

As a result we expect nearly the same critical loads as for the classical Euler buckling analysis, although we use a nonlinear constitutive relation based on the free energy of Neo-Hookean type given in Equation (28.1), as long as we stay in the range of small strains. The stress boundary conditions are applied on $\boldsymbol{PN}$. For the computation a mixed least-squares element (RT_1P_2, neq= 1120, $\omega_1 = 1, \omega_2 = \omega_3 = 1/\mu$) and a standard quadratic displacement based Galerkin element (T_2, neq= 1440) are used. As it could be seen in Figure 64, both formulation compute nearly the same results for the two selected Euler buckling cases.

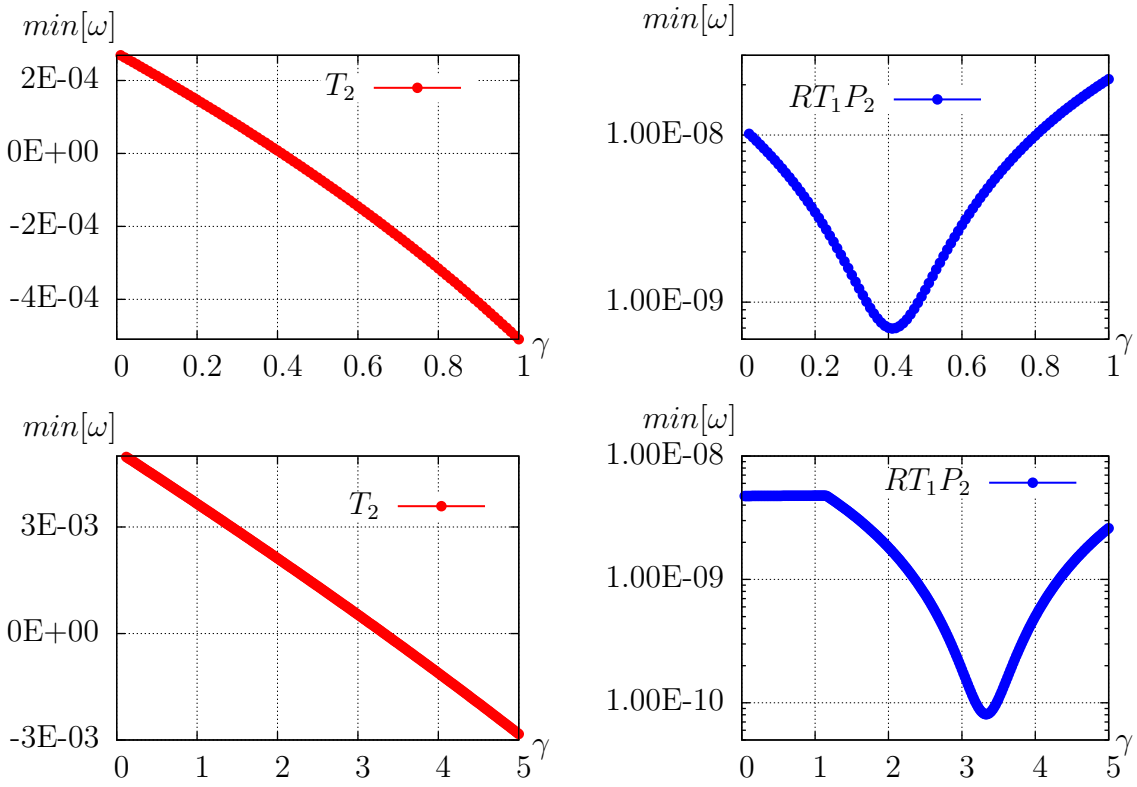

Figure 64: Results of stability analysis for T_2 (left,red) and RT_1P_2 (right,blue) for Euler case 1 (above) and for Euler case 3 (below) .

For the first Euler case the deformation is still that small, that the critical load from the linear theory is obtained. For the third case, the critical load is a little different due to the occuring nonlinear effects of the used constitutive law (Neo-Hooke instead of Hooke's law).

8.2 Example 2: Stability points, compare Auricchio et al. [2010] and Auricchio et al. [2013]

In the following two boundary value problems in line with Auricchio et al. [2010] and Auricchio et al. [2013] are considered. The constitutive relation is given by a Neo-Hooke free energy function (see Chapter 2.3.1, Equation (28.2). The geometry is the same for both problems (square material body $(-1,1)\times(-1,1)$), but the boundary conditions are different, see also Figure 65.

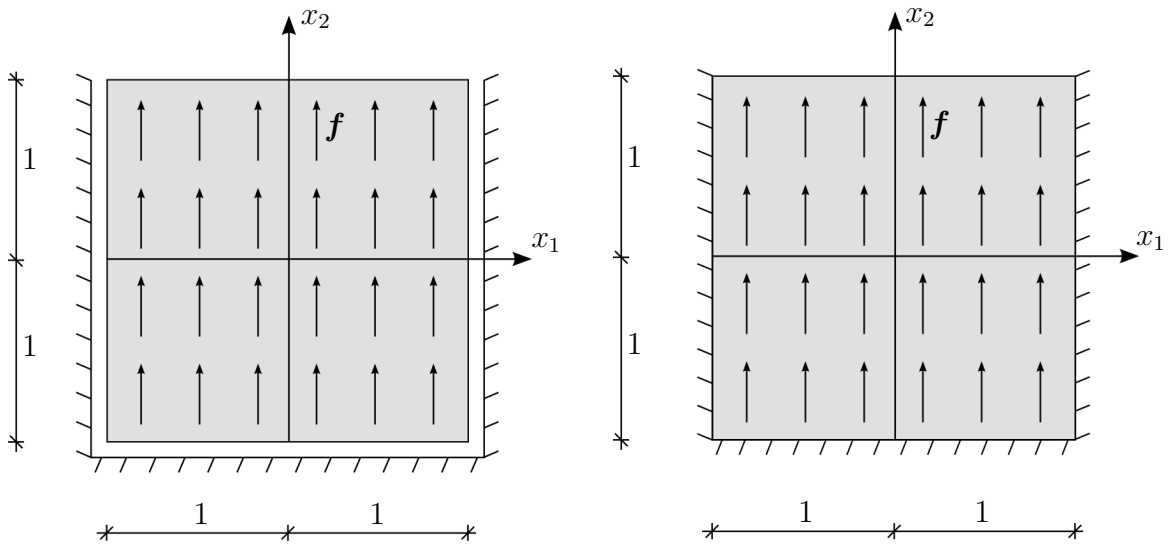

Figure 65: Incompressible blocks for stability analysis, problem 2 in Auricchio et al. [2010] (left) and problem 1 in Auricchio et al. [2013] (right).

As a load a body force $\boldsymbol{f} = (0,1)^T$ with the load factor γ is applied. We consider a nearly incompresible material with the Lamé parameters chosen as $\lambda = 10000\mu$ and $\mu = 1$ (Young's modulus $E = 2.9999$, Poisson's ration $\nu = 0.4995$). The weights for the least-squares mixed finite are chosen as $\omega_1 = 1, \omega_2 = \omega_3 = 1/\mu$. Due to the (nearly) incompressible material and the given boundary conditions, just the solution for a zero displacement field seems possible. But for specific critical loads γ_{crit} there exist also further solutions. For the computation of the results a Galerkin element (T_2) and different least-squares elements are used. If a computation (the numerical scheme) diverges, the result is not marked in the plots.

8.2.1 Stability points, problem 2 in Auricchio et al. [2010] For this problem, zero normal displacements on three sides are applied (lower, right and left) and on the remaining (upper) side a stress free boundary condition is given, see also Figure 65 (left). Here the free energy given in Equation (28.2) with the second term of (29) is considered. The critical load factor in Auricchio et al. [2010] is given by $\gamma_{crit} = 3.23\mu$. For the Galerkin T_2 element three different meshes are considered, whereas for the least-squares elements RT_1P_2 five discretizations are investigated. Again, the main goal of this example is to find the first critical load γ_{crit} where, beside the classical solution, a further solution (equilibrium path) appears. The results are shown in Figure 66, where the legends state

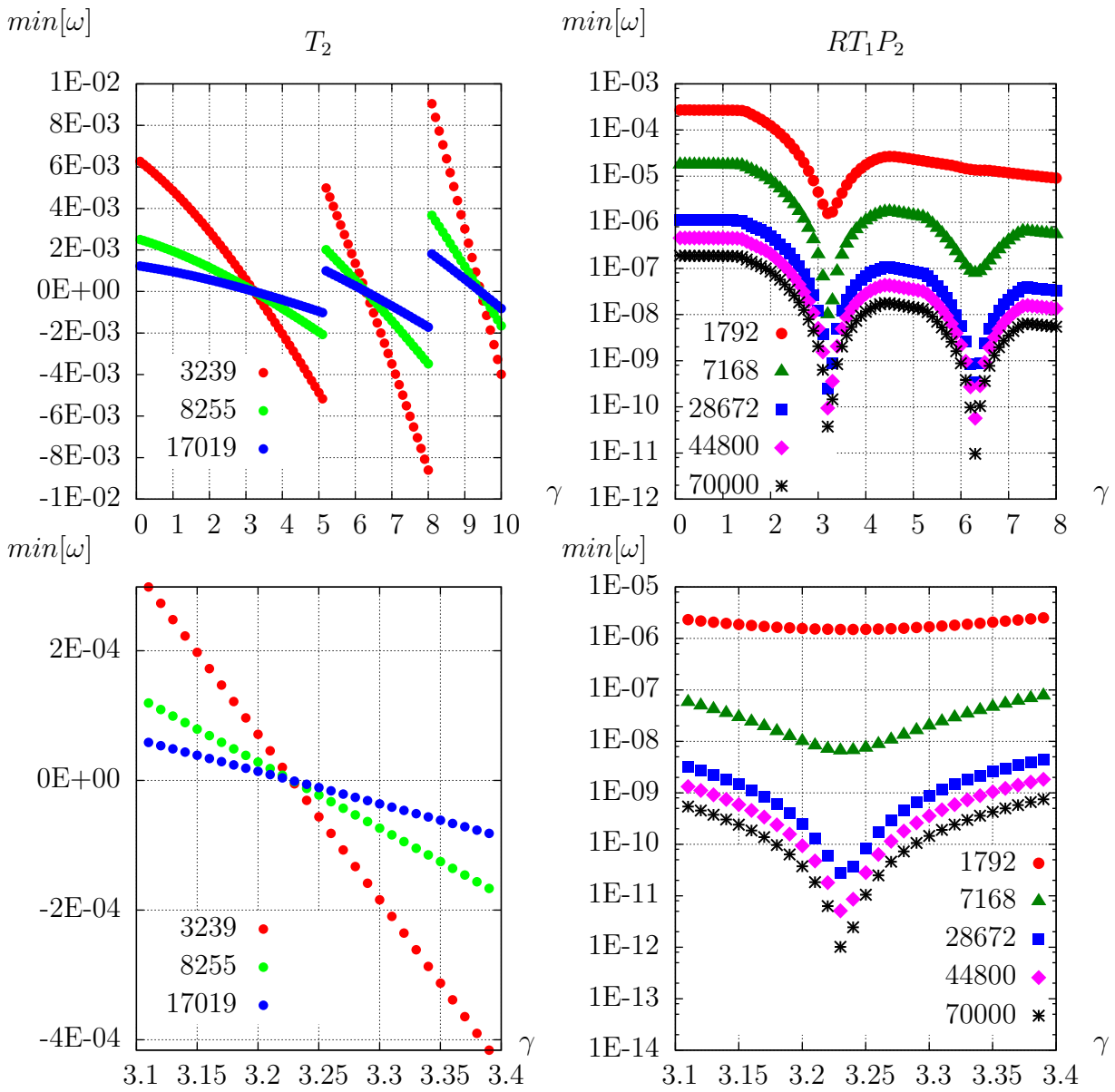

Figure 66: Result of stability analysis for the standard Galerkin element T_2 (left) and the least-squares element RT_1P_2 (right) for different number of equations (stated in the legend) for problem 2 in Auricchio et al. [2010].

the number of equations of the computation. The results are given by an overview (above) and for a better detection of the critical load, by a detailed view (below) around the first negative smallest eigenvalue (Galerkin element) respectively the local minimum of the smallest eigenvalue (least-squares formulation). For the overview a load factor step size of $\Delta\gamma = 0.1$ and for the detailed view of $\Delta\gamma = 0.01$ has been used.
It can be seen that both elements are able to compute the first bifurcation point correctly. The least-squares solution shows, due to the nature of the minimization problem, solely positive smallest eigenvalues in contrast to the Galerkin formulation, where the eigenvalues run from positive to negative. The solution for the least-squares element is more precise for a more refined mesh, since the minimum shows up more clearly.

8.2.2 Stability points, problem 1 in Auricchio et al. [2013] The second problem is characterized by clamped boundary conditions on three sides (lower, right and left), see Figure 65 (right). For this example three different terms for the incompressibility constraint $\theta(J)$ are investigated, see Equation (28.2) and Equation (29). The critical load factor is given by $\gamma_{crit} = 6.60\mu$. The chosen mesh for the Galerkin computations is given by $n = 16$ elements per side leading to $neq = 1984$. For the two least-squares elements a comparable number of equations (RT_1P_2, $neq = 7168$ and RT_2P_3, $neq = 7260$) is used. The results are shown in Figure 67.
It can be seen that the Galerkin element computes the correct bifurcation point. The least-squares formulation can detect the critical loads correctly with the choice of a suitable interpolation order. Several computations (the numerical scheme) diverge for the element type RT_1P_2 and the provided mesh in the region of the bifurcation point, but raising the polynomial order and using the element type RT_2P_3 leads to a satisfying result. The different terms used in the free energy, see Equation (28.2) and Equation (29), have no influence on the results for the Galerkin and the least-squares elements.

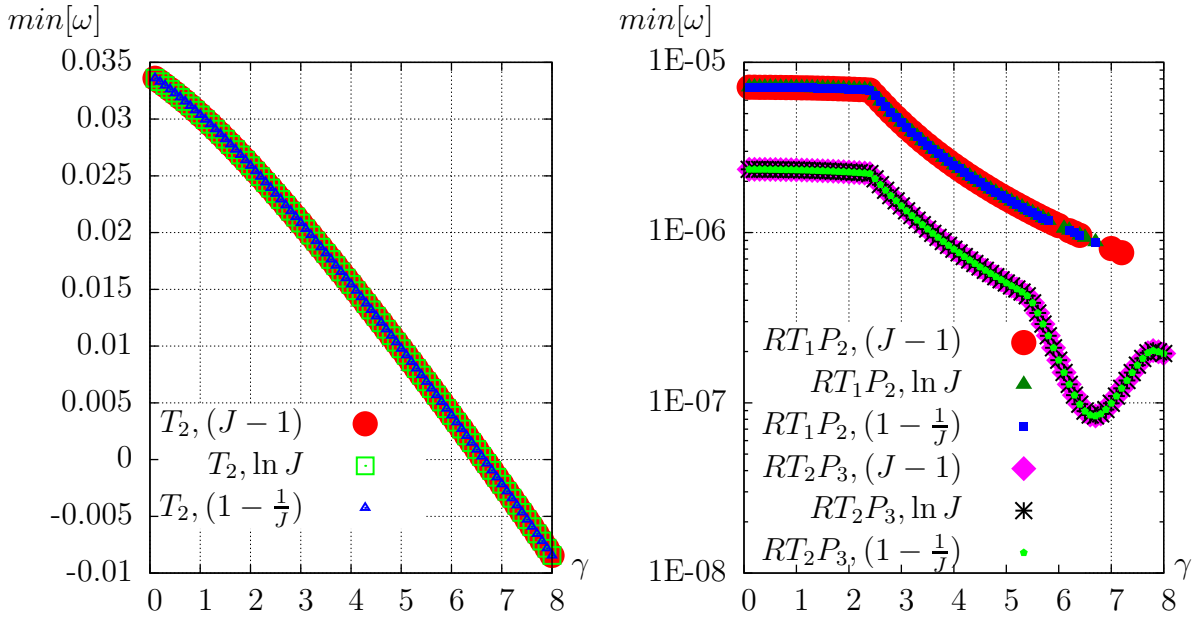

Figure 67: Result of stability analysis for the standard Galerkin element T_2 (left) and the least-squares elements RT_1P_2 and RT_2P_3 (right) for problem 1 in Auricchio et al. [2013] .

9 Summary, conclusion and outlook

Summary In the present work a least-squares formulation for hyperelastic materials has been provided and investigated. Therefore, the used transformation rules, several kinematical quantities, deformation measures and stress quantities have been introduced. In that framework principal invariants of the right Cauchy-Green deformation tensor $\boldsymbol{C}$ as well as mixed invariants have been defined. In the following several different hyperelastic material laws based on free energy functions of Neo-Hookean and Mooney-Rivlin type have been introduced. Furthermore, a transversely isotropic constitutive relation has been given based on a free energy function of Neo-Hookean type. For all constitutive relations the second Piola-Kirchhoff stress tensor $\boldsymbol{S}$ has been derived as the derivative of the given free energy functions. In the following the used interpolation spaces have been introduced and the construction of suitable interpolation functions for the approximation in $W^{1,p}(\mathcal{B})$ (standard interpolation polynomials) and $W^q(\text{div}, \mathcal{B})$ (vector-valued Raviart-Thomas interpolation functions) have been derived. Here, for the derivation of the Raviart-Thomas functions, also an alternative way of construction has been provided to make the application more convenient. A general procedure for the construction of a least-squares functional has been described and applied for a least-squares mixed finite element formulation. Basis for the element formulation has been a div-grad first-order system consisting of the equilibrium condition, the constitutive equation and a stress symmetry condition all written in a residual form. The solution variables (displacements and stresses) have been, dependent on the element type, interpolated using different approximation spaces. The resulting elements have been named as $P_m P_k$ (stresses and displacements in $W^{1,p}(\mathcal{B})$) and $RT_m P_k$ (stresses in $W^q(\text{div}, \mathcal{B})$ and displacements in $W^{1,p}(\mathcal{B})$). Here, m (stresses) and k (displacements) denote the polynomial order of the particular interpolation function. For a deeper understanding of the least-squares method, a simple one-dimensional geometrically nonlinear example has been provided which explains - step by step - how to deal with a least-squares mixed finite element for nonlinear materials. After that the used element types have been presented with respect to the nodal coordinates, the number of degrees of freedom and the resulting interpolation matrices. In addition to that, some remarks have been given concerning the application of boundary conditions on the different element types due to the varying nodal degrees of freedom of the stresses. Next, a few remarks on the implementation have been given as e.g. concerning the way of coding in AceGen. Then the performance of the provided elements has been investigated by extensive numerical studies with respect to e.g. bending dominated problems, incompressibility, stability issues and convergence of the field quantities and has been compared to standard and mixed Galerkin elements. Furthermore, the crucial influence of suitable weighting has been discussed. In addition to that the formulation has been tested with respect to its sensitivity to volumetric locking. Next, the least-squares functional has been used as a local error estimator for the application of adaptive mesh refinement. Therefore, two different marking strategies have been presented and tested under usage of a simple refinement strategy. In this context also the resulting convergence rates have been discussed. The last investigation has been done about the detection of bifurcation points. Therefore, starting with the classical Euler buckling cases the stability points have been computed and compared to the results computed by a standard Galerkin element. Furthermore, two additional examples for the detection of these points are investigated.

Conclusion It could be stated, that the provided least-squares mixed finite element formulation is a suitable approach for the solution of problems in the field of solid mechanics. Both element types, RT_mP_k as well as P_mP_k, give reliable results considering the displacement field, compare e.g. Chapter 5.1 respectively, Chapter 5.2. The usage of high-order elements ($m \geq 2$, $k \geq 3$) leads, as it would have been expected, to a better performance. Especially for adaptively refined meshes this reflects also in higher convergence rates. The approximation of the stress field yields a smooth distribution even considering an incompressible material. Furthermore, the resulting reaction forces can be computed suitably. However, it should be remarked, that the interpolation of the stresses in $W^{1,p}(\mathcal{B})$ can lead to problems e.g. in case of material transitions, as it has been shown in Chapter 5.4. This is due to the fact, that the occurring pollution effect in the stress field (and possibly excessive values) could influence the solution crucially e.g. in case of plasticity or crack simulation. The interpolation of the stress field in $W^q(\mathrm{div}, \mathcal{B})$ and the resulting elements of type RT_mP_k give reliable results for the stresses for all boundary value problems under consideration. Thus it can be concluded, that the element type RT_mP_k is the better choice. Vector-valued Raviart-Thomas interpolation functions for the interpolation of the stresses in $W^q(\mathrm{div}, \mathcal{B})$ are a suitable choice and could be constructed as given in Chapter 3.3. The influence of weighting plays a crucial role with respect to the convergence of the field quantities (and the resulting convergence rates), compare e.g. Chapter 5.2. This effect becomes strongly viewable in case of the bending dominated cantilever beam under consideration. As the bending moment has a stronger influence on the deflection of the beam than the shear force (see also the beam theory of *Bernoulli*), the strengthening of the stress symmetry by a suitable weight for the residual which includes this connection improves the overall performance of the formulation. Unfortunately, the choice of weights depends on the boundary value problem of consideration and furthermore on the quantity of interest. However, for all applied weighting factor combinations, convergent solution can be found (even though a high number of degrees of freedom is necessary). It should be remarked, that inappropriate weighting can lead to ill-conditioned systems and/or unphysical results. The provided formulation is also applicable for transversely isotropic materials as far as it has been investigated in the framework of this thesis.

It can be stated, that the provided least-squares formulation shows a slight sensitiveness with respect to volumetric locking. In this context it should be remarked, that the quantitative error for the least-squares element could not be the only indicator for locking (if the functional is considered as a measurement), as a residual weighting somehow by the material parameter λ could weight this effect out of the functional. However, the loss of convergence rate can be seen as a suitable indicator for locking. But, even though the volumetric locking affects the performance of the element slightly with respect to the convergence rate, the stresses for incompressible materials can be computed correctly, see Chapter 5.3. To reach optimal convergence rates even for problems which are not regular, adaptive mesh refinement is a suitable tool. The usage of the least-squares functional as a local error indicator and the application of different marking strategy leads to significantly improved convergence rates. This is a great benefit of the method, as the local error indicator is given without any additional costs. As presented in Chapter 8, the provided formulation shows a good performance in detecting bifurcation points for different boundary value problems. Finally, with regard to the provided formulation it can be stated, that the overall performance is generally satisfactory, but there are still many open problems and possibilities of improvement.

Outlook As the formulation is sensitive with respect to weightings and material parameters, the robustness of the method should be considered and stabilization techniques should be investigated. Especially the reliability of the result under consideration of problems on arbitrary scales or highly jumping coefficients should be investigated and possible enhancements should be developed. In addition to that, the condition of the resulting matrices should be discussed in detail. Furthermore, the obtained results should be confirmed also for the three-dimensional case in more detail. For this several work is already done, but not finalized at this point and therefore not part of this contribution. Especially the extension of the vector-valued Raviart-Thomas functions for the interpolation in $W^q(\mathrm{div}, \mathcal{B})$ to the three-dimensional case for high-order interpolations is important. As the $P_m P_k$ elements have an issue if the physical solution is not part of $W^{1,p}(\mathcal{B})$ but only of $W^q(\mathrm{div}, \mathcal{B})$ a discontinuous interpolation of the stresses (in $L^2(\mathcal{B})$), as it is done for e.g. mixed Galerkin elements, could be a possible solution. Due to the straightforward construction of the least-squares functional an application of the method to coupled problems (as e.g. thermo-mechanical or electro-mechanical coupling) is obvious. For that basic formulations are already developed beside this contribution and will be investigated further. The elements in this contribution are restricted to the geometrically nonlinear elastic case, hence the extension of the formulation to inelastic problems (as e.g. finite plasticity) is an open problem.

A Appendix

A.1 Basis functions for order $m = 2$

For RT_2 the numbering of the interpolation sites given in Figure 68.

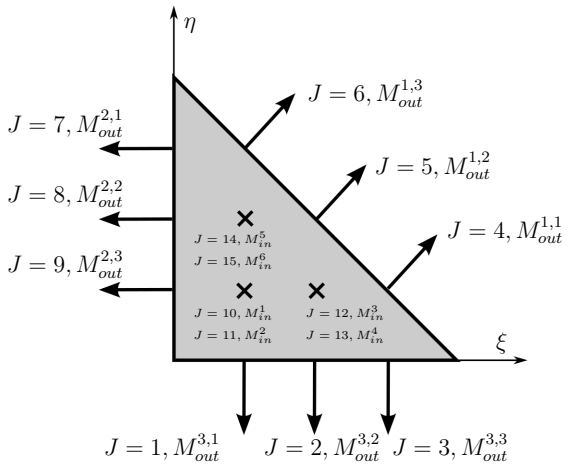

Figure 68: Numbering of interpolation sites J for RT_2

The general basis of order $m = 2$ is given as

$$\begin{aligned} \hat{\boldsymbol{v}}_2(\xi,\eta) &= \begin{pmatrix} a_1 + a_2\xi^2 + a_3\xi\eta + a_4\eta^2 + a_5\xi + a_6\eta \\ b_1 + b_2\xi^2 + b_3\xi\eta + b_4\eta^2 + b_5\xi + b_6\eta \end{pmatrix} \\ &+ (c_1\xi^2 + c_2\xi\eta + c_3\eta^2)\begin{pmatrix} \xi \\ \eta \end{pmatrix}. \end{aligned} \tag{135}$$

The complete set of functions $\hat{q}_2^{L,K}$ and $\hat{\boldsymbol{q}}_1^I$ and necessary additional conditions (correlation of coordinates) for the construction of RT_2 are given in Table 10. For edge $L = 1$ the integral expression is transformed using $ds = \sqrt{2}d\xi$. The resulting solution vector is given as

$$(a_1, a_2, a_3, a_4, a_5, a_6, b_1, b_2, b_3, b_4, b_5, b_6, c_1, c_2, c_3)^T . \tag{136}$$

We obtain for the outer basis functions of order $m = 2$ the coefficients given in Table 11 and for the inner basis functions in Table 12.

L	K	I	$\hat{q}_2^{L,K}$ / $\hat{\boldsymbol{q}}_1^I$	correlation of coordinates
1	1	-	$6\,(2\xi^2-\xi)$	$\eta = 1-\xi$
1	2	-	$6\frac{1}{4}\,(4\xi-4\xi^2)$	$\eta = 1-\xi$
1	3	-	$6(2\xi^2-3\xi+1)$	$\eta = 1-\xi$
2	1	-	$6(2\eta^2-\eta)$	$\xi = 0$
2	2	-	$6\frac{1}{4}\,(4\eta-4\eta^2)$	$\xi = 0$
2	3	-	$6(2\eta^2-3\eta+1)$	$\xi = 0$
3	1	-	$6(2\xi^2-3\xi+1)$	$\eta = 0$
3	2	-	$6\frac{1}{4}\,(4\xi-4\xi^2)$	$\eta = 0$
3	3	-	$6(2\xi^2-\xi)$	$\eta = 0$
-	-	1	$(-\eta-\xi+1,0)^T$	-
-	-	2	$(0,-\eta-\xi+1)^T$	-
-	-	3	$(\xi,0)^T$	-
-	-	4	$(0,\xi)^T$	-
-	-	5	$(\eta,0)^T$	-
-	-	6	$(0,\eta)^T$	-

Table 10: Set of functions $\hat{q}_2^{L,K}$ and $\hat{\boldsymbol{q}}_1^I$ and correlation of coordinates for the construction of RT_3.

	$\hat{v}_2^1$	$\hat{v}_2^2$	$\hat{v}_2^3$	$\hat{v}_2^4$	$\hat{v}_2^5$	$\hat{v}_2^6$	$\hat{v}_2^7$	$\hat{v}_2^8$	$\hat{v}_2^9$
a_1	0	0	0	0	0	0	$-\frac{1}{2}$	1	$-\frac{3}{2}$
a_2	-10	$\frac{35}{2}$	$-\frac{15}{2}$	$-\frac{15}{2}$	$-\frac{25}{2}$	0	0	-10	-15
a_3	-10	0	0	0	-15	-5	-5	25	-20
a_4	0	0	0	0	0	0	-5	10	-5
a_5	3	$-\frac{7}{2}$	$\frac{3}{2}$	$\frac{3}{2}$	4	$\frac{1}{2}$	$\frac{1}{2}$	$\frac{3}{2}$	9
a_6	0	0	0	0	0	0	4	-10	6
b_1	$-\frac{3}{2}$	1	$-\frac{1}{2}$	0	0	0	0	0	0
b_2	-5	10	-5	0	0	0	0	0	0
b_3	-20	25	-5	-5	-15	0	0	0	-10
b_4	-15	-10	0	0	$-\frac{25}{2}$	$-\frac{15}{2}$	$-\frac{15}{2}$	$\frac{35}{2}$	-10
b_5	6	-10	4	0	0	0	0	0	0
b_6	9	$\frac{3}{2}$	$\frac{1}{2}$	$\frac{1}{2}$	4	$\frac{3}{2}$	$\frac{3}{2}$	$-\frac{7}{2}$	3
c_1	$\frac{15}{2}$	-15	$\frac{15}{2}$	$\frac{15}{2}$	$\frac{15}{2}$	0	0	$\frac{15}{2}$	$\frac{15}{2}$
c_2	15	-15	0	0	30	0	0	-15	15
c_3	$\frac{15}{2}$	$\frac{15}{2}$	0	0	$\frac{15}{2}$	$\frac{15}{2}$	$\frac{15}{2}$	-15	$\frac{15}{2}$

Table 11: Set of coefficients for the construction of RT_2, outer functions.

	$\hat{v}_2^{10}$	$\hat{v}_2^{11}$	$\hat{v}_2^{12}$	$\hat{v}_2^{13}$	$\hat{v}_2^{14}$	$\hat{v}_2^{15}$
a_1	0	0	0	0	0	0
a_2	-450	-150	360	240	60	30
a_3	-300	-300	60	120	360	240
a_4	0	0	0	0	0	0
a_5	180	60	-90	-60	-60	-30
a_6	0	0	0	0	0	0
b_1	0	0	0	0	0	0
b_2	0	0	0	0	0	0
b_3	-300	-300	240	360	120	60
b_4	-150	-450	30	60	240	360
b_5	0	0	0	0	0	0
b_6	60	180	-30	-60	-60	-90
c_1	270	90	-270	-180	0	0
c_2	360	360	-180	-360	-360	-180
c_3	90	270	0	0	-180	-270

Table 12: Set of coefficients for the construction of RT_2, inner functions.

A.2 Basis functions for order $m = 3$

For RT_3 the numbering of the interpolation sites given in Figure 69.

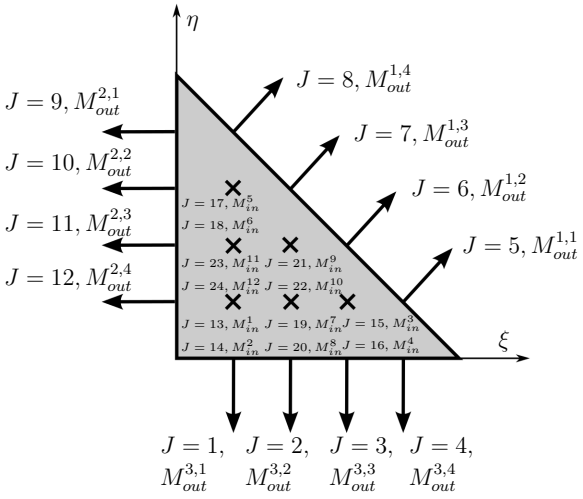

Figure 69: Numbering of interpolation sites J for RT_3

The general basis of order $m = 3$ is given as

$$\begin{aligned} \hat{\boldsymbol{v}}_3(\xi,\eta) &= \begin{pmatrix} a_1 + a_2\xi + a_3\eta + a_4\xi^2 + a_5\eta\xi + a_6\eta^2 + a_7\xi^3 + a_8\eta\xi^2 + a_9\eta^2\xi + a_{10}\eta^3 \\ b_1 + b_2\xi + b_3\eta + b_4\xi^2 + b_5\eta\xi + b_6\eta^2 + b_7\xi^3 + b_8\eta\xi^2 + b_9\eta^2\xi + b_{10}\eta^3 \end{pmatrix} \\ &+ (c_1\xi^3 + c_2\eta\xi^2 + c_3\eta^2\xi + c_4\eta^3)\begin{pmatrix} \xi \\ \eta \end{pmatrix}. \end{aligned} \tag{137}$$

The complete set of functions $\hat{q}_3^{L,K}$ and $\hat{\boldsymbol{q}}_2^I$ and necessary additional conditions (correlation of coordinates) for the construction of RT_3 are given in Table 13. For edge $L = 1$ we transform the integral expression using $ds = \sqrt{2}d\xi$. The resulting solution vector is given as

$$(a_1, a_2, a_3, a_4, a_5, a_6, a_7, a_8, a_9, a_{10}, b_1, b_2, b_3, b_4, b_5, b_6, b_7, b_8.b_9, b_{10}, c_1, c_2, c_3, c_4)^T.$$

We obtain for the outer basis functions of order $m = 3$ the coefficients given in Table 14 and for the inner basis functions in Table 15 and Table 16.

L	K	I	$\hat{q}_1^{L,K}$ / $\hat{\boldsymbol{q}}_0^I$	correlation of coordinates
1	1	-	$\frac{8}{3}\left(\frac{9\xi^3}{2}-\frac{9\xi^2}{2}+\xi\right)$	$\eta = 1-\xi$
1	2	-	$\frac{8}{3}\left(-\frac{27\xi^3}{2}+18\xi^2-\frac{9\xi}{2}\right)$	$\eta = 1-\xi$
1	3	-	$\frac{8}{3}\left(\frac{27\xi^3}{2}-\frac{45\xi^2}{2}+9\xi\right)$	$\eta = 1-\xi$
1	4	-	$\frac{8}{3}\left(-\frac{9\xi^3}{2}+9\xi^2-\frac{11\xi}{2}+1\right)$	$\eta = 1-\xi$
2	1	-	$\frac{8}{3}\left(\frac{9\eta^3}{2}-\frac{9\eta^2}{2}+\eta\right)$	$\xi = 0$
2	2	-	$\frac{8}{3}\left(-\frac{27\eta^3}{2}+18\eta^2-\frac{9\eta}{2}\right)$	$\xi = 0$
2	3	-	$\frac{8}{3}\left(\frac{27\eta^3}{2}-\frac{45\eta^2}{2}+9\eta\right)$	$\xi = 0$
2	4	-	$\frac{8}{3}\left(-\frac{9\eta^3}{2}+9\eta^2-\frac{11\eta}{2}+1\right)$	$\xi = 0$
3	1	-	$\frac{8}{3}\left(-\frac{9\xi^3}{2}+9\xi^2-\frac{11\xi}{2}+1\right)$	$\eta = 0$
3	2	-	$\frac{8}{3}\left(\frac{27\xi^3}{2}-\frac{45\xi^2}{2}+9\xi\right)$	$\eta = 0$
3	3	-	$\frac{8}{3}\left(-\frac{27\xi^3}{2}+18\xi^2-\frac{9\xi}{2}\right)$	$\eta = 0$
3	4	-	$\frac{8}{3}\left(\frac{9\xi^3}{2}-\frac{9\xi^2}{2}+\xi\right)$	$\eta = 0$
-	-	1	$(2\eta^2+4\eta\xi-3\eta+2\xi^2-3\xi+1,0)^T$	-
-	-	2	$(0,2\eta^2+4\eta\xi-3\eta+2\xi^2-3\xi+1)^T$	-
-	-	3	$(2\xi^2-\xi,0)^T$	-
-	-	4	$(0,2\xi^2-\xi)^T$	-
-	-	5	$(2\eta^2-\eta,0)^T$	-
-	-	6	$(0,2\eta^2-\eta)^T$	-
-	-	7	$(0,-4\eta\xi-4\xi^2+4\xi)^T$	-
-	-	8	$(-4\eta\xi-4\xi^2+4\xi,0)^T$	-
-	-	9	$(0,4\eta\xi)^T$	-
-	-	10	$(4\eta\xi,0)^T$	-
-	-	11	$(0,-4\eta^2-4\eta\xi+4\eta)^T$	-
-	-	12	$(-4\eta^2-4\eta\xi+4\eta,0)^T$	-

Table 13: Set of functions $\hat{q}_3^{L,K}$ and $\hat{\boldsymbol{q}}_2^I$ and correlation of coordinates for the construction of RT_3.

	$\hat{v}_3^1$	$\hat{v}_3^2$	$\hat{v}_3^3$	$\hat{v}_3^4$	$\hat{v}_3^5$	$\hat{v}_3^6$	$\hat{v}_3^7$	$\hat{v}_3^8$	$\hat{v}_3^9$	$\hat{v}_3^{10}$	$\hat{v}_3^{11}$	$\hat{v}_3^{12}$
a_1	0	0	0	0	0	0	0	0	$\frac{1}{2}$	$-\frac{4}{9}$	$\frac{17}{18}$	-2
a_2	5	$-\frac{37}{9}$	$\frac{19}{9}$	-2	-2	$-\frac{9}{2}$	-3	$-\frac{1}{2}$	$-\frac{1}{2}$	$-\frac{14}{9}$	$\frac{19}{18}$	20
a_3	0	0	0	0	0	0	0	0	$-\frac{15}{2}$	$\frac{25}{3}$	$-\frac{95}{6}$	15
a_4	-30	$\frac{100}{3}$	$-\frac{64}{3}$	18	18	30	12	0	0	$\frac{13}{3}$	$-\frac{76}{3}$	-60
a_5	-30	$\frac{22}{3}$	$\frac{14}{3}$	0	0	21	30	9	9	6	75	-90
a_6	0	0	0	0	0	0	0	0	$\frac{45}{2}$	$-\frac{85}{3}$	$\frac{215}{6}$	-30
a_7	$\frac{105}{2}$	-63	$\frac{105}{2}$	-42	-42	$-\frac{154}{3}$	$-\frac{35}{3}$	0	0	$\frac{7}{9}$	$\frac{434}{9}$	70
a_8	105	$-\frac{266}{3}$	$-\frac{49}{3}$	0	0	-112	-98	0	0	$-\frac{119}{2}$	-98	$\frac{315}{2}$
a_9	$\frac{105}{2}$	$\frac{56}{3}$	$-\frac{49}{6}$	0	0	$-\frac{35}{2}$	-56	$-\frac{63}{2}$	$-\frac{63}{2}$	$\frac{140}{3}$	$-\frac{721}{6}$	105
a_{10}	0	0	0	0	0	0	0	0	$-\frac{35}{2}$	$\frac{385}{18}$	$-\frac{385}{18}$	$\frac{35}{2}$
b_1	-2	$\frac{17}{18}$	$-\frac{4}{9}$	$\frac{1}{2}$	0	0	0	0	0	0	0	0
b_2	15	$-\frac{95}{6}$	$\frac{25}{3}$	$-\frac{15}{2}$	0	0	0	0	0	0	0	0
b_3	20	$\frac{19}{18}$	$-\frac{14}{9}$	$-\frac{1}{2}$	$-\frac{1}{2}$	-3	$-\frac{9}{2}$	-2	-2	$\frac{19}{9}$	$-\frac{37}{9}$	5
b_4	-30	$\frac{215}{6}$	$-\frac{85}{3}$	$\frac{45}{2}$	0	0	0	0	0	0	0	0
b_5	-90	75	6	9	9	30	21	0	0	$\frac{14}{3}$	$\frac{22}{3}$	-30
b_6	-60	$-\frac{76}{3}$	$\frac{13}{3}$	0	0	12	30	18	18	$-\frac{64}{3}$	$\frac{100}{3}$	-30
b_7	$\frac{35}{2}$	$-\frac{385}{18}$	$\frac{385}{18}$	$-\frac{35}{2}$	0	0	0	0	0	0	0	0
b_8	105	$-\frac{721}{6}$	$\frac{140}{3}$	$-\frac{63}{2}$	$-\frac{63}{2}$	-56	$-\frac{35}{2}$	0	0	$-\frac{49}{6}$	$\frac{56}{3}$	$\frac{105}{2}$
b_9	$\frac{315}{2}$	-98	$-\frac{119}{2}$	0	0	-98	-112	0	0	$-\frac{49}{3}$	$-\frac{266}{3}$	105
b_{10}	70	$\frac{434}{9}$	$\frac{7}{9}$	0	0	$-\frac{35}{3}$	$-\frac{154}{3}$	-42	-42	$\frac{105}{2}$	-63	$\frac{105}{2}$
c_1	-28	$\frac{308}{9}$	$-\frac{308}{9}$	28	28	$\frac{224}{9}$	$\frac{28}{9}$	0	0	$-\frac{28}{9}$	$-\frac{224}{9}$	-28
c_2	-84	$\frac{280}{3}$	$-\frac{28}{3}$	0	0	112	56	0	0	$\frac{140}{3}$	$\frac{112}{3}$	-84
c_3	-84	$\frac{112}{3}$	$\frac{140}{3}$	0	0	56	112	0	0	$-\frac{28}{3}$	$\frac{280}{3}$	-84
c_4	-28	$-\frac{224}{9}$	$-\frac{28}{9}$	0	0	$\frac{28}{9}$	$\frac{224}{9}$	28	28	$-\frac{308}{9}$	$\frac{308}{9}$	-28

Table 14: Set of coefficients for the construction of RT_3, outer functions.

	$\hat{v}_3^{13}$	$\hat{v}_3^{14}$	$\hat{v}_3^{15}$	$\hat{v}_3^{16}$	$\hat{v}_3^{17}$	$\hat{v}_3^{18}$
a_1	0	0	0	0	0	0
a_2	960	240	288	216	144	72
a_3	0	0	0	0	0	0
a_4	−4320	−1080	−2304	−1728	−144	−72
a_5	−3240	−2160	−216	−432	−1944	−1152
a_6	0	0	0	0	0	0
a_7	6048	1512	4704	3528	0	0
a_8	9072	6048	1512	3024	2016	1008
a_9	3024	4536	0	0	4536	3528
a_{10}	0	0	0	0	0	0
b_1	0	0	0	0	0	0
b_2	0	0	0	0	0	0
b_3	240	960	72	144	216	288
b_4	0	0	0	0	0	0
b_5	−2160	−3240	−1152	−1944	−432	−216
b_6	−1080	−4320	−72	−144	−1728	−2304
b_7	0	0	0	0	0	0
b_8	4536	3024	3528	4536	0	0
b_9	6048	9072	1008	2016	3024	1512
b_{10}	1512	6048	0	0	3528	4704
c_1	−2688	−672	−2688	−2016	0	0
c_2	−6048	−4032	−2016	−4032	0	0
c_3	−4032	−6048	0	0	−4032	−2016
c_4	−672	−2688	0	0	−2016	−2688

Table 15: Set of coefficients for the construction of RT_3, inner functions, $\hat{v}_3^{13}$ up to $\hat{v}_3^{18}$.

	$\hat{v}_3^{19}$	$\hat{v}_3^{20}$	$\hat{v}_3^{21}$	$\hat{v}_3^{22}$	$\hat{v}_3^{23}$	$\hat{v}_3^{24}$
a_1	0	0	0	0	0	0
a_2	−48	−66	216	144	6	−12
a_3	0	0	0	0	0	0
a_4	720	486	−1098	−774	−468	−72
a_5	−216	216	−1332	−1044	1188	360
a_6	0	0	0	0	0	0
a_7	−1344	−756	1554	1134	1134	252
a_8	−756	−2268	4788	4032	−2772	−504
a_9	504	378	1638	1638	−1512	−1008
a_{10}	0	0	0	0	0	0
b_1	0	0	0	0	0	0
b_2	0	0	0	0	0	0
b_3	−12	6	144	216	−66	−48
b_4	0	0	0	0	0	0
b_5	360	1188	−1044	−1332	216	−216
b_6	−72	−468	−774	−1098	486	720
b_7	0	0	0	0	0	0
b_8	−1008	−1512	1638	1638	378	504
b_9	−504	−2772	4032	4788	−2268	−756
b_{10}	252	1134	1134	1554	−756	−1344
c_1	672	336	−672	−504	−672	−168
c_2	1008	2016	−3528	−3024	1512	0
c_3	0	1512	−3024	−3528	2016	1008
c_4	−168	−672	−504	−672	336	672

Table 16: Set of coefficients for the construction of RT_3, inner functions, $\hat{v}_3^{19}$ up to $\hat{v}_3^{24}$.

A.3 Alternative basis functions for order $m = 1$

Following the alternative way of construction for $m = 1$ we obtain the vector-valued basis functions (respectively the coefficients) as given in Table 17.

	$\hat{v}_2^1$	$\hat{v}_2^2$	$\hat{v}_2^3$	$\hat{v}_2^4$	$\hat{v}_2^5$	$\hat{v}_2^6$	$\hat{v}_2^7$	$\hat{v}_2^8$
a_1	0	0	0	0	1	−2	0	0
a_2	2	−1	−1	−1	−1	5	6	3
a_3	0	0	0	0	−3	3	0	0
b_1	−2	1	0	0	0	0	0	0
b_2	3	−3	0	0	0	0	0	0
b_3	5	−1	−1	−1	−1	2	3	6
c_1	−3	3	3	0	0	−3	−6	−3
c_2	−3	0	0	3	3	−3	−3	−6

Table 17: Alternative set of coefficients for the construction of RT_1.

A.4 Alternative basis functions for order $m = 2$

Constructing the basis for order $m = 2$ using the alternative way, leads to the coefficients for the outer degrees of freedom given in Table 18 and for the inner basis functions in Table 19.

	$\hat{v}_2^1$	$\hat{v}_2^2$	$\hat{v}_2^3$	$\hat{v}_2^4$	$\hat{v}_2^5$	$\hat{v}_2^6$	$\hat{v}_2^7$	$\hat{v}_2^8$	$\hat{v}_2^9$
a_1	0	0	0	0	0	0	−1	3	−3
a_2	−10	16	−6	−6	−4	0	0	4	−18
a_3	−10	4	0	0	−4	−6	−6	32	−26
a_4	0	0	0	0	0	0	−8	16	−8
a_5	3	−3	1	1	1	1	1	−7	13
a_6	0	0	0	0	0	0	6	−16	10
b_1	−3	3	−1	0	0	0	0	0	0
b_2	−8	16	−8	0	0	0	0	0	0
b_3	−26	32	−6	−6	−4	0	0	4	−10
b_4	−18	4	0	0	−4	−6	−6	16	−10
b_5	10	−16	6	0	0	0	0	0	0
b_6	13	−7	1	1	1	1	1	−3	3
c_1	8	−16	8	8	0	0	0	0	8
c_2	16	−16	0	0	16	0	0	−16	16
c_3	8	0	0	0	0	8	8	−16	8

Table 18: Alternative set of coefficients for the construction of RT_2, outer functions.

	$\hat{v}_2^{10}$	$\hat{v}_2^{11}$	$\hat{v}_2^{12}$	$\hat{v}_2^{13}$	$\hat{v}_2^{14}$	$\hat{v}_2^{15}$
a_1	0	0	0	0	0	0
a_2	−84	−28	60	40	16	8
a_3	−60	−52	8	16	72	44
a_4	0	0	0	0	0	0
a_5	36	12	−12	−8	−16	−8
a_6	0	0	0	0	0	0
b_1	0	0	0	0	0	0
b_2	0	0	0	0	0	0
b_3	−52	−60	44	72	16	8
b_4	−28	−84	8	16	40	60
b_5	0	0	0	0	0	0
b_6	12	36	−8	−16	−8	−12
c_1	48	16	−48	−32	0	0
c_2	64	64	−32	−64	−64	−32
c_3	16	48	0	0	−32	−48

Table 19: Alternative set of coefficients for the construction of RT_2, inner functions.

A.5 Alternative basis functions for order $m = 3$

The alternative coefficients of the basis functions for order $m = 3$ for the outer degrees of freedom are given in Table 20, for the inner basis functions in Table 21 and Table 22.

	$\hat{v}_3^1$	$\hat{v}_3^2$	$\hat{v}_3^3$	$\hat{v}_3^4$	$\hat{v}_3^5$	$\hat{v}_3^6$	$\hat{v}_3^7$	$\hat{v}_3^8$	$\hat{v}_3^9$	$\hat{v}_3^{10}$	$\hat{v}_3^{11}$	$\hat{v}_3^{12}$
a_1	0	0	0	0	0	0	0	0	1	-4	6	-4
a_2	4	-6	4	-1	-1	-1	-1	-1	-1	9	$-\frac{47}{2}$	$\frac{77}{3}$
a_3	0	0	0	0	0	0	0	0	$-\frac{55}{6}$	35	$-\frac{95}{2}$	$\frac{65}{3}$
a_4	$-\frac{65}{3}$	$\frac{95}{2}$	-35	$\frac{55}{6}$	$\frac{55}{6}$	$\frac{15}{2}$	5	0	0	-5	30	$-\frac{355}{6}$
a_5	$-\frac{65}{3}$	$\frac{35}{2}$	-5	0	0	5	$\frac{15}{2}$	$\frac{55}{6}$	$\frac{55}{6}$	$-\frac{145}{2}$	160	$-\frac{290}{3}$
a_6	0	0	0	0	0	0	0	0	25	$-\frac{175}{2}$	100	$-\frac{75}{2}$
a_7	$\frac{75}{2}$	-100	$\frac{175}{2}$	-25	-25	$-\frac{25}{2}$	0	0	0	0	$-\frac{25}{2}$	$\frac{175}{3}$
a_8	75	$-\frac{225}{2}$	$\frac{75}{2}$	0	0	$-\frac{75}{2}$	$-\frac{75}{2}$	0	0	$\frac{75}{2}$	-175	$\frac{275}{2}$
a_9	$\frac{75}{2}$	$-\frac{25}{2}$	0	0	0	0	$-\frac{25}{2}$	-25	-25	150	-225	100
a_{10}	0	0	0	0	0	0	0	0	$-\frac{125}{6}$	$\frac{125}{2}$	$-\frac{125}{2}$	$\frac{125}{6}$
b_1	-4	6	-4	1	0	0	0	0	0	0	0	0
b_2	$\frac{65}{3}$	$-\frac{95}{2}$	35	$-\frac{55}{6}$	0	0	0	0	0	0	0	0
b_3	$\frac{77}{3}$	$-\frac{47}{2}$	9	-1	-1	-1	-1	-1	-1	4	-6	4
b_4	$-\frac{75}{2}$	100	$-\frac{175}{2}$	25	0	0	0	0	0	0	0	0
b_5	$-\frac{290}{3}$	160	$-\frac{145}{2}$	$\frac{55}{6}$	$\frac{55}{6}$	$\frac{15}{2}$	5	0	0	-5	$\frac{35}{2}$	$-\frac{65}{3}$
b_6	$-\frac{355}{6}$	30	-5	0	0	5	$\frac{15}{2}$	$\frac{55}{6}$	$\frac{55}{6}$	-35	$\frac{95}{2}$	$-\frac{65}{3}$
b_7	$\frac{125}{6}$	$-\frac{125}{2}$	$\frac{125}{2}$	$-\frac{125}{6}$	0	0	0	0	0	0	0	0
b_8	100	-225	150	-25	-25	$-\frac{25}{2}$	0	0	0	0	$-\frac{25}{2}$	$\frac{75}{2}$
b_9	$\frac{275}{2}$	-175	$\frac{75}{2}$	0	0	$-\frac{75}{2}$	$-\frac{75}{2}$	0	0	$\frac{75}{2}$	$-\frac{225}{2}$	75
b_{10}	$\frac{175}{3}$	$-\frac{25}{2}$	0	0	0	0	$-\frac{25}{2}$	-25	-25	$\frac{175}{2}$	-100	$\frac{75}{2}$
c_1	$-\frac{125}{6}$	$\frac{125}{2}$	$-\frac{125}{2}$	$\frac{125}{6}$	$\frac{125}{6}$	0	0	0	0	0	0	$-\frac{125}{6}$
c_2	$-\frac{125}{2}$	125	$-\frac{125}{2}$	0	0	$\frac{125}{2}$	0	0	0	0	$\frac{125}{2}$	$-\frac{125}{2}$
c_3	$-\frac{125}{2}$	$\frac{125}{2}$	0	0	0	0	$\frac{125}{2}$	0	0	$-\frac{125}{2}$	125	$-\frac{125}{2}$
c_4	$-\frac{125}{6}$	0	0	0	0	0	0	$\frac{125}{6}$	$\frac{125}{6}$	$-\frac{125}{2}$	$\frac{125}{2}$	$-\frac{125}{6}$

Table 20: Alternative set of coefficients for the construction of RT_3, outer functions.

	$\hat{v}_3^{13}$	$\hat{v}_3^{14}$	$\hat{v}_3^{15}$	$\hat{v}_3^{16}$	$\hat{v}_3^{17}$	$\hat{v}_3^{18}$
a_1	0	0	0	0	0	0
a_2	$\frac{1000}{3}$	$\frac{250}{3}$	$\frac{500}{9}$	$\frac{125}{3}$	$\frac{250}{3}$	$\frac{125}{3}$
a_3	0	0	0	0	0	0
a_4	$-\frac{11750}{9}$	$-\frac{5875}{18}$	$-\frac{4250}{9}$	$-\frac{2125}{6}$	$-\frac{250}{3}$	$-\frac{125}{3}$
a_5	$-\frac{9500}{9}$	$-\frac{10375}{18}$	$-\frac{125}{3}$	$-\frac{250}{3}$	$-\frac{2000}{3}$	$-\frac{6625}{18}$
a_6	0	0	0	0	0	0
a_7	$\frac{5000}{3}$	$\frac{1250}{3}$	$\frac{10000}{9}$	$\frac{2500}{3}$	0	0
a_8	$\frac{15625}{6}$	$\frac{3125}{2}$	$\frac{625}{2}$	625	625	$\frac{625}{2}$
a_9	$\frac{1875}{2}$	$\frac{6875}{6}$	0	0	$\frac{8125}{6}$	$\frac{1875}{2}$
a_{10}	0	0	0	0	0	0
b_1	0	0	0	0	0	0
b_2	0	0	0	0	0	0
b_3	$\frac{250}{3}$	$\frac{1000}{3}$	$\frac{125}{3}$	$\frac{250}{3}$	$\frac{125}{3}$	$\frac{500}{9}$
b_4	0	0	0	0	0	0
b_5	$-\frac{10375}{18}$	$-\frac{9500}{9}$	$-\frac{6625}{18}$	$-\frac{2000}{3}$	$-\frac{250}{3}$	$-\frac{125}{3}$
b_6	$-\frac{5875}{18}$	$-\frac{11750}{9}$	$-\frac{125}{3}$	$-\frac{250}{3}$	$-\frac{2125}{6}$	$-\frac{4250}{9}$
b_7	0	0	0	0	0	0
b_8	$\frac{6875}{6}$	$\frac{1875}{2}$	$\frac{1875}{2}$	$\frac{8125}{6}$	0	0
b_9	$\frac{3125}{2}$	$\frac{15625}{6}$	$\frac{625}{2}$	625	625	$\frac{625}{2}$
b_{10}	$\frac{1250}{3}$	$\frac{5000}{3}$	0	0	$\frac{2500}{3}$	$\frac{10000}{9}$
c_1	$-\frac{6250}{9}$	$-\frac{3125}{18}$	$-\frac{6250}{9}$	$-\frac{3125}{6}$	0	0
c_2	$-\frac{3125}{2}$	$-\frac{3125}{3}$	$-\frac{3125}{6}$	$-\frac{3125}{3}$	0	0
c_3	$-\frac{3125}{3}$	$-\frac{3125}{2}$	0	0	$-\frac{3125}{3}$	$-\frac{3125}{6}$
c_4	$-\frac{3125}{18}$	$-\frac{6250}{9}$	0	0	$-\frac{3125}{6}$	$-\frac{6250}{9}$

Table 21: Alternative set of coefficients for the construction of RT_3, inner functions, $\hat{v}_3^{13}$ up to $\hat{v}_3^{18}$.

	$\hat{v}_3^{19}$	$\hat{v}_3^{20}$	$\hat{v}_3^{21}$	$\hat{v}_3^{22}$	$\hat{v}_3^{23}$	$\hat{v}_3^{24}$
a_1	0	0	0	0	0	0
a_2	$-\frac{125}{4}$	$-\frac{125}{8}$	$\frac{375}{32}$	$\frac{125}{16}$	$-\frac{375}{8}$	$-\frac{125}{8}$
a_3	0	0	0	0	0	0
a_4	$\frac{3625}{16}$	$\frac{3625}{32}$	$-\frac{1125}{16}$	$-\frac{375}{8}$	$\frac{3375}{32}$	$\frac{1125}{32}$
a_5	$\frac{875}{16}$	$\frac{2125}{32}$	$-\frac{2125}{32}$	$-\frac{1625}{32}$	$\frac{9875}{32}$	$\frac{4125}{32}$
a_6	0	0	0	0	0	0
a_7	$-\frac{3125}{8}$	$-\frac{3125}{16}$	$\frac{1875}{32}$	$\frac{625}{16}$	$-\frac{1875}{32}$	$-\frac{625}{32}$
a_8	$-\frac{10625}{32}$	$-\frac{13125}{32}$	$\frac{3125}{8}$	$\frac{9375}{32}$	$-\frac{19375}{32}$	$-\frac{1875}{8}$
a_9	$-\frac{625}{32}$	$-\frac{1875}{32}$	$\frac{625}{16}$	$\frac{1875}{32}$	$-\frac{3125}{8}$	$-\frac{9375}{32}$
a_{10}	0	0	0	0	0	0
b_1	0	0	0	0	0	0
b_2	0	0	0	0	0	0
b_3	$-\frac{125}{8}$	$-\frac{375}{8}$	$\frac{125}{16}$	$\frac{375}{32}$	$-\frac{125}{8}$	$-\frac{125}{4}$
b_4	0	0	0	0	0	0
b_5	$\frac{4125}{32}$	$\frac{9875}{32}$	$-\frac{1625}{32}$	$-\frac{2125}{32}$	$\frac{2125}{32}$	$\frac{875}{16}$
b_6	$\frac{1125}{32}$	$\frac{3375}{32}$	$-\frac{375}{8}$	$-\frac{1125}{16}$	$\frac{3625}{32}$	$\frac{3625}{16}$
b_7	0	0	0	0	0	0
b_8	$-\frac{9375}{32}$	$-\frac{3125}{8}$	$\frac{1875}{32}$	$\frac{625}{16}$	$-\frac{1875}{32}$	$-\frac{625}{32}$
b_9	$-\frac{1875}{8}$	$-\frac{19375}{32}$	$\frac{9375}{32}$	$\frac{3125}{8}$	$-\frac{13125}{32}$	$-\frac{10625}{32}$
b_{10}	$-\frac{625}{32}$	$-\frac{1875}{32}$	$\frac{625}{16}$	$\frac{1875}{32}$	$-\frac{3125}{16}$	$-\frac{3125}{8}$
c_1	$\frac{3125}{16}$	$\frac{3125}{32}$	0	0	0	0
c_2	$\frac{9375}{32}$	$\frac{3125}{8}$	$-\frac{9375}{32}$	$-\frac{3125}{16}$	$\frac{9375}{32}$	$\frac{3125}{32}$
c_3	$\frac{3125}{32}$	$\frac{9375}{32}$	$-\frac{3125}{16}$	$-\frac{9375}{32}$	$\frac{3125}{8}$	$\frac{9375}{32}$
c_4	0	0	0	0	$\frac{3125}{32}$	$\frac{3125}{16}$

Table 22: Alternative set of coefficients for the construction of RT_3, inner functions, $\hat{v}_3^{19}$ up to $\hat{v}_3^{24}$.

A.6 Further courses of the reaction forces for the Cook's Membrane example

In the following further results of Chapter 5.3 are shown. In Figure the course of the reaction forces at the left boundary of the Cook's Membrane problem for P_1P_2 and RT_1P_2 are depicted for two additional meshes under consideration of different weights ω_i. For the standard and the mixed Galerkin element the additional computations are shown in Figure 71. Finally, in Figure 72 the evaluation of the reaction forces for higher order least-squares elements are depicted under consideration of the weightings $\omega_1 = 1, \omega_2 = \omega_3 = 1/\mu$.

A.7 Shear stress distribution for the example of the quartered plate.

Figure 73 show the distribution of the shear stresses σ_{12} and σ_{21} over the domain of the quartered plate for two different fine meshes.

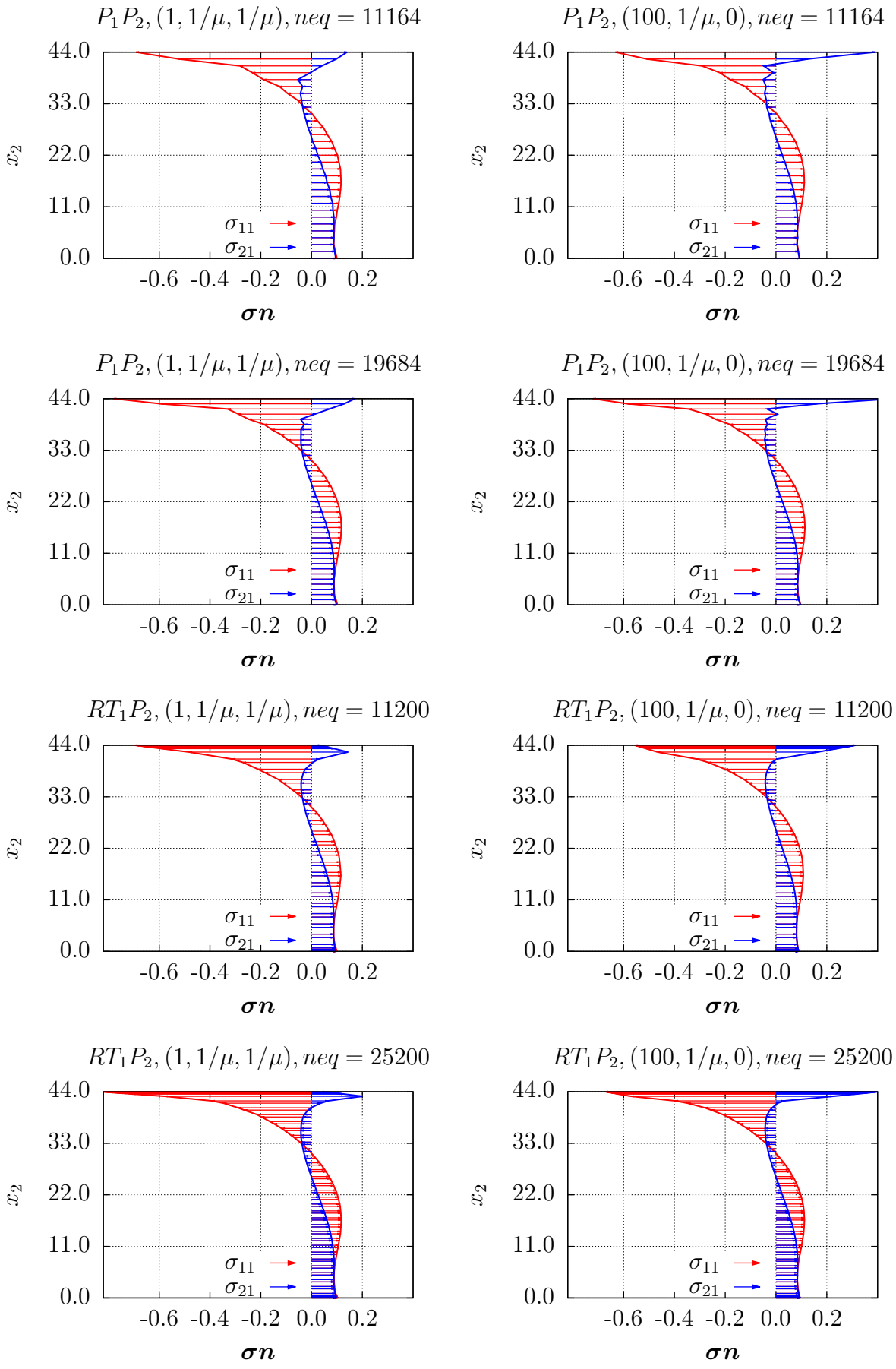

Figure 70: Course of the support reactions for P_1P_2 and RT_1P_2 under consideration of different system sizes neq and different weights ω_i .

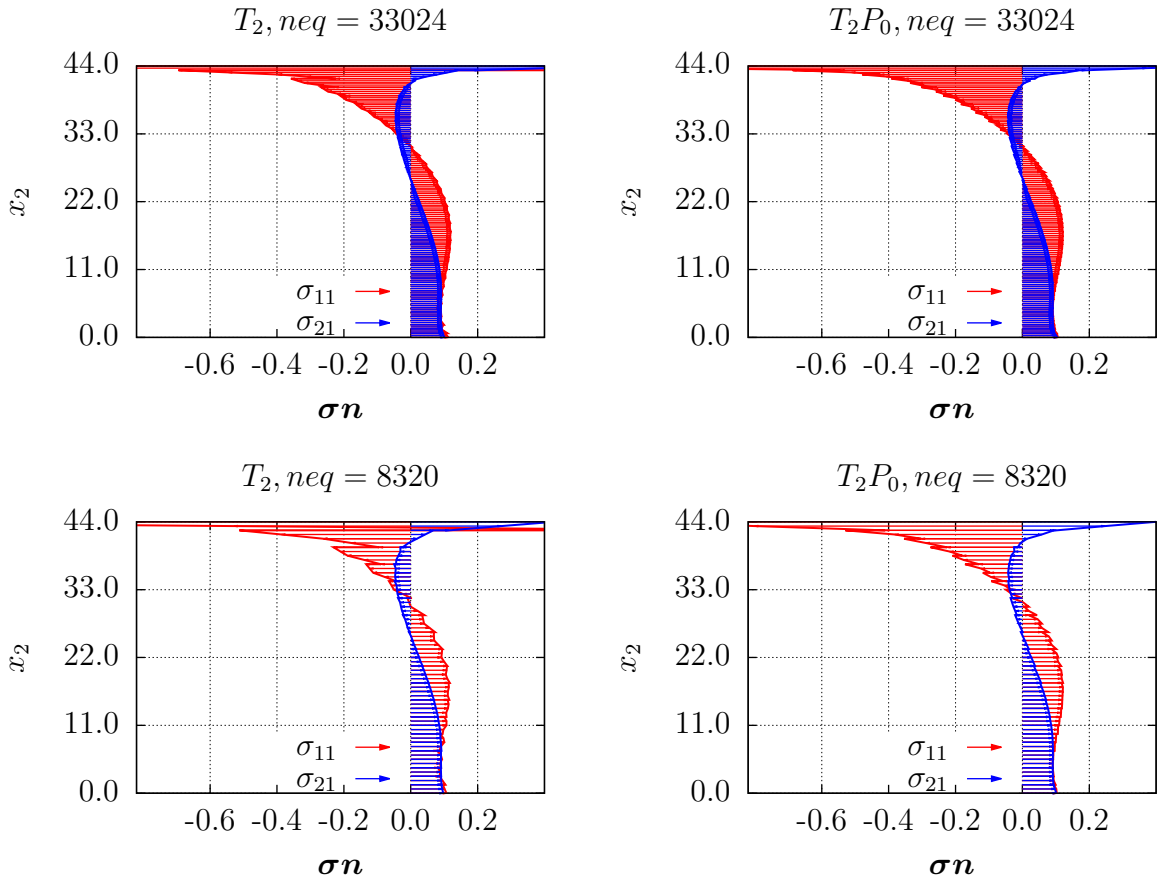

Figure 71: Course of the support reactions for T_2 and T_2P_0 under consideration of different system sizes neq .

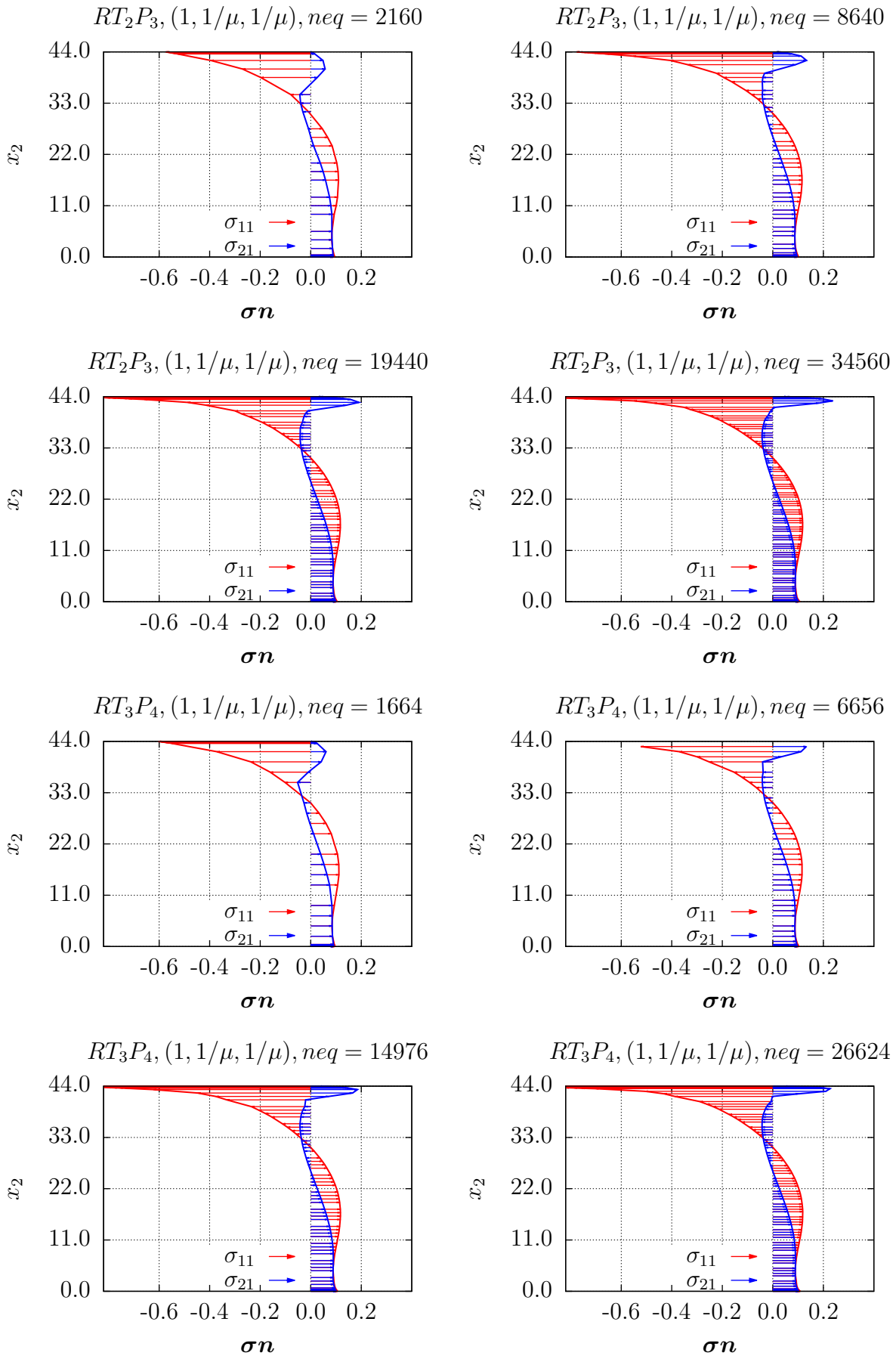

Figure 72: Course of the support reactions for RT_2P_3 and RT_3P_4 under consideration of different system sizes neq .

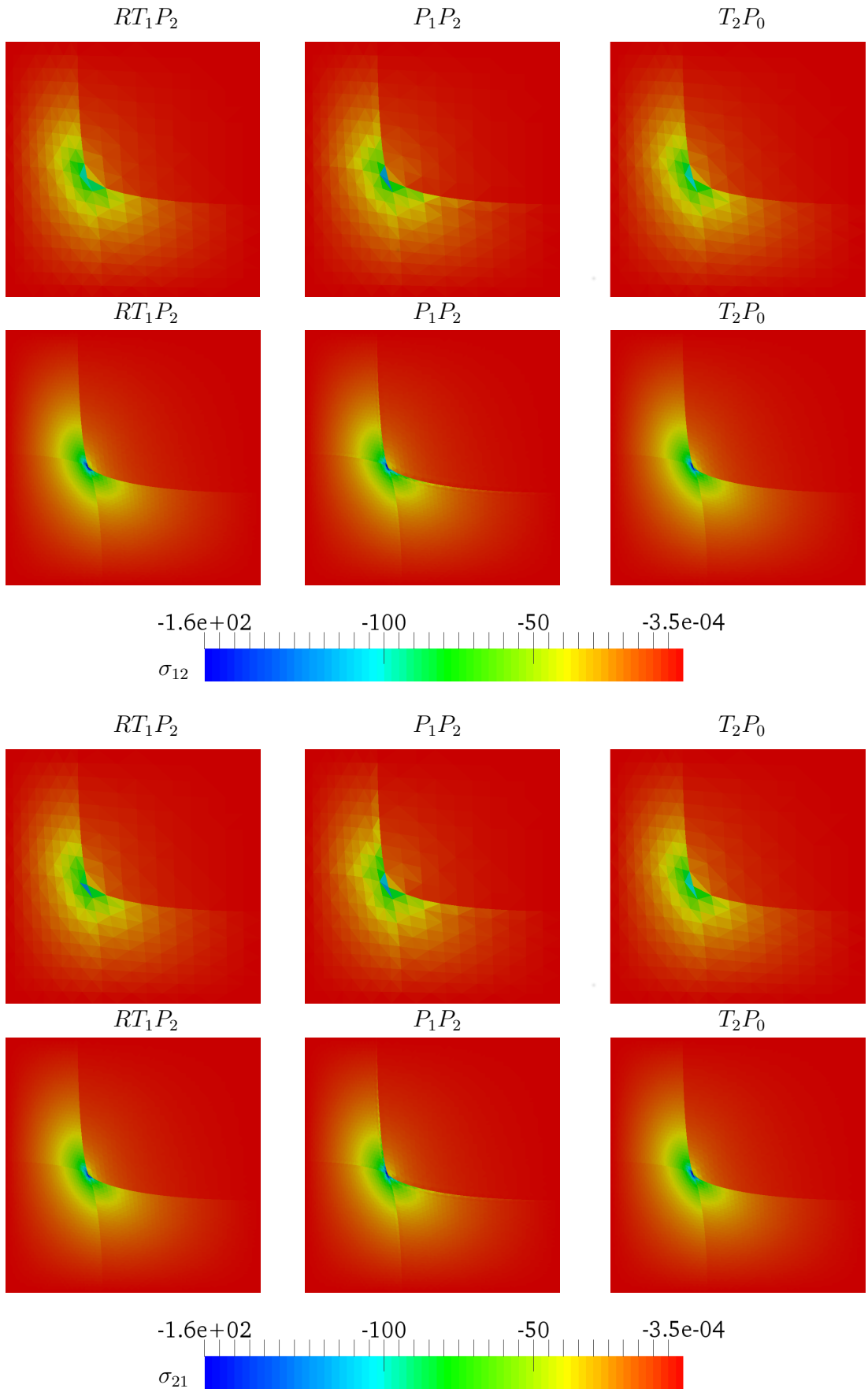

Figure 73: Distribution of the σ_{12} stresses (upper six plots) and σ_{21} stresses (lower six plots) for the quartered plate meshed with 20x20 elements (above) and 80x80 elements (below).

List of Figures

List of Tables

References

AceDoc. https://wiki.uni-due.de/acedoc/. Internal wiki, Institute of Mechanics, Department of Civil Engineering, 2016.

J. Ahrens, B. Geveci, and C. Law. *ParaView: An End-User Tool for Large Data Visualization, Visualization Handbook*. Elsevier, version 10.1 edition, 2005. Champaign, Illinois.

J.H. Argyris. Energy theorems and structural analysis: Part ii. *Aircraft Engineering and Aerospace Technology*, 27(2):42–58, 1955.

J.H. Argyris and D.E.S. Kelsey. Energy theorems and structural analysis: Part i. *Aircraft Engineering and Aerospace Technology*, 26:410–422, 1954.

F. Auricchio, L. Beirão da Veiga, C. Lovadina, and A. Reali. A stability study of some mixed finite elements for large deformation elasticity problems. *Computer Methods in Applied Mechanics and Engineering*, 194:1075–1092, 2005.

F. Auricchio, L. Beirão da Veiga, C. Lovadina, and A. Reali. The importance of the exact satisfaction of the incompressibility constraint in nonlinear elasticity: Mixed FEMs versus NURBS-based approximations. *Computer Methods in Applied Mechanics and Engineering*, 199:314–323, 2010.

F. Auricchio, L. Beirão da Veiga, C. Lovadina, A. Reali, R.L. Taylor, and P. Wrigger. Approximation of incompressible large deformation elastic problems: some unresolved issues. *Computational Mechanics*, 52:1153–1167, 2013.

A.K. Aziz, R.B. Kellogg, and A.B. Stephens. Least squares methods for elliptic systems. *Mathematics of computation*, 44(169):53–70, 1985.

I. Babuška. The finite element method with lagrangian multipliers. *Numerische Mathematik*, 20(3):179–192, 1973.

I. Babuška and W.C. Rheinboldt. A unified least-squares formulation for fluid-structure interaction problems. *SIAM Journal on Mathematical Analysis*, 15(4):736–754, 1978.

I. Babuška and M. Suri. Locking effects in the finite element approximation of elasticity problems. *Numerische Mathematik*, 62(1):439–463, 1992.

D. Balzani. *Polyconvex anisotropic energies and modeling of damage applied to arterial walls*. PhD thesis, University Duisburg-Essen, Verlag Glückauf Essen, 2006.

D. Balzani, P. Neff, J. Schröder, and G.A. Holzapfel. A polyconvex framework for soft biological tissues. adjustment to experimental data. *International Journal for Numerical Methods in Engineering*, 43(20):6052–6070, 2006.

K.-J. Bathe. *Finite Element Procedures*. Prentice Hall, 1995.

K.-J. Bathe. The inf–sup condition and its evaluation for mixed finite element methods. *Computers and Structures*, 79(2):243–252, 2001.

B.C. Bell and K.S. Surana. A space-time coupled p-version least-squares finite element formulation for unsteady fluid dynamics problems. *International Journal for Numerical Methods in Engineering*, 37:3545–3569, 1994.

T. Belytschko, W.K. Liu, and B. Moran. *Nonlinear Finite Elements for Continua and Structures*. John Wiley and Sons, Chichester, 2000.

M. Berndt, T.A. Manteuffel, and S.F. McCormick. Local error estimates and adaptive refinement for first-order system least squares. *Electronic Transactions on Numerical Analysis*, 6:35–43, 1997.

F. Bertrand, S. Münzenmaier, and G. Starke. First-order system least squares on curved boundaries. *SIAM Journal on Scientific Computing*, 52:880–894, 2014.

M. Bischoff, W.A. Wall, and E. Ramm. Stabilized enhanced assumed strain elements for large strain analysis without artificial kinematic modes. *Proc. European Conference on Computational Mechanics*, 1999.

P.B. Bochev. *Least-Squares Finite Element Methods for the Stokes and Navier-Stokes equations*. Phd thesis, Virginia Polytechnic Institute and State University, Blacksburg, Virginia, 1994.

P.B. Bochev. Negative norm least-squares methods for the velocity-vorticity-pressure Navier-Stokes equations. *Numerical Methods for Partial Differential Equations*, 15: 237–256, 1999.

P.B. Bochev and M.D. Gunzburger. Analysis of least squares finite element methods for the Stokes equations. *Mathematics of Computation*, 63:479–506, 1994.

P.B. Bochev and M.D. Gunzburger. Least-squares methods for the velocity-pressure-stress formulation of the Stokes equations. *Computer Methods in Applied Mechanics and Engineering*, 126:267–287, 1995.

P.B. Bochev and M.D. Gunzburger. *Least-Squares Finite Element Methods*. Springer-Verlag, New York, 1st edition, 2009.

P.B. Bochev, Z. Cai, T.A. Manteuffel, and S.F. McCormick. Analysis of velocity-flux least-squares methods for the Navier-Stokes equations, part I. *SIAM Journal on Numerical Analysis*, 35:990–1009, 1998.

P.B. Bochev, T. Manteuffel, and S. McCormick. Analysis of velocity-flux least squares methods for the Navier-Stokes equations, part II. *SIAM Journal on Numerical Analysis*, 36:1125–1144, 1999.

D. Boffi, F. Brezzi, and M. Fortin. *Mixed Finite Element Methods and Applications*. Springer, Heidelberg, 2013.

D. Braess. *Finite Elemente*. Springer-Verlag, Berlin, 2nd edition, 1997.

F. Brezzi. On the existence, uniqueness and approximation of saddle-point problems arising from lagrangian multipliers. *Revue française d'automatique, informatique, recherche opérationnelle. Analyse numérique*, 8(2):129–151, 1974.

F. Brezzi, J. Douglas, and L.D. Martini. Two families of mixed finite elements for second order elliptic problems. *Numerische Mathematik*, 47:217–325, 1985.

Z. Cai and G. Starke. First-order system least squares for the stress-displacement formulation: Linear elasticity. *SIAM Journal on Numerical Analysis*, 41:715–730, 2003.

Z. Cai and G. Starke. Least-squares methods for linear elasticity. *SIAM Journal on Numerical Analysis*, 42:826–842, 2004.

Z. Cai, R. Lazarov, T.A. Manteuffel, and S.F. McCormick. First-order system least squares for second-order partial differential equations: Part I. *SIAM Journal on Numerical Analysis*, 31:1785–1799, 1994.

Z. Cai, T.A. Manteuffel, and S.F. McCormick. First-order system least squares for velocity-vorticity-pressure form of the Stokes equations, with application to linear elasticity. *Electronic Transactions on Numerical Analysis*, 3:150–159, 1995.

Z. Cai, T.A. Manteuffel, and S.F. McCormick. First-order system least squares for the Stokes equation, with application to linear elasticity. *SIAM Journal on Numerical Analysis*, 34:1727–1741, 1997.

Z. Cai, T.A. Manteuffel, S.F. McCormick, and S.V. Parter. First-order system least squares (FOSLS) for planar linear elasticity: Pure traction problem. *SIAM Journal on Numerical Analysis*, 35:320–335, 1998.

Z. Cai, C.-O. Lee, T.A. Manteuffel, and S.F. McCormick. First-order system least squares for linear elasticity: Numerical results. *SIAM Journal on Scientific Computing*, 21: 1706–1727, 2000a.

Z. Cai, C.-O. Lee, T.A. Manteuffel, and S.F. McCormick. First-order system least squares for the Stokes and linear elasticity equations: Further results. *SIAM Journal on Scientific Computing*, 21:1728–1739, 2000b.

Z. Cai, J. Korsawe, and G. Starke. An adaptive least squares mixed finite element method for the stress-displacement formulation of linear elasticity. *Numerical Methods for Partial Differential Equations*, 21:132–148, 2005.

C. Chang and B.-N. Jiang. An error analysis of least-squares finite element method of velocity-pressure-vorticity formulation for the Stokes problem. *Computer Methods in Applied Mechanics and Engineering*, 84:247–255, 1990.

C. Chang, S.Y Yang, and C.H. Hsu. A least-squares finite element method for incompressible flow in stress-velocity-pressure version. *Computer Methods in Applied Mechanics and Engineering*, 128:1–9, 1995.

P.G. Ciarlet. *Handbook of Numerical Analysis, vol II: Finite Element Methods, Part 1.* Elsevier Science Ltd, 1991.

P.G. Ciarlet and G. Geymonat. Sur les lois de comportement en élasticité non-linéaire compressible. *CR Acad. Sci. Paris Sér. II*, 295:423–426, 1982.

R.W. Clough. The finite element method in plane stress analysis. 1960.

E.A. de Souza Neto, F.M. Andrade Pires, and D.R.J. Owen. Design of simple low order finite elements for large strain analysis of nearly incompressible solids. *International Journal of Solids and Structures*, 33:3277–3296, 1996.

E.A. de Souza Neto, F.M. Andrade Pires, and D.R.J. Owen. F-bar based linear triangles and tetrahedra for finite strain analysis of nearly incompressible solids. Part I: formulation and benchmarking. *International Journal of Solids and Structures*, 62:353–383, 2005.

B. Delaunay. Sur la sphere vide. *Izv. Akad. Nauk SSSR, Otdelenie Matematicheskii i Estestvennyka Nauk*, 7(793-800):1–2, 1934.

X. Ding and T.T.H. Tsang. Large eddy simulation of turbulent flows by a least-squares finite element method. *International Journal for Numerical Methods in Fluids*, 37: 297–319, 2001.

X. Ding and T.T.H. Tsang. On first-order formulations of the least-squares finite element method for incompressible flows. *International Journal of Computational Fluid Dynamics*, 17:183–197, 2003.

W.P. Doherty, E.L. Wilson, and R.L. Taylor. Stress analysis of axisymmetric solids utilizing higher order quadrilateral finite elements, sesm report 69-3, department of civil engineering. *University of California, Berkeley*, 1969.

C.R. Dohrmann, M. W. Heinstein, J. Jung, S. W. Key, and W. R. Witkowski. Node-based uniform strain elements for three-node triangular and four-node tetrahedral meshes. *International Journal for Numerical Methods in Engineering*, 47:1549–1568, 2000.

W. Dörfler. A convergent adaptive algorithm for poisson's equation. *SIAM Journal on Numerical Analysis*, 33(3):1106–1124, 1996.

A. Düster, S. Hartmann, and E. Rank. p-fem applied to finite isotropic hyperelastic bodies. *Computer Methods in Applied Mechanics and Engineering*, 192(47):5147–5166, 2003.

E.D. Eason. A review of least-squares methods for solving partial differential equations. *International Journal for Numerical Methods in Engineering*, 10:1021–1046, 1976.

V. Ebbing. *Design of Polyconvex Energy Functions for All Anisotropy Classes.* PhD thesis, Institut für Mechanik, Abteilung Bauwissenschaften, Fakultät für Ingenieurwissenschaften, Universität Duisburg-Essen, 2010.

A.C. Eringen. *Mechanics of continua.* John Wiley & Sons, 1967.

A. Ern and J.-L. Guermond. *Theory and practice of finite elements*, volume 159. Springer Science & Business Media, 2013.

V.J. Ervin. Computational bases for RT_k and BDM_k on triangles. *Computers and Mathematics with Applications*, 64(8):2765–2774, 2012.

L. Euler. *Methodus inveniendi lineas curvas maximi minimive proprietate gaudentes sive solutio problematis isoperimetrici latissimo sensu accepti. Additamentum I : De curvis elasticis.* Lausannae & Genevae, 1744.

G.J. Fix, M.D. Gunzburger, and R.A. Nicolaides. On finite element methods of the least squares type. *Computers and Mathematics with Applications*, 5:87–98, 1979.

C. Freischläger and K. Schweizerhof. On a systematic development of trilinear three-dimensional solid elements based on Simo's enhanced strain approach. *International Journal of Solids and Structures*, 33,No.20-22:2993–3017, 1996.

B.G. Galerkin. Series solution of some problems of elastic equilibrium of rods and plates. *Vestn. Inzh. Tekh*, 19:897–908, 1915.

M.W. Gee, C.R. Dohrmann, S.W. Key, and W.A. Wall. A uniform nodal strain tetrahedron with isochoric stabilization. *International Journal for Numerical Methods in Engineering*, 78:429–443, 2009.

U. Heisserer, S. Hartmann, A. Düster, and Z. Yosibash. On volumetric locking-free behaviour of p-version finite elements under finite deformations. *Communications in numerical methods in engineering*, 24(11):1019–1032, 2008.

G.A. Holzapfel. *Nonlinear Solid Mechanics - A Continuum Approach for Engineering*. John Wiley and Sons, 2000.

H. Jarausch. On an adaptive grid refining technique for finite element approximations. *SIAM journal on scientific and statistical computing*, 7(4):1105–1120, 1986.

D. Jespersen. A least-squares decomposition method for solving elliptic equations. *Mathematics of Computation*, 31:873–880, 1977.

B.-N. Jiang. A least-squares finite element method for incompressible Navier-Stokes problems. *International Journal for Numerical Methods in Fluids*, 14:843–859, 1992.

B.-N. Jiang. *The Least-Squares Finite Element Method*. Springer-Verlag, Berlin, 1998.

B.-N. Jiang. The least-squares finite element method in elasticity. Part ii: Bending of thin plates. *International Journal for Numerical Methods in Engineering*, 54(10):1459–1475, 2002.

B.-N. Jiang and C.L. Chang. Least-squares finite elements for the Stokes problem. *Computer Methods in Applied Mechanics and Engineering*, 78:297–311, 1990.

B.-N. Jiang and J. Wu. The least-squares finite element method in elasticity. Part I: Plane stress or strain with drilling degrees of freedom. *International Journal for Numerical Methods in Engineering*, 53:621–636, 2002.

C. Johnson. Adaptive finite element methods for diffusion and convection problems. *Computer Methods in Applied Mechanics and Engineering*, 82(1-3):301–322, 1990.

C. Kadapa, W.G. Dettmer, and D. Perić. Nurbs based least-squares finite element methods for fluid and solid mechanics. *International Journal for Numerical Methods in Engineering*, 101(7):521–539, 2015.

O. Kayser-Herold and H.G. Matthies. Space-time adaptive solution of fluid-structure interaction problems. *In 2nd MIT Conference on Computational Fluid and Solid Mechanics, Amsterdam*, pages 1000–1004, 2003.

O. Kayser-Herold and H.G. Matthies. Least-squares FEM, literature review. *Informatik-Bericht 2005-05, TU Braunschweig, Institut für Wissenschaftliches Rechnen*, 2005.

O. Kayser-Herold and H.G. Matthies. A unified least-squares formulation for fluid-structure interaction problems. *Computers and Structures*, 85:998–1011, 2007.

S.D. Kim, T.A. Manteuffel, and S.F. McCormick. First-order system least squares (FOSLS) for spatial linear elasticity: Pure traction. *SIAM Journal on Numerical Analysis*, 38:1454–1482, 2000.

O. Klaas, J. Schröder, E. Stein, and C. Miehe. A regularized dual mixed element for plane elasticity implementation and performance of the BDM element. *Computer Methods in Applied Mechanics and Engineering*, 121:201–209, 1995.

J. Korelc. Automatic generation of finite-element code by simultaneous optimization of expressions. *Theoretical Computer Science*, 187:231–248, 1997.

J. Korelc. Multi-language and multi-environment generation of nonlinear finite element codes. *Engineering with Computers*, 18:312–327, 2002.

J. Korelc and P. Wriggers. *Automation of finite element methods*. Springer, 2016.

F. Koschnick. *Geometrische Lockingeffekte bei finiten Elementen und ein allgemeines Konzept zu ihrer Vermeidung*. PhD thesis, Technische Universität München, 2004.

K.C. Kwon, S.H. Park, and S.K. Youn. The least-squares meshfree method for elastoplasticity and its application to metal forming analysis. *International Journal for Numerical Methods in Engineering*, 64:751–788, 2005.

O.A. Ladyzhenskaya. *The mathematical theory of viscous incompressible flow*, volume 76. Gordon and Breach New York, 1969.

G.R. Liu and T. Nguyen-Thoi. *Smoothed finite element methods*. CRC Press, Taylor and Francis Group, 2010.

P.P. Lynn and S.K. Arya. Use of the least squares criterion in the finite element formulation. *International Journal for Numerical Methods in Engineering*, 6:75–88, 1973.

P.P. Lynn and S.K. Arya. Finite elements formulated by the weighted discrete least squares method. *International Journal for Numerical Methods in Engineering*, 8:71–90, 1974.

T.A. Manteuffel, S.F. McCormick, J.G. Schmidt, and C.R. Westphal. First-order system least squares (FOSLS) for geometrically nonlinear elasticity. *SIAM Journal on Numerical Analysis*, 44:2057–2081, 2006.

J.E. Marsden and T.J.R. Hughes. *Mathematical foundations of elasticity*. Dover Publications, Inc., 1994.

W.F. Mitchell. A comparison of adaptive refinement techniques for elliptic problems. *ACM Transactions on Mathematical Software (TOMS)*, 15(4):326–347, 1989.

G.E. Moore. Cramming more components onto integrated circuits. *Electronics*, 38(20): 114–117, 1965.

B. Müller. *Mixed least squares finite element methods based on inverse stress-strain relations in hyperelasticity*. PhD thesis, Duisburg, Essen, 2015. Duisburg, Essen, Univ., Diss., 2015.

B. Müller and G. Starke. Stress-based finite element methods in linear and nonlinear solid mechanics. In J. Schröder and P. Wriggers, editors, *Advanced Finite Element Technologies*, CISM Courses and Lectures. Springer, 2016.

B. Müller, G. Starke, A. Schwarz, and J Schröder. A first-order system least squares method for hyperelasticity. *SIAM Journal on Scientific Computing*, 36:795–816, 2014.

J.C. Nash. *Compact numerical methods for computers: linear algebra and function minimisation*. CRC Press, 1990.

T. Netz, A. Düster, and S. Hartmann. High-order finite elements compared to low-order mixed element formulations. *Journal of Applied Mathematics and Mechanics*, 93(2-3): 163–176, 2013.

A.K. Noor. Bibliography of books and monographs on finite element technology. *Applied Mechanics Reviews*, 44(6):307–317, 1991.

R.W. Ogden. *Non-linear elastic deformations*. Dover Publications, 1984.

H. Parisch. *Festkörper-Kontinuumsmechanik: von den Grundgleichungen zur Lösung mit finiten Elementen*. Springer-Verlag, 2013.

A. Pflüger. *Stabilitätsprobleme der Elastostatik*. Springer-Verlag, 1975.

T.H.H. Pian. Derivation of element stiffness matrices by assumed stress distribution. *AIAA Journal*, 20:1333–1336, 1964.

T.H.H. Pian and K. Sumihara. A rational approach for assumed stress finite elements. *International Journal for Numerical Methods in Engineering*, 20:1685–1695, 1984.

J.P. Pontaza. *Least-squares variational principles and the finite element method: theory, form, and model for solid and fluid mechanics*. PhD thesis, Texas A&M University, 2003.

J.P. Pontaza and J.N. Reddy. Spectral/hp least-squares finite element formulation for the Navier-Stokes equations. *Journal of Computational and Applied Mathematics*, 190: 523–549, 2003.

P.A. Raviart and J.M. Thomas. A mixed finite element method for 2-nd order elliptic problems. Mathematical aspects of finite element methods. *Lecture Notes in Mathematics, Springer-Verlag New York*, pages 292–315, 1977.

B.D. Reddy and J.C. Simo. Stability and convergence of a class of enhanced strain methods. *SIAM Journal on Numerical Analysis*, 32)(6):1705–1728, 1995.

S. Reese and P. Wriggers. A stabilization technique to avoid hourglassing in finite elasticity. *International Journal for Numerical Methods in Engineering*, 48:79–109, 2000.

S. Reese, M. Küssner, and B.D. Reddy. A new stabilization technique for finite elements in non-linear elasticity. *International Journal for Numerical Methods in Engineering*, 44:1617–1652, 1999.

J. Schröder. Anisotropic polyconvex energies. In J. Schröder and P. Neff, editors, *Poly-, quasi- and rank-one convexity in applied mechanics*, volume 516 of *CISM Courses and Lectures*, pages 53–106. Springer, 2010.

J. Schröder and P. Neff. On the construction of polyconvex anisotropic free energy functions. In C. Miehe, editor, *Proceedings of the IUTAM Symposium on Computational Mechanics of Solid Materials at Large Strains*, pages 171–180. Kluwer Academic Publishers, 2001.

J. Schröder and P. Neff. Invariant formulation of hyperelastic transverse isotropy based on polyconvex free energy functions. *International Journal of Solids and Structures*, 40:401–445, 2003.

J. Schröder, O. Klaas, E. Stein, and C. Miehe. A physically nonlinear dual mixed finite element formulation. *Computer Methods in Applied Mechanics and Engineering*, 144: 72–92, 1997.

J. Schröder, P. Neff, and V. Ebbing. Anisotropic polyconvex energies on the basis of crystallographic motivated structural tensors. *Journal of the Mechanics and Physics of Solids*, 56(12):3486–3506, 2008.

J. Schröder, R. de Boer, and J. Bluhm. *Tensor Calculus for Engineers with Applications to Continuum and Computational Mechanics*. Springer-Verlag, Berlin, 2016. to appear.

J. Schröder, A. Schwarz, and K. Steeger. Least-squares finite element formulations for isotropic and anisotropic elasticity at small and large strains. In J. Schröder and P. Wriggers, editors, *Advanced Finite Element Technologies*, CISM Courses and Lectures. Springer, 2016.

A. Schwarz. *Least-Squares Mixed Finite Elements for Solid Mechanics*. PhD thesis, University Duisburg-Essen, 2009.

A. Schwarz and J. Schröder. Least-squares mixed finite elements with applications to anisotropic elasticity and viscoplasticity. *Proceedings in Applied Mathematics and Mechanics*, 7:4040043–4040044, 2007.

A. Schwarz, J. Schröder, and G. Starke. Least-squares mixed finite elements for small strain elasto-viscoplasticity. *International Journal for Numerical Methods in Engineering*, 77:1351–1370, 2009a.

A. Schwarz, J. Schröder, and K. Steeger. A modified least-squares finite element formulation for small strain plasticity. *Proceedings of ICCSM 2009*, 2009b.

A. Schwarz, J. Schröder, and G. Starke. A modified least-squares mixed finite element with improved momentum balance. *International Journal for Numerical Methods in Engineering*, 81:286–306, 2010.

A. Schwarz, J. Schröder, G. Starke, and K. Steeger. Least-squares mixed finite elements for hyperelastic material models. In *Report of the Workshop 1207 at the "Mathematisches Forschungsinstitut Oberwolfach" entitled "Advanced Computational Engineering", organized by O. Allix, C. Carstensen, J. Schröder, P. Wriggers*, pages 470–472, 2012.

A. Schwarz, K. Steeger, and J. Schröder. Weighted overconstrained least-squares mixed finite elements for static and dynamic problems in quasi-incompressible elasticity. *Computational Mechanics*, 54(1):603–612, 2014.

J.C. Simo and F. Armero. Geometrically Non-Linear Enhanced Strain Mixed Methods and the Method of Incompatible Modes. *International Journal for Numerical Methods in Engineering*, 33:1413–1449, 1992.

J.C. Simo and M.S. Rifai. A class of assumed strain methods and the method of incompatible modes. *International Journal for Numerical Methods in Engineering*, 29: 1595–1638, 1990.

J..C. Simo, R.L. Taylor, and K.S. Pister. Variational and projection methods for the volume constraint in finite deformation elasto-plasticity. *Computer Methods in Applied Mechanics and Engineering*, 51:177–208, 1984.

J.C. Simo, F. Armero, and R.L. Taylor. Assumed enhanced strain tri-linear elements for 3D finite deformation problems. *Computer Methods in Applied Mechanics and Engineering*, 110:359–386, 1993.

G. Starke. An adaptive least-squares mixed finite element method for elasto-plasticity. *SIAM Journal on Numerical Analysis*, 45:371–388, 2007.

G. Starke. Adaptive least squares finite element methods in elasto-plasticity. *Proccedings 7th International Conference on Large Scale Scientific Computations*, pages 676–682, 2009.

G. Starke, B. Müller, A. Schwarz, and J. Schröder. Stress-displacement least squares mixed finite element approximation for hyperelastic materials. In *Report of the Workshop 1207 at the "Mathematisches Forschungsinstitut Oberwolfach" entitled "Advanced Computational Engineering", organized by O. Allix, C. Carstensen, J. Schröder, P. Wriggers*, pages 467–469, 2012.

K. Steeger, J. Schröder, and A. Schwarz. Comparison of a mixed least-squares formulation using different approximation spaces. *Proceedings in Applied Mathematics and Mechanics*, 15:233–234, 2015.

E. Stein. Milestones of direct variational calculus and its analysis from the 17th century until today and beyond -Mathematics meets Mechanics- with restriction to linear elasticity. *Computer Assisted Methods in Engineering and Science*, 19:7–91, 2012.

E. Stein and F.-J. Barthold. Elastizitätstheorie. In G. Mehlhorn, editor, *Der Ingenieurbau: Grundwissen*. Ernst and Sohn, 1996.

E. Stein, R. De Borst, and T.J.R. Hughes. *Encyclopedia of computational mechanics - vol. 1 Fundamental, vol. 2 Solids and Structures, vol. 3 Fluids*. John Wiley & Sons, 2004.

L. Tang and T.T.H. Tsang. A least-squares finite element method for time dependent incompressible flows with thermal convection. *International Journal for Numerical Methods in Fluids*, 17:271–289, 1993.

R.L. Taylor, P.J. Beresford, and E.L. Wilson. A non-conforming element for stress analysis. *Computer Methods in Applied Mechanics and Engineering*, 7:1–16, 1976.

C. Truesdell and W. Noll. The nonlinear field theories of mechanics. In S. Flügge, editor, *Handbuch der Physik III/3*. Springer, 1965.

C. Truesdell and W. Noll. *The Non-Linear Field Theories of Mechanics*. Springer, third edition, 2004.

C. Truesdell and R. Toupin. The classical field theories. In S. Flügge, editor, *Encyclopedia of Physics*. Springer, 1960.

M.J. Turner, R.W. Clough, H.C. Martin, and L.J. Topp. Stiffness and deflection analysis of complex structures. *Journal of the Aeronautical Sciences*, 23:805–823, 1956.

R. Verfürth. A posteriori error estimation and adaptive mesh-refinement techniques. *Journal of Computational and Applied Mathematics*, 50(1):67–83, 1994.

F.B. De Veubeke. Displacement and equilibrium models in the finite element method. *Stress analysis*, 9:145–197, 1965.

M. Šilhavý. *The mechanics and thermodynamics of continuous media*. Springer, 1997.

C.R. Westphal. *First-order system least squares for geometrically-nonlinear elasticity in nonsmooth domains*. PhD thesis, Citeseer, 2004.

E.L. Wilson, R.L. Taylor, W.P. Doherty, and J. Ghabaussi. Incompatible displacement models. *S.J. Fenves et al., eds., Numerical and Computer Methods in Structural Mechanics (Academic Press, New York)*, pages 43–57, 1973.

Inc. Wolfram Research. *Mathematica*. Wolfram Research, Inc., version 10.1 edition, 2015. Champaign, Illinois.

P. Wriggers. *Nichtlineare Finite-Element-Methoden*. Springer-Verlag, Berlin, 2001.

P. Wriggers and S. Reese. A note on enhanced strain methods for large deformations. *Computer Methods in Applied Mechanics and Engineering*, 135:201–209, 1996.

J.Z. Zhu, R.L. Taylor, and O.C. Zienkiewicz. *The finite element method: its basis and fundamentals*. Butterworth Heinemann, 2005.

O.C. Zienkiewicz and R.L. Taylor. *The Finite Element Method - Volume I: The Basis*. Butterworth Heinemann, 5th edition, 2000.

O.C. Zienkiewicz and J.Z. Zhu. Adaptivity and mesh generation. *International Journal for Numerical Methods in Engineering*, 32(4):783–810, 1991.

O.C. Zienkiewicz, D.R. Owen, and K.N. Lee. Least square-finite element for elasto-static problems. Use of 'reduced' integration. *International Journal for Numerical Methods in Engineering*, 8:341–358, 1974.

Der Lebenslauf ist in der Online-Version aus Gründen des Datenschutzes nicht enthalten.

In dieser Schriftenreihe bisher erschienene Berichte:

Nr. 1 (2004) *Ein Modell zur Beschreibung finiter anisotroper elastoplastischer Deformationen unter Berücksichtigung diskreter Rissausbreitung*, J. Löblein, Dissertation, 2004.

Nr. 2 (2006) *Polyconvex Anisotropic Energies and Modeling of Damage applied to Arterial Walls*, D. Balzani, Dissertation, 2006.

Nr. 3 (2006) *Kontinuumsmechanische Modellierung ferroelektrischer Materialien im Rahmen der Invariatentheorie*, H. Romanowski, Dissertation, 2006.

Nr. 4 (2007) *Mehrskalen-Modellierung polykristalliner Ferroelektrika basierend auf diskreten Orientierungsverteilungsfunktionen*, I. Kurzhöfer, Dissertation, 2007.

Nr. 5 (2007) *Proceedings of the First Seminar on the Mechanics of Multifunctional Materials*, J. Schröder, D.C. Lupascu, D. Balzani (Ed.), Tagungsband, 2007.

Nr. 6 (2008) *Zur Modellierung und Simulation diskreter Rissausbreitungsvorgänge*, O. Hilgert, Dissertation, 2008.

Nr. 7 (2009) *Least-Squares Mixed Finite Elements for Solid Mechanics*, A. Schwarz, Dissertation, 2009.

Nr. 8 (2010) *Design of Polyconvex Energy Functions for All Anisotropy Classes*, V. Ebbing, Dissertation, 2010.

Nr. 9 (2012) *Modeling of Electro-Mechanically Coupled Materials on Multiple Scales*, M.-A. Keip, Dissertation, 2012.

Nr. 10 (2012) *Geometrical Modeling and Numerical Simulation of Heterogeneous Materials*, D. Brands, Dissertation, 2012.

Nr. 11 (2012) *Modeling and simulation of arterial walls with focus on damage and residual stresses*, S. Brinkhues, Dissertation, 2012.

Nr. 12 (2014) *Proceedings of the Second Seminar on the Mechanics of Multifunctional Materials*, J. Schröder, D.C. Lupascu, M.-A. Keip, D. Brands (Ed.), Tagungsband, 2014.

Nr. 13 (2016) *Mixed least squares finite element methods based on inverse stress-strain relations in hyperelasticity*, B. Müller, Dissertation, 2016.

Nr. 14 (2016) *Electromechanical Modeling and Simulation of Thin Cardiac Tissue Constructs* , R. Frotscher, Dissertation, 2016.